Damage Characterization and Modeling of Notched Graphite/Epoxy Sandwich Panels in Compression

by

José María Mirazo Antolín

B. S., Parks College of St. Louis University
(1996)

Submitted to the Department of Aeronautics and Astronautics
in partial fulfillment of the requirements for the degree of

Master of Science in Aeronautics and Astronautics

at the

MASSACHUSETTS INSTITUTE OF TECHNOLOGY

February 1999

Author . . . . . .
Department of Aeronautics and Astronautics
January 28, 1999

Certified by . . . . . .
S. Mark Spearing
Esther and Harold E. Edgerton
Assistant Professor of Aeronautics and Astronautics
Thesis Supervisor

Accepted by . . . . . .
Jaime Peraire, Associate Professor
Chairman, Department Committee on Graduate Students

Damage Characterization and Modeling of Notched Graphite/Epoxy Sandwich Panels in Compression

by

José María Mirazo Antolín

Submitted to the Department of Aeronautics and Astronautics
on January 15, 1999, in partial fulfillment of the
requirements for the degree of
Master of Science in Aeronautics and Astronautics

Abstract

Damage tolerant design, which focuses on a structure's ability to perform in a damaged state, is widely used in the aerospace industry today. Although extensive research has been carried out in this area for notched composite laminates, a relatively small fraction has dealt with compressive loading of composite honeycomb sandwich panels. Furthermore, little emphasis has been placed on identifying and modeling the damage mechanisms that contribute to ultimate failure. In an attempt to better understand the damage propagation and residual properties of notched composite panels subjected to compressive loads, edge-wise uniaxial quasi-static tests were performed in displacement control. Coupons consisted of various sized notched sandwich panels with woven Graphite-reinforced PMC facesheets and Nomex honeycomb cores. Two lay-ups were used in the facesheets: [45/0/0] and [0/0/0/], identified as T45 and T0 respectively for simplicity. Damage propagated in all coupons perpendicular to the load direction from one or more of the four notch tips. All coupons were loaded to final failure. *In-situ* and *post-mortem* damage evaluation techniques such as polishing and microscopy were employed to describe the damage progression. The key microscopic damage mechanisms were identified to be delamination and fiber micro-buckling, which often led to kink-band formation. Two distinct failure types were identified macroscopically: linear damage zones (LDZ's) and delamination/bulge zones (DBZ's), the latter being confined to the T45 series. The LDZ's consisted of out-of-plane kink-bands propagating away from the notch in the 0° plies, and were modeled using a bridged-crack analogy with tensile loading (DZM). The DBZ's were formed by the outer 45° ply, which delaminated from the rest of the coupon and buckled locally into a deformed out-of-plane curved shape. They were described using a novel one-dimensional delamination/buckling propagation model (DBM). Comparison between the two models revealed that smaller panels were more prone to linear damage zone formation, whereas larger panels were more prone to delamination/buckling zone formation. Damage mechanism charts were produced which are capable of predicting the operative damage mechanism as a function of material and geometric parameters.

Thesis Supervisor: S. Mark Spearing
Title: Esther and Harold E. Edgerton Assistant Professor of Aeronautics and Astronautics

Acknowledgements

The completion of this thesis would not have been possible without the trust, guidance, help and friendship of my advisor, Prof. S. M. Spearing. I hereby thank him for giving me the opportunity to pursue this study and entrusting me with such an endeavor. Alongside I would like to thank the other TELAC professors for their ideas and suggestions during the weekly lab meetings and their friendly support in general: Prof. P. A. Lagace, Prof. H. McManus, Prof. C. Cesnik, and especially Prof. J. Dugundji for the enlightenment he provided to the modeling in this research. Not least I would like to thank the people who helped me in the various laboratories I had to spend time in: TELAC technician, John Kane, for his instruction, help and advice down at the lab, and for always having a solution to all my problems however bizarre they were; Don Weiner for allowing use of his shop and sharing much of his own time and expertise; Lenny Rigione for having the patience to coach me in the arts of potting and microscopy; and Pat Kerney for allowing access to his polishing lab. I cannot forget mentioning the administrative side of TELAC: many thanks go to Deb Bowser (the lab would be chaos without her) and Ping Lee (who is the mistress of all monetary issues). I would also like to mention some people in the Aero/Astro Department who have consistently helped me during my stay at MIT: Liz Zotos for welcoming me and showing me around, Kathryn Fischer for being so friendly and helpful, and Hillary De Baun for her co-operation and understanding. Thank you all!

The student body in the lab has also been terribly co-operative during these two years. Special mentions go to fellow TELAC grad student Mike Toribio (big boy!), who started from scratch with me in this project and shared its initial complications and frustrations; and to my UROP, Dylan McConaghy, who helped me with the most time-consuming portion of this work: polishing. And to the rest of the students that I had the privilege to interact with in TELAC, I want to thank you for being there whenever I needed a hand and wish you all the best in life! Outside the lab, I would like to mention Martin Norsell,

who started out being my classmate and ended up being my friend for life (thanks for being so patient with my never-ending MATLAB questions).

The deepest and dearest thanks go, however, to the people who are most directly responsible for me being who I am today: my parents Mari Asun and José María. Without their support, encouragement and love this would have been nothing but a dream. Dedicating this work to them is my modest way of thanking them for the sacrifice and effort they put themselves through to provide me with this opportunity. I hope I didn't disappoint you. I love you with all my heart.

They say that behind every great man there is a great woman. Well, I don't claim to be a great man, but I certainly have an incredible woman by my side in Magdalena. Her motivation, comfort and strength have made the completion of this thesis feasible. Thank you for being there through the good and the bad times. Thank you for being the lighthouse in the storm. Thank you for your friendship and thank you for your love. "PE PIEPO".

Finally, I would like to thank God for His inspiration and guidance throughout my life.

Foreword

This work was performed in the Technology Laboratory for Advanced Composites (TELAC) in the Department of Aeronautics and Astronautics at the Massachusetts Institute of Technology, Cambridge, Massachusetts (US). Sponsorship was provided by the Boeing Commercial Aircraft Group Structural Methods and Allowables group, a division of The Boeing Company, under Boeing Purchase Order Number B-283502; and by NSF Career Award CMS-9702399.

Contents

List of Figures

List of Tables

Nomenclature

a	notch half-width, damage length, delamination half-length
a_c	critical crack length at which steady-state crack growth is reached
b	notch half-width
l	crack length, delamination length (bulge width)
m	crack singularity in Mar-Lin correlation
n	number of segments (in x-direction) into which cohesive zone is divided
s	path length along buckled sub-laminate
t	ply thickness
t_1	top sub-laminate thickness
t_2	bottom sub-laminate thickness
u	applied strain
u_{prop}	applied strain for bulge propagation
u_{cr}	critical applied strain for plate to buckle
u_{cr1}	critical applied strain for top sub-laminate to buckle
u_{cr2}	critical applied strain for bottom sub-laminate to buckle
v	crack opening displacement
v_c	critical crack opening displacement at which bridging traction is zero
v_i^S	crack surface displacement due to remote stress
v_i^σ	crack surface displacement due to local stress
w	bulge displacement in z-direction
w_c	bulge deformed shape amplitude
x	co-ordinate perpendicular to load direction from notch center
y	co-ordinate parallel to load direction from notch center
z	co-ordinate perpendicular to laminate surface area and load direction
COD	crack opening displacement
CCD	crack closing displacement
DBZ	delamination/bulge zone
E	modulus of elasticity in direction of applied displacement

E_1 longitudinal modulus of elasticity of top sub-laminate

E_2 longitudinal modulus of elasticity of bottom sub-laminate

E_{11} ply longitudinal modulus of elasticity

E_{22} ply transverse modulus of elasticity

E_x laminate modulus of elasticity in direction of loading

F_h^S circular hole correction factor due to remote stress

$F_h^{\sigma_i}$ circular hole correction factor due to local stress

F_w^S finite width correction factor due to remote stress

$F_w^{\sigma_i}$ finite width correction factor due to local stress

G strain energy release rate

G_0 material intrinsic fracture energy

G_{12} ply in-plane shear modulus

G_{app} applied strain energy release rate

G_c laminate intrinsic fracture energy for kink-band growth or delamination

G_R strain energy release rate resisting crack growth

G_{SS} steady-state strain energy release rate

H panel height

H_c composite fracture parameter used in Mar-Lin correlation

K_∞^S SIF for a crack in an infinite plate without a hole due to remote stress

K_c intrinsic material fracture toughness

K_h^S SIF for cracked hole specimen due to remote stress

K_h^σ SIF for cracked hole specimen due to local stress

LDZ linear damage zone

P_{cr} critical load for plate to buckle

P_{fail} sandwich panel failure load

R notch radius

S applied remote stress

SIF stress intensity factor

T cohesive zone bridging traction

U stored elastic strain energy in laminate

U_{ub} stored elastic strain energy in laminate prior to buckling

U_b stored elastic strain energy in laminate after buckling

U_{el} stored elastic strain energy

U_{el}^{A} stored elastic strain energy in strip A

U_{el}^{B} stored elastic strain energy in strip B

V_f fiber volume fraction

W panel width (half-width in DZM model), work done on laminate

W^{A} work done on strip A

W^{B} work done on strip B

α kink-band rotation angle

β kink-band boundary angle

δ kink-band segment length

δa strip width in delamination/buckling model

ε applied strain

ε_{cr} critical applied strain for plate to buckle

ε_{back} far-field strain in back facesheet

ε_{front} far-field strain in front facesheet

λ ratio of sub-laminate to laminate thickness

ξ ratio of sub -laminate to laminate modulus

ν_{12} ply Poisson's ratio

σ stress

σ_{cr} critical stress for plate to buckle

σ_f far-field failure stress

σ_{fail} facesheet failure stress

σ_i cohesive zone bridging stress in segment i

σ_n notched laminate failure stress

σ_{prop} applied stress for damage propagation

σ_{un} un-notched laminate failure stress

Δa crack length, bulge length

Chapter 1

Introduction

1.1 Problem Statement: Composite Materials Today

The performance advantages promised by the use of composite materials in structural components are nowadays being limited by the large commitment of time and expense involved in their design, manufacture and in-service repair. For industries such as aerospace, this becomes an increasingly important factor in the material selection phase of design. This is particularly true of the commercial sector (compared to the military or space sectors) since if the performance gain does not justify the extra cost involved, the shift from metals to composites cannot be justified.

The use of composite materials in new aerospace applications is primarily due to their suitability for lightweight structures: they offer high strength and stiffness to weight ratios (compared to conventional metals), which are critical parameters in the design of structural components for aircraft. In addition, these materials offer the potential for tailoring their properties to specific functions. However, this potential for flexibility implies additional complexity in the design process for composite materials. Furthermore,

since composites are composed of two or more distinct materials, by their nature they are strongly affected by material discontinuities, inhomogeneities and anisotropy. These effects introduce failure modes which are specific to composite mechanical response (such as delamination) which need to be considered in addition to those which apply to monolithic materials.

Another aspect that makes composite design complicated is directly derived from one of the advantages mentioned above: the ability to create new structural properties by varying the laminate stacking sequence. Even though the materials used in each laminate may be the same, changing the ply orientations can radically change the mechanical response of a laminate.

Accurate determination of the service load cases is also of extreme importance in composite material design. The dependence of a laminate's mechanical properties on ply orientation and stacking sequence makes it crucial to know how the structural component is to be loaded before attempting to design for it to carry the loads and preserve structural integrity. Moreover, tensile and compressive loading cases will yield different mechanical behaviors, including but not confined to different failure modes.

In general, the prediction of and design against fracture requires analysis of very intricate, three-dimensional loading states at the micro- and macroscopic states, and the analytical solutions to the micro-mechanics involved in such problems are extremely complex. One-dimensional solutions are relatively simple, but they offer only a limited description of the true behavior. Two-dimensional solutions describe the problem better, but they introduce more analytical complications and still fall short of fully predicting the material's response to loading. Three-dimensional solutions would offer more complete solutions, but their implementation is computationally complex, even with the use of modern computers.

In any case, before attempting to develop models and design tools, the physics pertaining to the problem must be clearly established. In the particular case of composite

mechanical response, the failure modes occurring within the material must be determined before models for its mechanical failure are sought. For this reason it is logical to mechanically test a material and to determine the mechanisms driving its failure prior to seeking an analytical solution. The purpose of these initial mechanical tests is to understand how the material behaves under specific conditions. The observations should then be applied to create analytical solutions which can later be used to determine how that material will behave under service loading conditions, thereby introducing a predictive capability to the design of composite structural components.

One of the problems with the current composite design methodology today is that it relies heavily on mechanical testing. The complexity of analytical solutions often calls for assumptions and simplifications to be made which further increase the lack of confidence in the resulting solutions. The current response to this problem has been to introduce largely empirical models as design tools. Therefore, mechanical tests are very often used for verification as well as for design purposes. This only adds to the total cost of the design process, which hinders the possibilities of composite materials being economically viable.

It is very clear that in order for composite materials to be more widely used in the aerospace industry, a revision of their design methodology is necessary by which more emphasis is placed on truly predictive analytical solutions and less on mechanical testing. Such tests should be used to bring insight into the problem by revealing the physical mechanisms involved in the behavior of the material, not to calibrate a model designed to solve the very problem it was calibrated with. It is presumed that a proper description of the damage taking place will yield a more accurate model than one based on interpolation from test data.

The ideal goal would be for the designer to use mechanism-based models to make failure and durability predictions on a structural component, using only basic data about the material components (fiber, matrix and interface). Although this might be

pragmatically unfeasible, it is certain that significant gains can be achieved by working towards this goal [1]. This is the idea upon which this project is based.

1.2 Objectives: Sandwich Panels in Compression

There is a clear need in industry for models that predict composite mechanical behavior in an accurate, efficient and reliable manner. This need is particularly acute in cases where compressive loading dominates, where there has been relatively little prior research. The goal of this project is to observe and characterize the damage emanating from notch tips in composite sandwich panels when subjected to uniaxial compressive loads. The sandwich panels studied consist of two woven fabric reinforced laminate facesheets (three plies each) and a central non-rigid core. This testing configuration gives insight as to the damage behavior of sandwich panels under compression, which are used in aircraft secondary structures such as flaps, slats and fairings. Furthermore, it may provide information on the behavior of thin laminates under compression, which are used in multiple structural applications, but which cannot usually be tested at the coupon level in compressive loading due to global buckling.

For the sandwich configuration test to provide a faithful analogue to the behavior of a thin laminate, it must be demonstrated that the loading and boundary conditions experienced by each laminate are the same as if each laminate was tested on its own (i.e., no bending stresses are present). If the result is satisfactory, then the results from this research may be extended to thin laminates.

There is optimism that, by obtaining detailed information on the damage mechanisms occurring ahead of the notch tip, a physical basis may be provided to existing models – if the observed damage is consistent with models such as the Cohesive Zone Model, which is explained in detail in Chapter 2 – or applied to new modeling approaches. Whichever the case, a stronger basis for the design methodology of composite panels under compression will be the outcome of this work.

1.3 Approach: Damage Characterization

This research aims to develop a predictive model for the design of composite sandwich panels in compression through the introduction of a physical basis. Therefore, an accurate description of the damage occurring in the crush zone adjacent to the notch tips is at the core of this work. A series of damage evaluation techniques were used throughout this work, including destructive and non-destructive as well as *in-situ* and *post-mortem* observations. This approach provides various perspectives from which the prevalent damage mechanisms can be accurately characterized and consequently modeled, thus providing the desired physical basis to the model for the damage tolerance of sandwich panels.

1.4 Project Outline

In this study, sandwich structures composed of three-ply woven Graphite fabric reinforced facesheets and Nomex honeycomb core were tested to failure in uniaxial compression in an attempt to characterize the dominant damage mechanisms. Even loading of the two facesheets was essential in order to avoid bending stresses, and various methods were sought to accomplish acceptable alignment between the two panel faces. *In-situ* and *post-mortem* damage evaluation techniques were employed to both qualitatively and quantitatively describe the damage types detected, as well as the significant lengthscales and parameters.

The second part of the project was to model the observed failure modes in an attempt to predict the material's damage tolerant behavior. Direct observations from experiments were applied in the modeling phase to provide a physical basis for such models. The ultimate goal was to reduce the overall number of tests required prior to the introduction of a new material. This will be demonstrated by improving the predictive power of models for the particular case of damage tolerance of honeycomb sandwich panels.

Chapter 2

Literature Review

2.1 Introduction: Composites versus Metals

In the aerospace industry, a wing's structural integrity is as important as its aerodynamic properties. It is vital in the design of an aircraft to understand the structural requirements of every component and verify that these are met.

Metals have been used in aircraft components for more than 70 years, and their mechanical behavior is well established. Isotropy simplifies analysis considerably, and the yield and fracture mechanics of metals are reasonably well understood and can be applied reliably in the design of metallic components. A set of standards exist by which structural components are designed, and this has become a relatively automated procedure: a designer can refer to data book properties derived from tests performed on the metal to be employed and can then apply them to the part being designed, accounting for the local stress state and functional requirements.

The introduction of composite materials, however, has complicated the design of structural components. The flexibility available in the fabrication of these materials, and the complexity in their mechanical behavior due to their anisotropy, has kept researchers busy working on models to predict their structural performance. Flexibility translates into an endless number of different materials that can be manufactured using the same fiber and matrix components. Anisotropy and heterogeneity translate into multiple failure modes which cannot be adequately described by conventional plasticity theory or fracture mechanics. Combining these two factors results in a requirement for a different approach to structural composite design.

Various notched specimens are widely used by industry as a limiting test condition for the structural performance of a component. The three-dimensional stress concentrations introduced by notches in laminated materials, combined with the range of damage mechanisms by which such coupons can fail, makes the analysis and transfer of test data to the structural scale very taxing since conventional strength of materials or fracture mechanics cannot be directly applied [2-4]. A series of different approaches have been sought, some of which are described in the following sections.

2.2 Damage Tolerance

Given the inevitability of structures sustaining damage in service (due to impact events, lightning strikes, fatigue, corrosion, etc), the damage tolerant design methodology focuses on providing structures with the capability to perform in a damaged state. Fracture mechanics analyses have been developed for metallic structures that provide reasonably accurate predictions to support damage tolerant design [5]. However, these models rely on assumptions of isotropy and the application of continuum mechanics, which are appropriate for metals but which cannot be directly applied to composite structures. The main obstacle is the multiple damage mechanisms occurring in composites, which make it intractable to explicitly model the initiation and growth of

each individual component of the damage and its effect on the overall structural integrity of the component [6].

Another reason why the well-established fracture mechanics approach to damage tolerance of metals cannot be applied to composites is one of dimensions. It is inappropriate to use continuum mechanics to analyze a situation in which the lengthscales of the individual damage mechanisms are comparable to those of the structure. This is the case in composite materials, for which the damage zone can grow to the same order as the in-plane structural dimensions (hole size or ligament width), and is composed of individual cracks (e.g. delaminations) that can exceed the through-thickness dimensions of the laminate [6].

For the above reasons, considerable effort has been devoted to trying to simplify the damage state around features such as notch tips to permit damage tolerance analysis. Many researchers have adopted an approach of merging all the failure mechanisms into a single "damage zones". These are described in detail later in this chapter.

There are a number of such models that aim to facilitate damage tolerant design of notched laminates loaded in tension [7-11]. Some even describe in detail the physical mechanisms involved, such as the increased fracture resistance induced by fiber bridging along a crack emanating from an open hole specimen in tension [2-4]. Most of these studies acknowledge the different damage mechanisms occurring in the area adjacent to the notch tip, and that it is a combination of these that leads to final failure [2]. However, since most of these contemporary models rely on extensive mechanical testing for their calibration, a model that efficiently predicts the damage tolerant behavior of a composite panel is yet to be developed. This is particularly the case for compressive loading cases, for which the understanding of damage growth is substantially less than for tensile loading cases.

2.3 Sandwich Panels

2.3.1 Applications

The use of sandwich structures in the aerospace industry is extensive, and interest in their employment has evolved over the past decades with the introduction of composite materials for the facesheets and non-metallic honeycombs and plastic foams for the core [12]. The increase in bending stiffness and reduction in weight which sandwich panels permit have motivated designers to use them as primary structures in airplanes such as the Beech Starship, as well as their established use as secondary structural components (such as for wing flaps and fairings) in commercial passenger aircraft [12,13]. Compressive loading is inevitable in most aerospace structures, and buckling of panels is therefore a primary concern [12].

2.3.2 Failure Modes

Three types of failure have been typically associated with sandwich panels loaded in compression: core failure, core-facesheet debonding and facesheet fracture [12]. Early on in their application, it was realized that one of the most common failure modes involved failure via the occurrence of a short-wavelength instability. This local buckling was termed "wrinkling" [13]. Initial analyses of this failure mode regarded facesheets as perfectly flat, treating the wrinkling as a bifurcation problem in which no out-of-plane deflections were allowed until some critical compressive load was reached. Only then would the facesheets buckle locally in a symmetric or anti-symmetric mode [14-18]. However, it was soon realized that, due to imperfections introduced during the manufacturing process, the fabricated structures would usually exhibit a small amplitude waviness that would lead to failures at loads significantly lower than those predicted by the analysis assuming perfectly flat facesheets [13]. These initial out-of-plane imperfections have been found to have an important effect on the final failure load for thick panels but only a small influence on thin ones [12]. More recent work has developed more accurate models for the effect of waviness and examined the various

failure modes that may arise in a wavy facesheet under compression (core tension, shear or compression; adhesive tension or shear; and facesheet bending) [13].

2.3.3 Alignment

One of the most disputed aspects of sandwich panel testing has been that of determining whether the loading fixture produces acceptable data. The main concern is the possibility of unequal loading of the two facesheets. Some researchers argue that the sandwich panel configuration provides nothing more than a means by which to test extremely thin laminates without the need for anti-buckling devices [19]. Other workers suggest that sandwich specimens exhibit a higher longitudinal compressive strength than conventional composite coupons [20]. The effect on sandwich panel stiffness introduced by the central core is still not fully understood.

Unequal loading of the facesheets introduces bending stresses, which affect the outcome of the test in a variety of ways. For example, observed damage modes may no longer be due to uniaxial loading alone, but to a combination of uniaxial and bending stresses. Improper coupon alignment with the loading direction renders such tests useless, so it is necessary to apply the same loads to both facesheets to within a specific degree of accuracy. This is set by the ASTM Standard C-364 [21] for edgewise compressive strength of sandwich constructions, which states there must be under 5% difference in the strain levels measured for each facesheet in the early stages of loading.

2.4 Compression Strength and Failure

2.4.1 Approach

The longitudinal compressive strength of unidirectional composites depends on many factors including the stiffness and strength of the matrix and fiber. Better understanding of compressive failure mechanisms is needed to more accurately predict

strength changes resulting from the use of different resins and fibers [22], or from stacking sequence variations. Composite architecture plays an important role in the damage mechanisms occurring prior to catastrophic failure as well as the notched or unnotched strength of the material.

Over the past two decades, much effort has been concentrated on understanding the failure mechanisms and predicting the strength of compression loaded laminates [22]. Changes in material properties or the presence of defects introduced in manufacture may lead to a range of failure modes. Consequently, an analytical model accurate for one material system may not predict failure for another one. A comprehensive model that works for different failure modes and material systems is not accessible at the moment, so the current approach is to identify critical failure modes (and their respective sequence and contribution towards final failure) for each material system and to develop an appropriate model for each failure mode [22]. Therefore, models that describe a sequence of failure initiation and propagation must be based on observations of the damage, both prior to and after catastrophic failure.

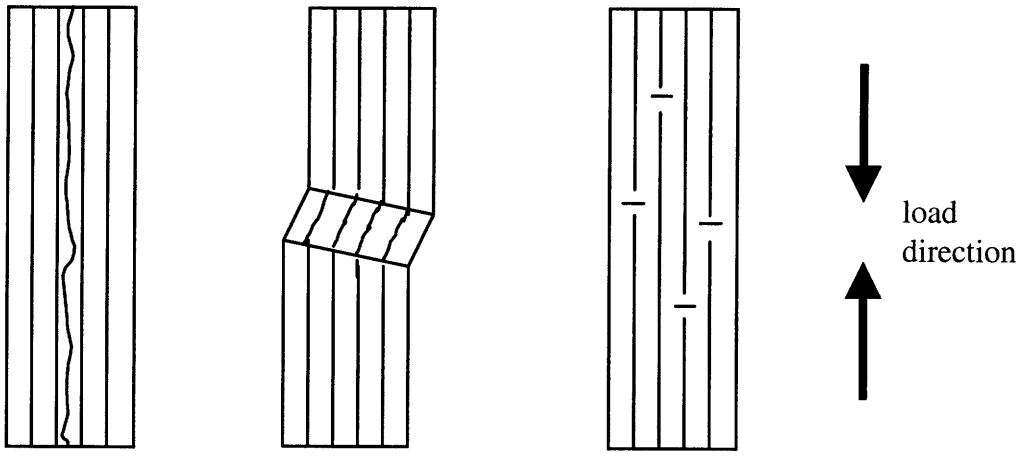

Figure 2.1: Unidirectional composite compression failure modes [22].

2.4.2 Damage Mechanisms

The stacking sequence of a laminate is one of the major causes for variation in failure mechanisms, the others being ply level properties and load case. In unidirectional composites, it is not uncommon to observe fracture along the fibers (i.e. within the matrix) and in the fiber/matrix interface due to their respective weakness compared to the strength of the fibers [22].

Transverse tensile stresses develop in the matrix due to Poisson's ratio differences between matrix and fiber, and stress concentrations caused by voids can initiate fracture in the fiber/matrix interface [23]. When embedded in a ductile matrix, fibers can fracture in bending, causing an eccentricity that may lead to longitudinal splitting with continued compressive loading (Fig. 2.1a).

A more common failure mode of composites, associated with fiber buckling and kinking, is shear crippling (Fig. 2.1b). Macroscopically, shear crippling appears to be similar to a shear failure on a plane at an angle to the load direction. Microscopic inspection, however, indicates that this type of failure is frequently the result of kink-band formation (Fig. 2.2).

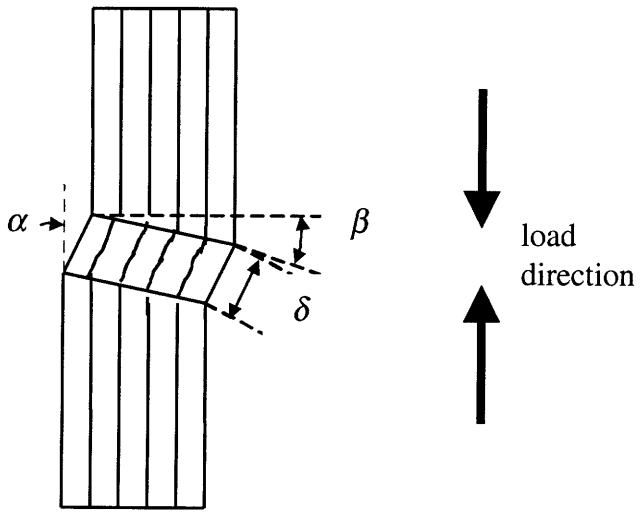

Figure 2.2: Kink-band geometry.

Kink-band boundary angle (β) and segment length (δ) values can vary depending on the material system, and even for similar material systems their values are not consistent, since they depend on the load history [22]. Fiber breaks are typically observed at the kink-band boundaries in Graphite fiber composites, whereas Kevlar and Glass systems exhibit fiber kinking and extreme fiber bending respectively. Kink bands are best observed in specimens and applied loadings that result in a gradual failure, i.e. when damage growth has taken place in a controlled manner. Such gradual failure is sometimes fostered by a gradient in the stress field such as that present near a hole [24].

Another failure mode of composites is associated with pure compression failure of fibers (Fig. 2.1c). In this case, the fracture surface is typically at an angle of about 45° to the loading direction. However, *post-mortem* examination of fracture surfaces of Graphite/Epoxy composites alone are not sufficient to determine whether the failure mode prior to catastrophic failure is fiber kinking or fiber compression failure because the fiber segments resulting from kinking tend to be randomly displaced during crushing of the laminate.

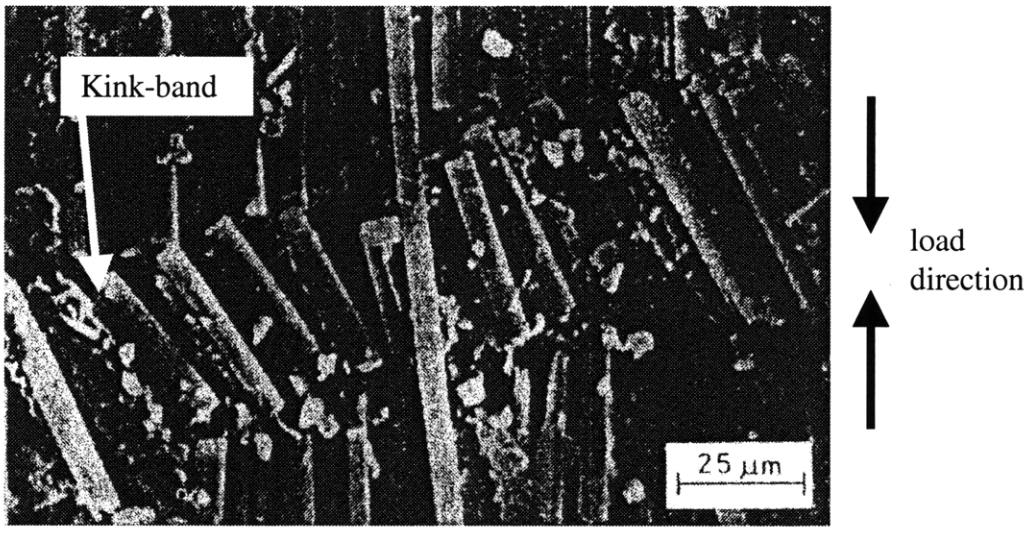

Figure 2.3: Scanning electron micrograph showing fiber micro-buckling [28].

Most of the work performed in this area suggests that the most likely critical failure mode in Graphite/Epoxy laminates is shear crippling involving fiber kinking (or micro-buckling) in the 0° plies [22,25-27]. The sequence of events is generally thought to be as follows: compression induces kinking of a few fibers, which in turn disrupt the stability of the neighboring fibers so that these also fail in the kinking mode. This damage propagation process continues until the composite completely fails [22]. Figure 2.3 shows a micrograph of a kink-band.

The majority of researchers agree that fiber micro-buckling is the driving mechanism for catastrophic failure of notched laminates loaded in compression. Some argue that this failure mode is initiated as matrix cracking, and that with increasing load, fiber micro-buckling, surrounded by delamination occurs at the edges of the notch and at locations of high in-plane compressive stress [28,29]. Others believe that an initial fiber misalignment and the shear yield strength of the matrix play a crucial role in the process of fiber plastic micro-buckling [30,31]. Still other researchers maintain that buckling, especially for small imperfections, is a theoretical upper bound for failure, and that interface failure occurs at much lower stresses for typical fiber reinforced polymers [32].

Not all work concentrates on describing the damage mechanisms taking place in the damage zone and developing an analytical model to describe it. Some recent work has produced an explicit equation for compression strength of unidirectional polymer matrix composites via the simplification of the exact solution [33]. This research claims that such a non-empirical formula can be used in the design of production parts without performing actual testing, or to estimate their compression strength. Only three parameters are required: the shear stiffness and strength of the composite and the standard deviation of fiber misalignment in the composite, all three of which can be measured by well-established experimental procedures.

Despite all the research performed in this area, and even though there is a good understanding of the key damage mechanisms that occur when composites are loaded in uniaxial compression, there is no design methodology able to predict with sufficient

precision what these failure modes will be prior to loading, and hence accurate prediction of compressive failure loads is still to be attained.

2.5 Damage Zone Modeling (DZM)

2.5.1 Approach

The damage state at the notch tip of a laminate loaded uniaxially is complex, consisting of various damage types occurring simultaneously and with high densities. The damage modes vary with material system, stacking sequence, and loading type. Developing analytical models to describe each of these failure modes is not difficult; in fact, there are well-established models which accurately describe fiber bridging, delamination growth, fiber kinking or matrix cracking, to mention a few. However, it has not yet been proved possible to link all these failure modes to account for the interactions between them. Apart from being a computationally taxing issue, the statistical uncertainty associated with composite mechanical behavior must also be taken into account. Addressing these problems at once becomes a daunting task which today seems unattainable, and this probably explains why researchers have simplified the situation at the notch tip as is explained in the following sections.

2.5.2 Cohesive Zones in Tension: Bridging Crack Tractions

Catastrophic failure in monolithic materials and some composites is often manifested in tensile tests by cracks that emanate from the notch tip and traverse the specimen's width in a direction perpendicular to the applied load. For homogeneous materials, no load is transferred across the crack, and hence the stress carried by the remaining intact material increases with constant load as the crack grows. For non-homogeneous materials, such as composites, the nature of the cracks may be entirely different. Continuous fiber composites (CFC's) loaded in tension sometimes exhibit the same crack-like behavior described above, with the marked difference that whereas the

crack will traverse through the matrix material, some of the fibers along the crack remain intact (Fig. 2.4). This is primarily due to the high strength/strain to failure of the fiber compared to the matrix or to the low fiber/matrix interface toughness, which favors debonding over fiber fracture.

Consequently, the surviving fibers along the crack are able to carry part of the applied load. These load-bearing fibers shield the intact material at the crack tip from part of the applied stress, which increases the load necessary to further propagate the crack. This behavior is called toughening of the material, and it results in a resistance curve (Fig. 2.5a) which describes the increasing strain energy release rate (G_R) needed to propagate the crack until a steady-state is reached [3,4,34].

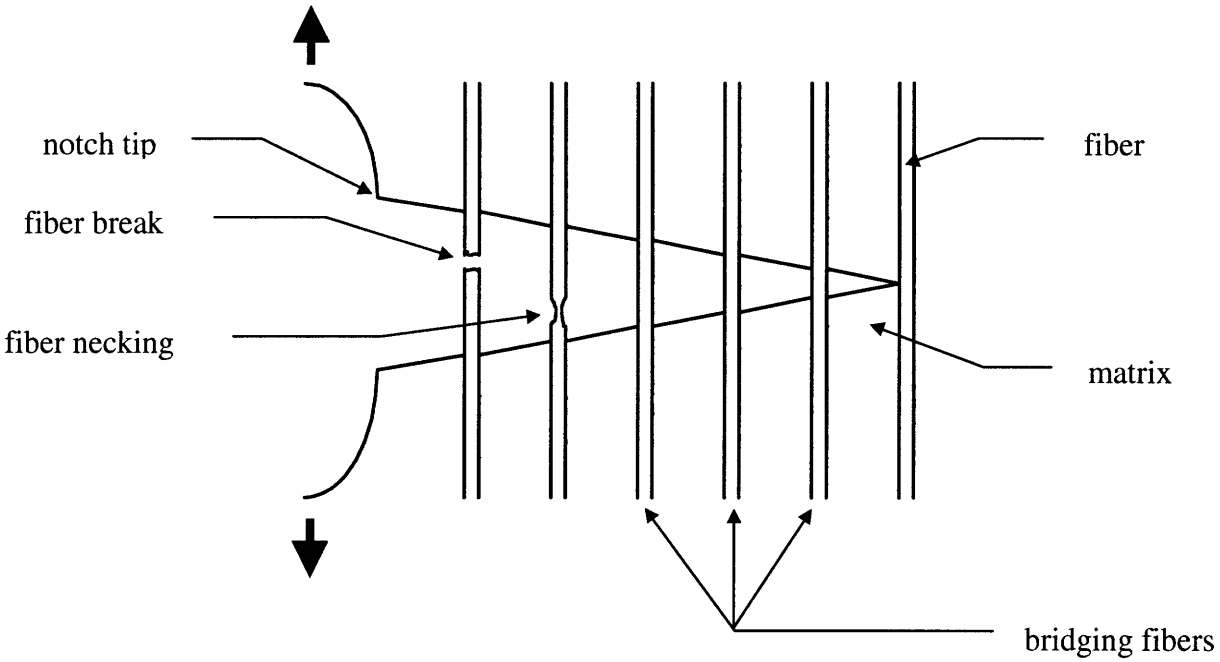

Figure 2.4: Fiber bridging in a composite loaded in tension.

To fully describe this cohesive zone, a bridging law is necessary to relate the crack opening displacement (v) to the stress (σ) carried across the crack at that crack opening displacement. The bridging law depicted in Figure 2.5b is of the strain-softening type, which implies that as the crack opens, the ability to transfer load across the crack decreases.

The critical crack opening displacement (v_c) symbolizes the point at which the bridging fibers no longer carry load, i.e. the fibers break. The energy required to propagate the crack increases because more and more fibers bridge the crack as it propagates – the material is being toughened. The steady-state (G_{SS}) is reached when the crack length (Δa) is such that for every new bridging fiber encountered by the crack tip one of the fibers in the wake breaks, so that the total number of fibers bridging the crack remains constant with increasing crack length.

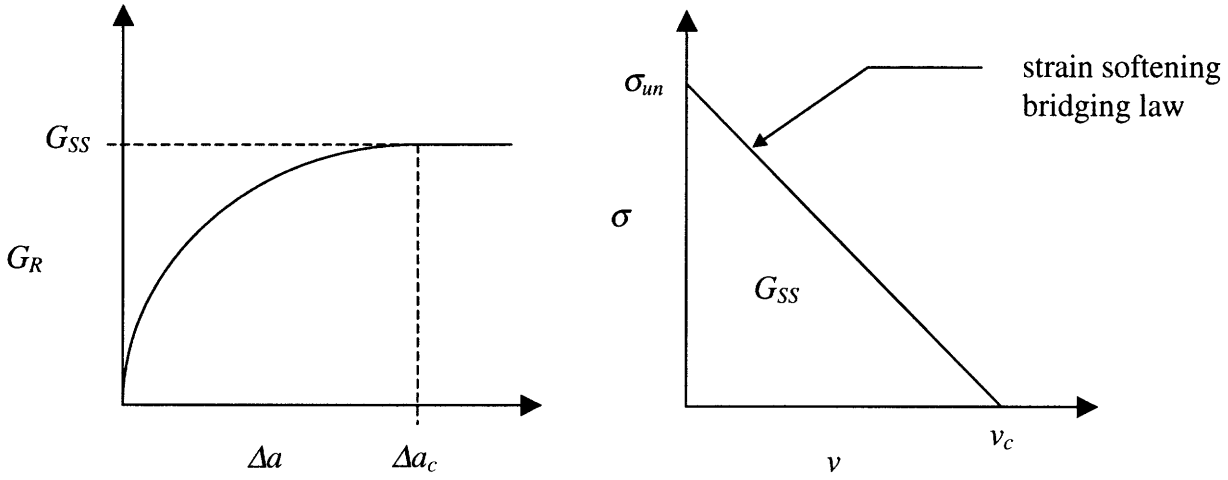

Figure 2.5: DZM resistance curve and bridging law.

2.5.3 Cohesive Zones in Compression: Crush Zone Tractions

Compressive failure of notched composite laminates is often preceded by the formation of a damage zone ahead of the notch which grows with increasing load [25,26]. The failure modes observed in the damage zone depend strongly on the lateral support provided by the matrix to the fiber during loading. In the absence of strong lateral support, all fibers would fail by buckling. However, as matrix stiffness increases, buckling is suppressed and the fibers tend to fail in shear. Data in the literature suggests that shear crippling involving fiber kinking (also called micro-buckling) is the most common compression failure mode in Graphite/Epoxy composites [22]. This micro-buckling is often surrounded by areas of extensive delamination [28,29].

In an attempt to make use of the well-established cohesive zone model developed for tension tests, researchers have developed analogous models for damage growing in compression [25-29,34,35]. Two fundamental observations validate this approach: (1) the crush zone observed in compression tests is macroscopically similar to the cracks seen in tensile tests; (2) the crush zone has been proven to transfer loads in a similar manner to the bridging fibers in the tensile tests [26]. Although the mechanisms involved in the damage propagation and in the load transfer are not the same, it is reasonable to make the analogy depicted in Figure 2.6 based on the strong similarities between the two cases.

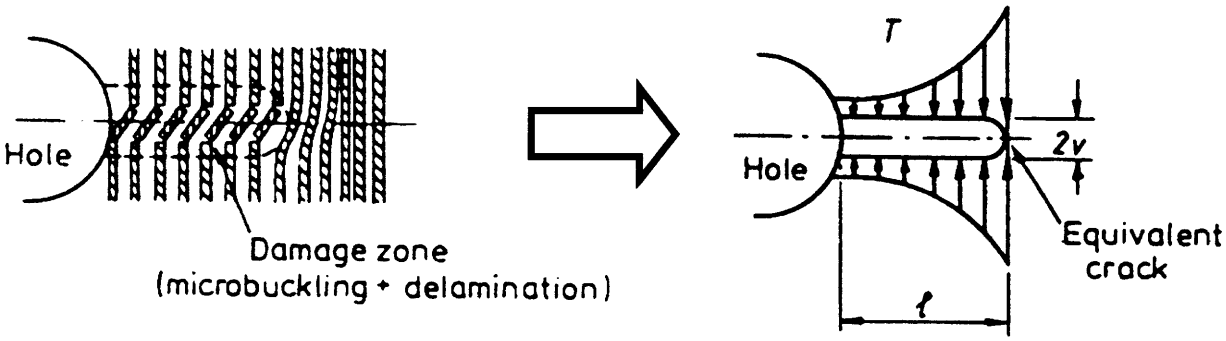

Figure 2.6: Cohesive zone analogy for compressive damage [27].

Instead of a crack opening displacement there is a crack closing displacement, and instead of fibers bridging to transfer tensile stress there are micro-buckled fibers transferring compressive stress. When a certain crack closing displacement (v_c) is reached, the micro-buckled fibers no longer have load-bearing capability.

One last characteristic worth mentioning regarding cohesive zones is that the bridging laws (or traction laws) involved are ideally considered to be a material property. One measure of the total available toughening due to a given bridging law is the area under the σ-v curve (see Fig. 2.5b), which is equal to G_{SS}, the steady-state fracture energy of the laminate. Therefore, irrespective of coupon and notch size or geometry, the same law can be applied providing that the same material system is used, which makes it a potentially very powerful design tool.

2.6 Delamination/Buckling

One of the most common failure modes in laminated composite materials is delamination [28,29]. Large interlaminar stresses develop during loading, making the weak fiber/matrix interface (relative to the fiber) fail and causing plies to separate from each other. Delamination occurs both in tensile and compressive applied loadings, the latter being of particular interest for the present work.

When delamination occurs, the laminate is basically split into two or more sub-laminates, depending on the number interfaces that fail (Figure 2.7). The location of the delamination(s) determines the corresponding thicknesses of the resulting sub-laminates. This automatically reduces the bending stiffness of the sub-laminates and increases the likelihood of local Euler buckling. Thinner columns buckle at lower loads, hence local buckling of the thinnest sub-laminate is probable and thus must be monitored.

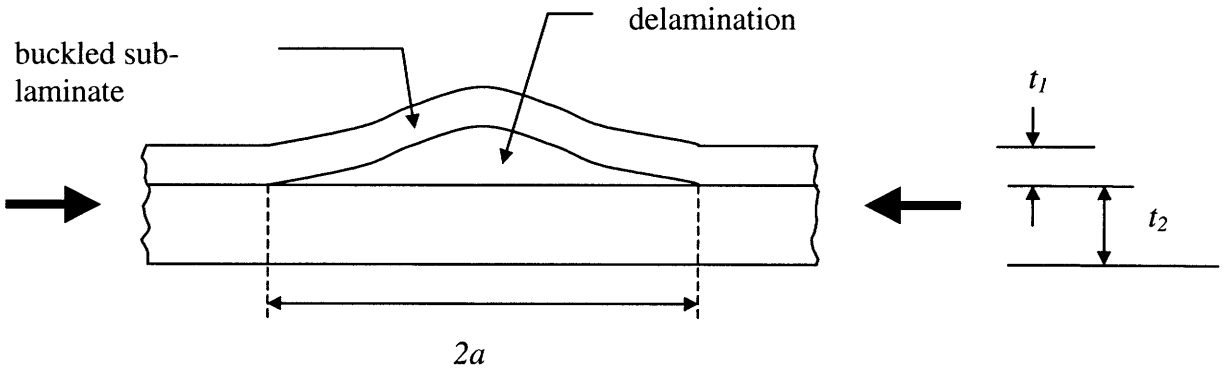

Figure 2.7: Delamination-buckling problem geometry.

Buckling in the presence of a delamination [36] and the propagation of this delamination in the direction parallel to load application has been analyzed in previous studies [37-39]. Buckling and post-buckling analyses reveal that, in the case of a short and thick delamination, the buckling load of the delaminated beam is a close lower bound to the ultimate axial load capacity. In the case of a relatively slender delamination, the post-buckling axial load can be considerably greater than the buckling load, and the ultimate failure of the beam may not be governed by delamination growth [39].

Further work in this area has recently concerned researchers with the effects of three-dimensional reinforcements in the laminates (e.g. fiber stitching). Such reinforcements, which are typically composed of fibers running through the laminate thickness, provide a restoring traction opposing the deflection of the delaminated layer adjacent to the crack [40-42].

Detailed analysis of the delamination propagation involves a balance between the strain energy stored in the buckled and in the intact sub-laminates, and the energy necessary to create new crack surface [41]. The Griffith condition for fracture is:

$$\frac{d}{da}[U_{ub} - U_b] = 2G_c \tag{2.1}$$

where a = half the crack (delamination) length, U_{ub} = strain energy stored in the thin laminate before buckling, U_b = strain energy stored in the thin laminate after buckling, and G_c = delamination fracture energy associated with delamination.

This delamination/buckling problem is very relevant to the work performed here because it can also describe the mechanical response of the crush zone described in the previous section. If delamination is already present in the material, or if it happens due to the compressive load applied, the thin sub-laminate is prone to buckle in the manner described above. This failure mode is consistent with the cohesive zone assumption that load is transferred across the damage: part of the laminate cross-section is intact, and the part that is buckled is still able to carry some load (its buckling load).

However, one must bear in mind that damage propagation in the cohesive zone model is *perpendicular* to the load direction, whereas the delamination propagation described in this section is *parallel* to the load direction. There was no work found in the literature describing in detail the propagation, perpendicular to load direction, of a delamination/buckling failure mode emanating from a notch. This new problem is of great interest in this work since this failure type was one of the observed modes, as

explained in Chapter 4. Most of the previous research in this area can be applied, but further modeling is necessary to describe this type of damage propagation in notched composite panels.

2.7 Notch Size Sensitivity

A common trend exhibited by composite laminates loaded uniaxially is a decrease in the notched strength with increasing notch size. Experimental data points are bounded by simple criteria based on notch sensitivity [43]. If the material is notch insensitive, the failure stresses are directly proportional to the reduction in cross-sectional area, while if the material is notch sensitive then it is postulated that the material fails when the stress concentration at the hole edge equals the failure stress of the material [19].

Composite materials often exhibit behavior in between these two bounds, indicating that the material is not ideally brittle and that some load redistribution does occur around the hole. This behavior has been reproduced by many researchers using the cohesive or damage zone modeling approach described in section 2.5, and is depicted in

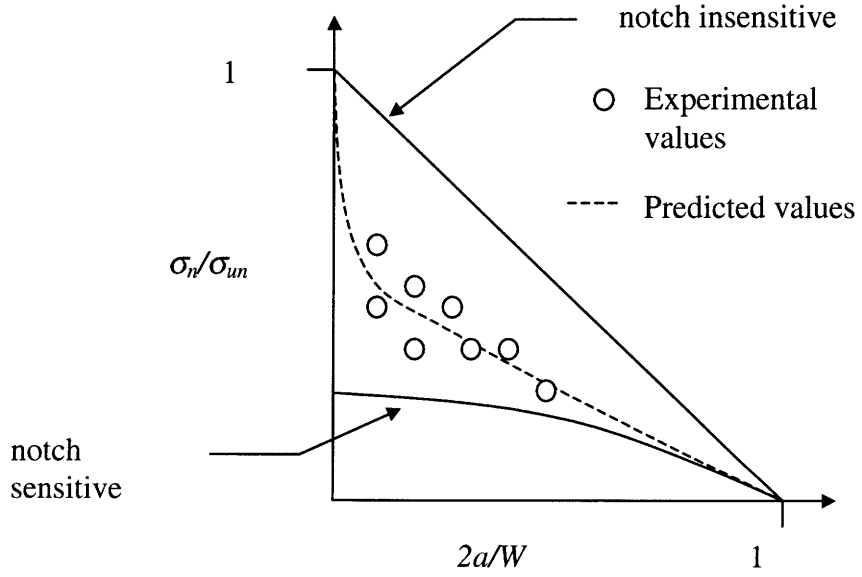

Figure 2.8: Notch sensitivity effect on ultimate failure stress [27-29,34,35].

This notch size effect has also been observed and predicted with correlations such as the Mar-Lin approach, which relates the un-notched strength of the material to the notch size via a toughening parameter and an exponential (Figure 2.9) [44]. Although this method is highly empirical, it produces the expected notch size effect from laminated notched composites loaded in compression.

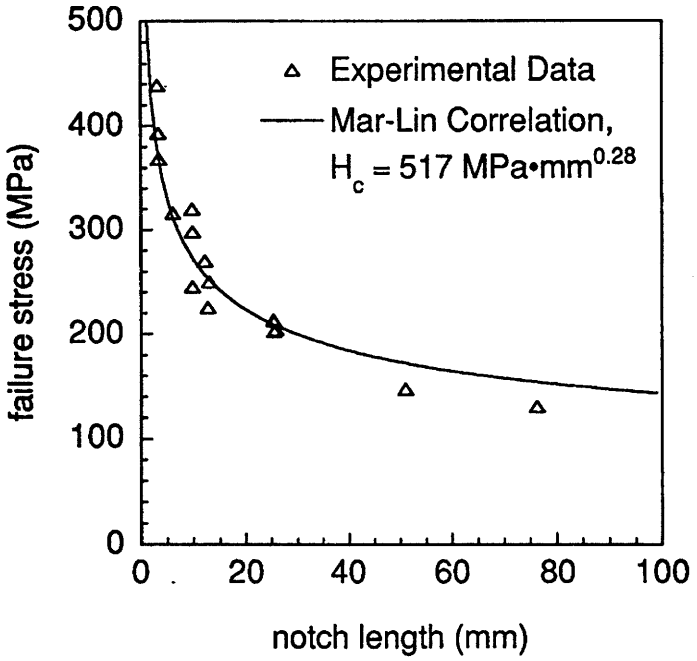

Figure 2.9: Correlation of notch size with ultimate failure stress [44].

2.8 Summary

A series of important points can be extracted from this literature review, the first being that there is a clear need for accurate and predictive models for the design and implementation of composite structural parts. Damage tolerant design demands that a structural component be able to perform in a damaged state, but in order to do so the mechanisms by which composites damage, and subsequently fail catastrophically, need to be fully understood and modeled. The increasing use of sandwich-type structures in aerospace components further requires proper testing and damage evaluation of such configurations. However, compression failure of composite laminates is extremely

complex, occurring by multiple and simultaneous failure modes that are not amenable to simple models. It is here where models of the cohesive zone type, which simplify the damage state at the notch tip by lumping all failure modes into one form of damage, become relevant. Such models have been satisfactorily implemented in tensile as well as in compressive loading cases, yielding predictions in good accordance with experimental results. A modeling approach which has not been applied to damage propagation of notched composites loaded in compression is the delamination/buckling problem, despite the fact that damage observations reveal consistent behavior with this model. This deficiency is acknowledged and the focus of this work is to implement this new type of modeling approach.

Chapter 3

Experimental Procedure

3.1 Test Specimens

3.1.1 Sandwich Material Specifications

All material was manufactured and supplied by Boeing Commercial Airplane Group (Stress Methods and Allowables Group). The facesheet material was denominated M3 by the manufacturer; its ply properties are listed in Table 3.1. It consisted of a plain weave, 3K tow, T-300 Graphite fiber fabric (BMS8-2121 Boeing specification) cured at 350°F, embedded in an Epoxy matrix. The core material was 1" thick Nomex (3 pcf).

E_{11} (GPa)	E_{22} (GPa)	G_{12} (GPa)	ν_{12}	t (mm)
57.2	57.2	4.8	0.06	0.211

Table 3.1: M3 material ply properties.

Two series of coupons were tested in this work, both made from the same material type but having different stacking sequences. The two layups were

[45/0/0/core/0/0/45] and [0/0/0/core/0/0/0] – they will be denominated as the "T45 Series" and the "T0 Series", respectively, throughout this manuscript for simplicity.

For both series, the two facesheets exhibited a marked difference in their texture when inspected with the naked eye: one was smoother than the other. This distinction was introduced during the manufacturing process, in which one of the sides was placed against a cure plate and the other was not. For purpose of referencing, the "smooth" and "rough" sides will be referred to as "front" and "back", respectively.

3.1.2 Coupon Geometries and Nomenclature

Tests were performed on three rectangular coupon geometries (prescribed by the company supplying the material) with through the thickness center slits. These geometries will be called "Small", "Medium" and "Large" respectively throughout this manuscript for simplicity (see Figure 3.1 and Table 3.2).

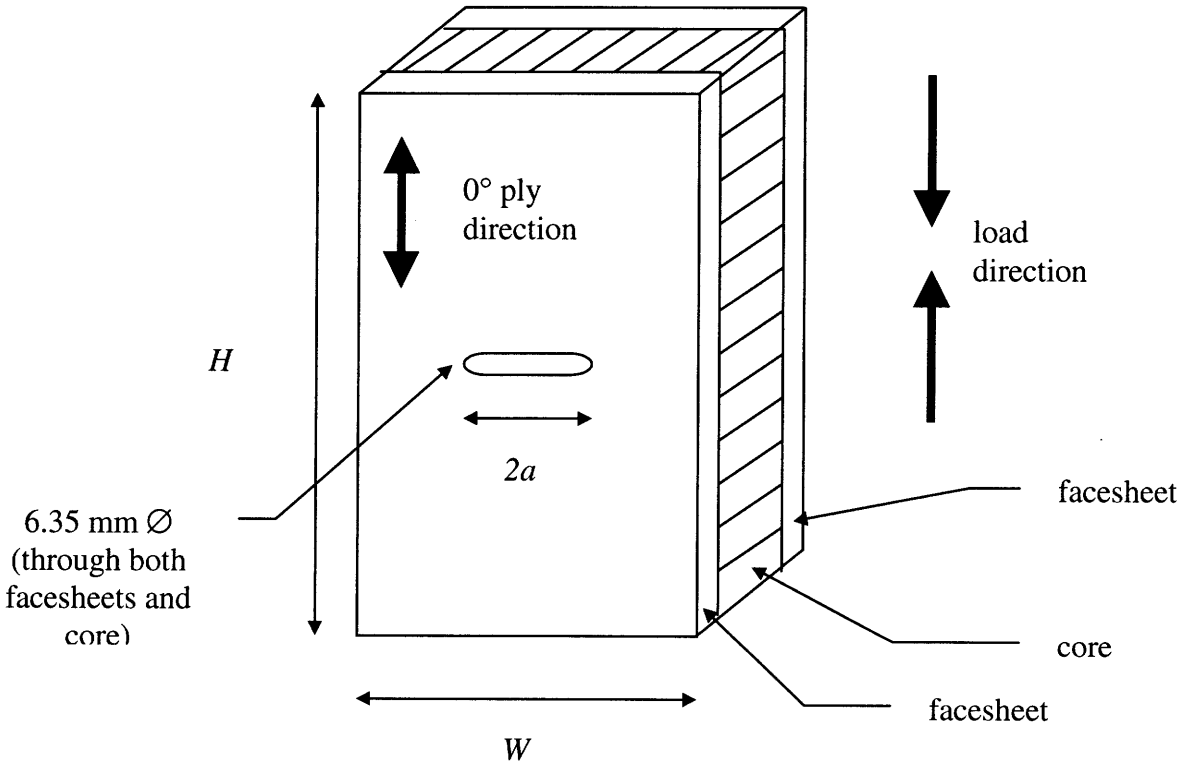

Figure 3.1: Test coupon configuration.

Nomenclature	$W \times H$ (cm)	$W \times H$ (in)	$2a$ (cm)	$2a$ (in)
Small	50.8 × 152.4	2 × 6	12.7	½
Medium	101.6 × 304.8	4 × 12	25.4	1
Large	203.2 × 406.4	8 × 16	50.8	2

Table 3.2: Specimen nomenclature and dimensions.

Material was supplied in large panels (40.68cm×82.55cm for the T45 Series and 40.68cm×92.71cm for the T0 Series). A cutting plan was developed to maximize the number of coupons obtained from each panel, having a minimum of two of each configuration.

T45 Series		T0 Series	
Coupon Name	**Dimensions**	**Coupon Name**	**Dimensions**
AS1	Small	BS1	Small
AS2	Small	BS2	Small
AS3	Small	BS3	Small
AS4	Small	BM1	Medium
AM1	Medium	BM2	Medium
AM2	Medium	BM3	Medium
AM3	Medium	BM4	Medium
AM4	Medium	BM5	Medium
AL1	Large	BL1	Large
AL2	Large	BL2	Large

Table 3.3: Test coupon nomenclature and description.

This quick explanation of the nomenclature in Table 3.3 will help identify each coupon throughout this manuscript:

A → T45 Series

B → T0 Series

S → Small coupon geometry

M → Medium coupon geometry

L → Large coupon geometry

3.2 Test Equipment

3.2.1 Load Frame

The setup employed for all tests was a 100 kN MTS load frame, equipped with an 8500 Plus Instron controller. Circular compression platens (22.86cm diameter) were used to enable uniaxial compressive testing. The bottom platen was fixed, whereas the top platen was self-aligning. Figure 3.2 depicts the test setup.

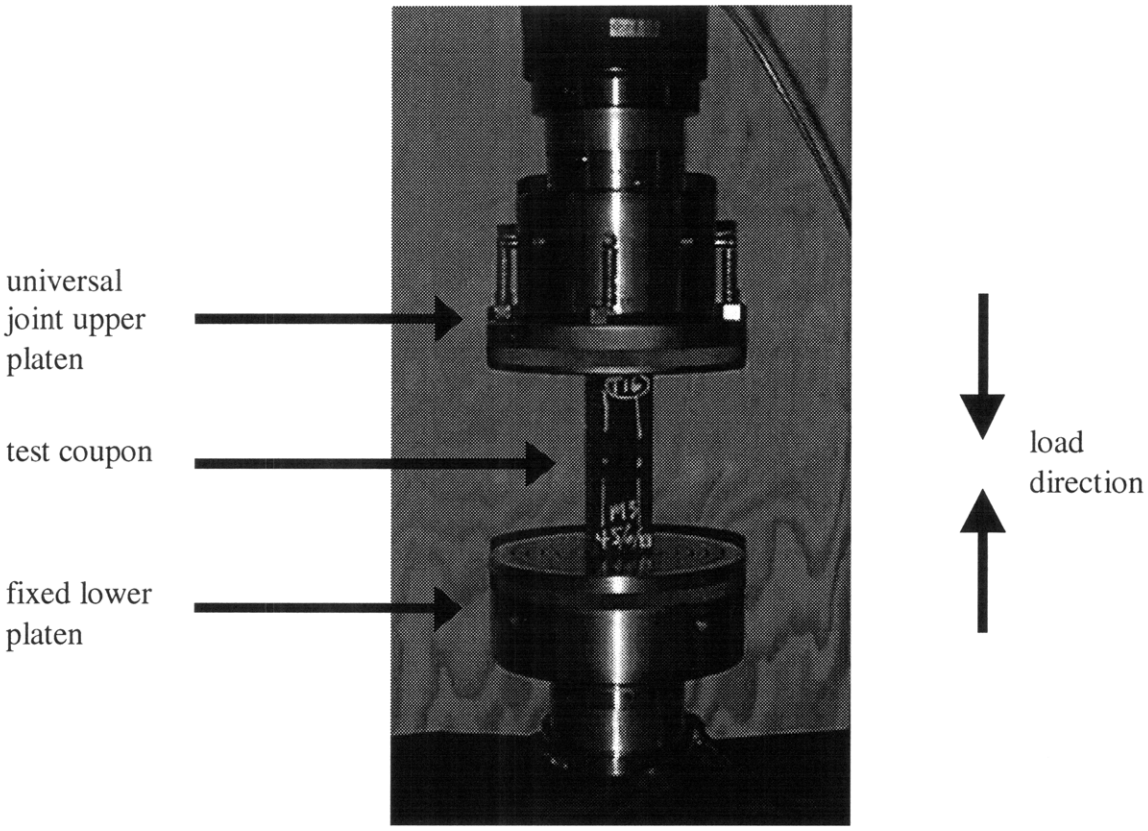

Figure 3.2: Test setup.

3.2.2 Strain Gauges

Strain measurements were taken during the tests with two objectives: first, to verify alignment for each individual test; second, to measure strain levels in the damage

zone around the notch. Figure 3.3a depicts the strain gauge positioning used to monitor alignment on each test. The intention here was to measure the strain levels on the two sandwich facesheets at the same location, and compare them in order to quantify the bending strains created due to misalignment. Locating the strain gages in the area affected by the notch tip stress concentration [5] would mean that the gages would have to be located in exactly the same position on both facesheets, since stress (and hence strain) can vary significantly over a few millimeters inside this area. In practice, locating the gages with such precision is very difficult. For this reason, it was decided to locate the alignment monitoring gages away from this stress concentration area: midway between the edge of the notch and the edge of the specimen in both directions.

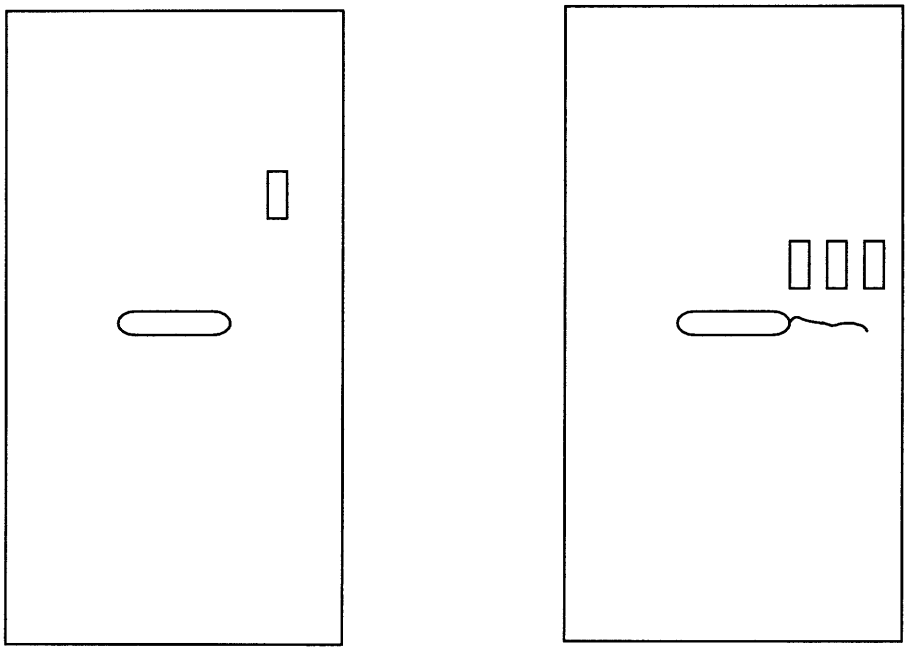

Figure 3.3: Strain gauge positioning.

Figure 3.3b shows the approximate locations of strain gauges used to monitor strain levels in the damage zone. The gauges were placed directly above the observed damage in order to monitor strain (and hence stress) transmission across the damage zone. Therefore, the gauges were only located on one facesheet, and only on the side of the notch which exhibited controlled sub-critical damage (see Section 3.4 below).

3.2.3 Data Acquisition System

Both strain and load were monitored during each test. Strain measurements from the strain gauges were directed to a strain gauge conditioner, which was connected to a breakout box. Load measurements from the testing machine were directed to the same breakout box. All strain channels (which varied from two in alignment tests to five in damage zone calibration tests) and the load channel were then directed to an Analog/Digital board inside a computer. LabView™ software was used to display and save the data. Figure 3.4 depicts the setup.

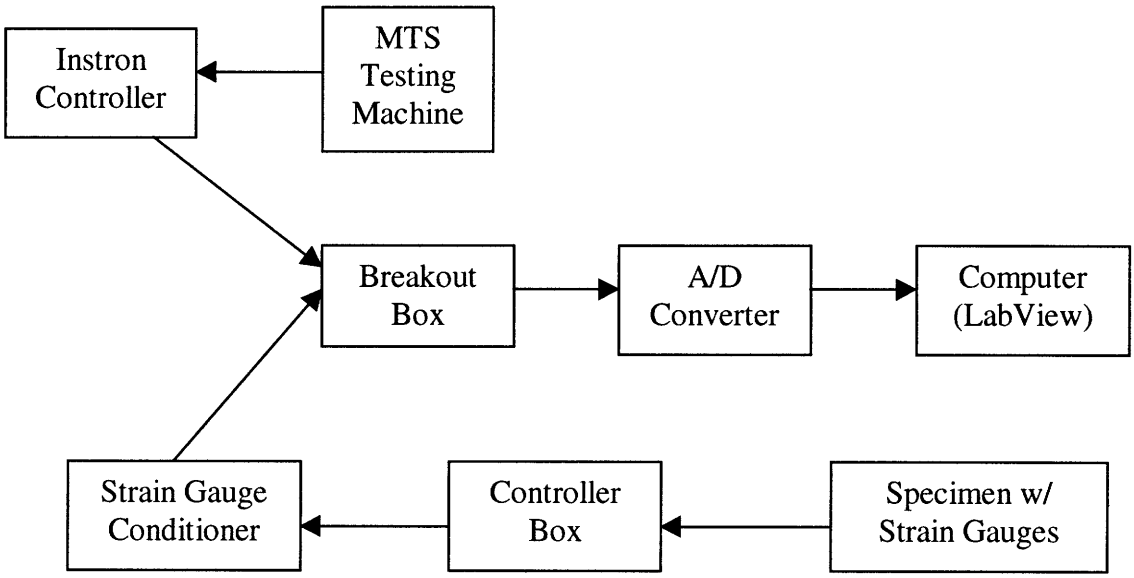

Figure 3.4: Data acquisition setup flowchart.

3.3 Test Procedure

3.3.1 Preliminary Testing

The first test of each coupon type was used as a trial run. These fulfilled several purposes. First, they provided approximate load ranges for sub-critical damage initiation and catastrophic failure, thus giving an idea of when to expect damage formation and

final failure in similar subsequent tests. Second, after inspection, they revealed the typical damage modes for each specific coupon type, something which cannot be directly inferred just from material properties and laminate layup. Moreover, this is one of the direct goals for this project. Third, they helped in deciding upon appropriate loading rates for subsequent tests of the same coupon type. By knowledge of the crucial loads, it was possible to plan ahead every test and slow down the loading rates accordingly as these loads were approached.

Subsequent testing proved that the observations made in these preliminary tests were quite reproducible. For the most part, each coupon type exhibited consistent behavior as far as damage modes and failure loads are concerned. So, besides providing one more data point for each coupon type, these "guinea pig" tests rendered a good insight as to what to expect on every successive run.

3.3.2 Sub-critical Damage

The principal focus of this work was to obtain, control, observe and characterize sub-critical damage emanating from the notch tip of sandwich panels due to uniaxial compressive loading. The preliminary tests discussed in Section 3.3.1 revealed that some of the panels tested exhibited "brittle" compressive behavior; i.e. catastrophic failure occurred suddenly, with little or no sub-critical damage growth. Furthermore, it was not uncommon for the panels to continue failing under decreasing loads; i.e. if any sub-critical damage was observed, the damage would continue to propagate even though the load may have actually been decreasing. For these reasons it was important to perform the tests in displacement control, and at very slow loading rates, in an attempt to control any sub-critical damage that might occur.

3.3.3 Coupon Alignment

In compression testing of sandwich panels, alignment is of critical importance to ensure the validity of the resulting data: the same load must be applied to both facesheets.

Using flat compression platens on both ends makes it even more taxing to obtain acceptable coupon alignment. Clearly, any imperfections of the coupon such as unequal facesheet lengths or nonparallel edges will introduce undesired effects, in particular bending stresses.

Normally, when a coupon was placed on the platens ready to test, the axial strain gauges showed differences in strain levels from one facesheet to the other when a small load was applied, no matter how accurately it had been cut. As load was increased slowly, the difference between strain levels was maintained, meaning that mis-alignment (and hence bending stresses) would remain throughout the entire test if it continued to be carried out in that manner. A series of alternatives were sought in order to solve this problem.

Shimming has been used by some researchers to obtain proper alignment in sandwich coupons [13]. A small load was applied to the coupon, and strain levels were compared between front and back. When one of the facesheets exhibited less strain than the other, it implied that there was insufficient contact between the edge of the facesheet and the platen, resulting in uneven loading. To solve this problem, thin pieces of material were placed between the edge of the facesheet exhibiting less strain and the platen. Materials used for this purpose include rubber, cork and thin sheets of aluminum, each rendering different results.

It was subsequently discovered that such measures were unnecessary since the moveable top platen was sufficient to allow for adjustment to achieve alignment. Once the coupons were initially loaded and strain monitored and compared on front and back, the top platen could be manually adjusted to produce even load application, and hence equal strain levels on both facesheets. Although somehow crude, this method yielded the best alignment results, and had the extra advantage of not requiring any additional machining or equipment. This was the method used throughout this work to ensure acceptable alignment. In all cases, alignment within 15% was achieved, where the percentage difference is defined by:

$$\%\ Difference = \frac{(\varepsilon_{front} - \varepsilon_{back})}{(\varepsilon_{front} + \varepsilon_{back})} \times 100 \tag{3.1}$$

where ε_{front} and ε_{back} refer to strain levels in the front and back facesheets.

3.3.4 Loading Rates

Fracture of high strength composite laminates is often instantaneous and catastrophic, and therefore identification of critical failure modes is not easily accomplished [22]. This was corroborated by the observations made in the preliminary testing (Section 3.3.1). Consequently, keeping the loading rates to which the coupons were subjected low was a crucial factor to enable stable sub-critical damage growth. The aim was to keep the loading rates as low as possible to ensure that the specimens did not exhibit too brittle a behavior, but fast enough so that tests could be conducted in a timely manner. The loading rates employed on each coupon type were similar in magnitude, but the load ranges at which each loading rate was used varied according to the preliminary test observations. Tables 3.4 and 3.5 summarize the loading rates used for each coupon type, and the load ranges for which they were employed. Some slight variations were made during each test, depending on specific test conditions, but the tables give the general trend followed.

T45 Series			
Loading Rate ($mm\ hr^{-1}$)	**Load Range (kN)**		
	Small	**Medium**	**Large**
15.24	0 – 3.34	0 – 4.45	0 – 8.90
7.62	3.34 – 4.45	4.45 – 6.67	8.90 – 11.12
2.54	4.45 – 5.56	6.67 – 8.90	11.12 – 13.34
1.52	5.56 – Failure	8.90 – Failure	13.34 – Failure

Table 3.4: Loading Rates for the T45 Series.

T0 Series			
Loading Rate ($mm\ hr^{-1}$)	**Load Range (kN)**		
	Small	**Medium**	**Large**
15.24	0 – 4.45	0 – 6.67	0 – 13.34
7.62	4.45 – 6.67	6.67 – 11.12	13.34 – 17.79
2.54	6.67 – 8.90	11.12 – 13.34	17.79 – 20.02
1.52	8.90 – Failure	13.34 – Failure	20.02 – Failure

Table 3.5: Loading Rates for the T0 Series.

3.4 Cohesive Zone Measurements

3.4.1 Rationale

It is well-established that laminated materials are sometimes able to continue transferring load even in a damaged state. Such is the case of the intact fibers present in tensile cracks, which provide bridging tractions between the crack faces.

Compressive tests do not produce such bridged cracks. However, the resemblance of the observed macroscopic damage to that described by damage zone models (see Section 2.5) suggests that the same type of load transfer might be occurring in the specimens tested, even though the microscopic mechanism by which load is transferred is likely to be different to that observed in tensile cracks. Thus, the relationship between transferred load and crack closing displacement must be determined in order to proceed with the damage zone model. Cohesive zone measurements were only attempted on large panels since a greater extent of stable sub-critical damage was observed at this scale.

3.4.2 Preparation

Since it was not practical to place and monitor strain gauges at all four possible locations for sub-critical damage growth (two notch tips × two facesheets), the specimens

were loaded up at very slow loading rates, and when any sub-critical damage was visually detected, the test was stopped (Fig. 3.5a). Strain gauges were then positioned along the predicted damage path in order to measure strain levels directly above the damage as it propagated towards the edge of the coupon (Fig. 3.5b). The specimen was then re-loaded and damage was monitored as it traversed past the strain gauges, enabling precise measurements of the strain transferred (Fig. 3.5c). The numbers (1 though 5) refer to the strain gauge numbering sequence employed.

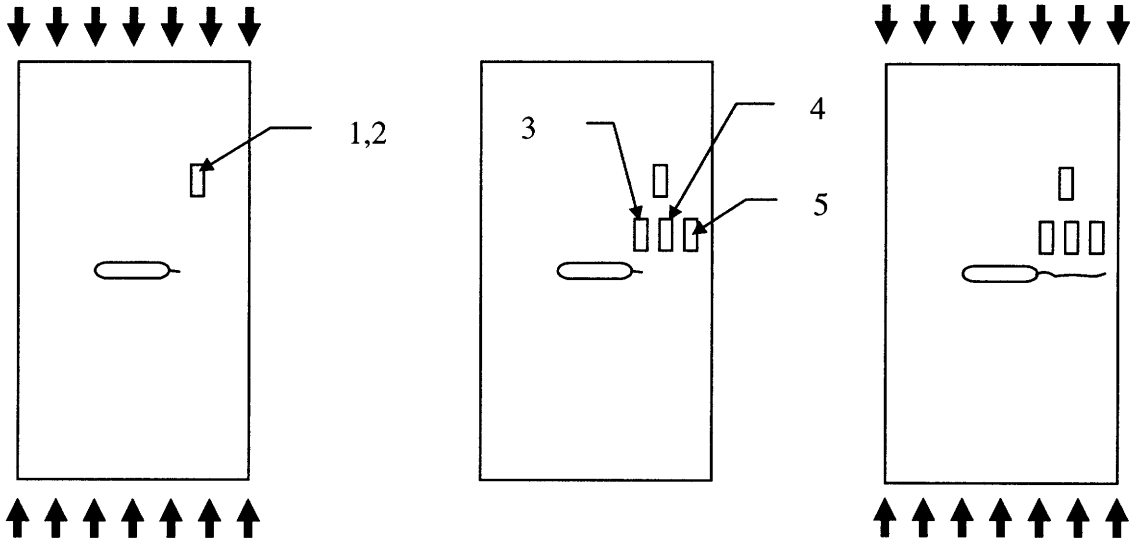

Figure 3.5: Strain gauge placing for cohesive zone measurements.

3.4.3 Procedure

Cohesive zone measurements were performed on two large panels (AL2 and BL2) since they exhibited extensive stable sub-critical damage growth. Loading was interrupted when a small crack was observed. Strain gauges were then located slightly above the anticipated crack path in order to monitor strain variation in the cohesive zone as the crack progressed (see Figure 3.5). The panels were then loaded again to failure in an attempt to grow the initial damage in a stable manner.

Strain measurements were correlated with applied load and damage length in order to provide a load transfer relationship for the DZM model. The results are further discussed in Chapter 4.

3.5 Non-Destructive Damage Observation

3.5.1 *In-situ Observations*

Qualitative as well as quantitative descriptions of the damage emanating from the notch tips were a crucial part of this project. There were two major sub-critical failure modes observed during testing: linear damage zones (LDZ's) and delamination/bulge zones (DBZ's). These are explained in detail in Section 4.2.3. Typical behavior of most of the coupons would include catastrophic failure of the facesheet that exhibited sub-critical damage during the test, which means that the area exhibiting sub-critical damage was crushed (and hence altered) after final failure. Therefore, damage measurements during testing were crucial to describe accurately damage progression.

In-situ measurements of damage in these specimens proved to be a rather difficult task for a variety of reasons. First, the surface of the facesheets was black, which made it difficult to identify where damage occurred. This was overcome by applying a thin coat of "white-out" prior to testing. When any type of damage occurred in the outermost ply, it would show very clearly as a break in the white-out coating. Second, because the material used was very brittle, and the tests were compressive, any slight contact with the facesheets near or around the damage zone during testing may have caused an instability sufficient to cause the entire panel to fail catastrophically prior to its intrinsic ultimate load. For this reason, measurements of crack and bulge dimensions during testing had to be taken extremely carefully. This was done in one of two ways: (1) if damage growth was sufficiently stable, direct measurements of the damage would be taken with a precision ruler; (2) if damage grew in a more unstable manner, a mark would be placed above the observed damage on the facesheet surface and measured *post-mortem*. In any

case, the data acquisition system (which monitored and recorded strain and load) was prompted whenever damage was observed (visually or audibly) in order to be able to correlate damage lengths with applied loads.

3.5.2 X-Radiography

Damage in composite materials occurs in a variety of ways, including but not confined to fiber breaks, delamination, matrix cracks or fiber kink bands. These are not always visible on the surface of the material, so damage may be present inside the laminate, yet not viewable. X-radiography is a powerful tool for determining non-destructively if there is damage below the material surface. Introducing a dye (which is opaque to X-rays) at the notch tip where damage was thought to be present and then taking a picture of the specimen would help to determine whether there was damage present or not. If damage was present, the dye would have been absorbed by capillary action into the cracks and/or delaminations, and the X-radiography would reveal its shape and extent.

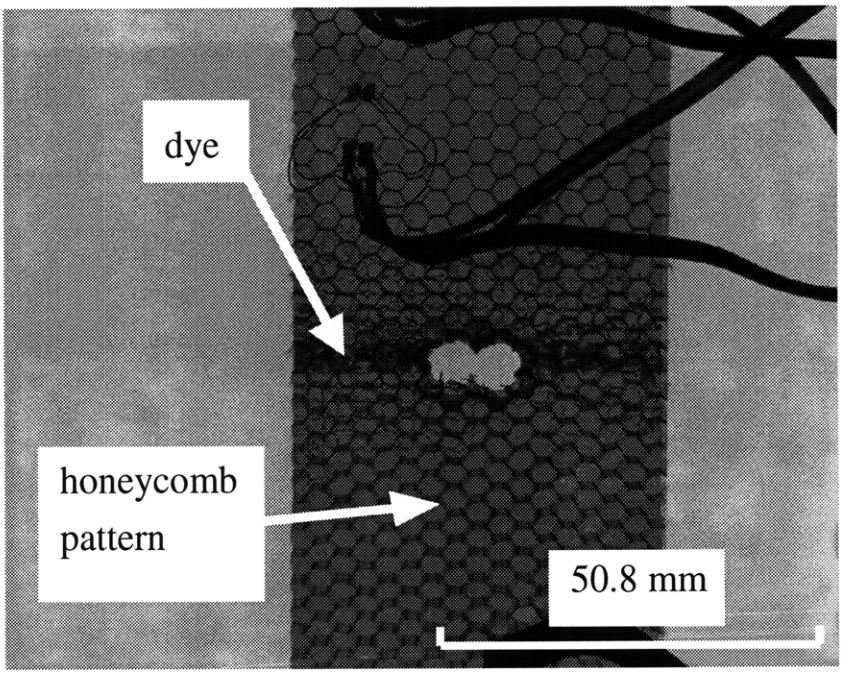

Figure 3.6. X-radiograph (top view).

This technique is very effective when working with composite laminates. However, the specimens involved in this study were sandwich panels, and the Nomex core complicated the process. First, the adhesive bond between the core and the facesheet, or the core itself, may have absorbed some of the dye. Second, the honeycomb pattern of the core showed up in the pictures. In any case, the lack of depth perception involved in X-radiography combined with the presence of the core made unambiguous damage detection very difficult with this method. Figure 3.6 depicts the lack of clarity shown in the X-radiographs taken.

3.6 Post-mortem Damage Characterization

3.6.1 Introduction

A critical aspect of this project was the characterization of the damage mechanisms in the notch tip region. There was no question regarding sub-critical damage occurring prior to catastrophic failure: it could be heard and in most cases seen macroscopically. However, this was not sufficient to pin-point the damage type(s) occurring at the microscopic level. In order to look at the damage mechanisms around the notch tip, destructive damage evaluation was a required.

3.6.2 Specimen Sectioning and Potting

Four sections were cut out of each specimen following catastrophic failure. The sections were labeled A, B, C and D and are depicted in Figure 3.7 below. Thus, section C from coupon AM3 will be referred to as AM3-C and so on. Surfaces suitable for microscopy were produced by grinding and polishing. A solid fixture in which to hold the material without breaking it while this is done is necessary. For this purpose, each section was placed in a transparent Epoxy solution and left to dry overnight. Sections were potted in different orientations to allow detailed characterization of the damage in several

directions. Figure 3.8 illustrates the two potting variations used to obtain "top" and "edge" views of the material.

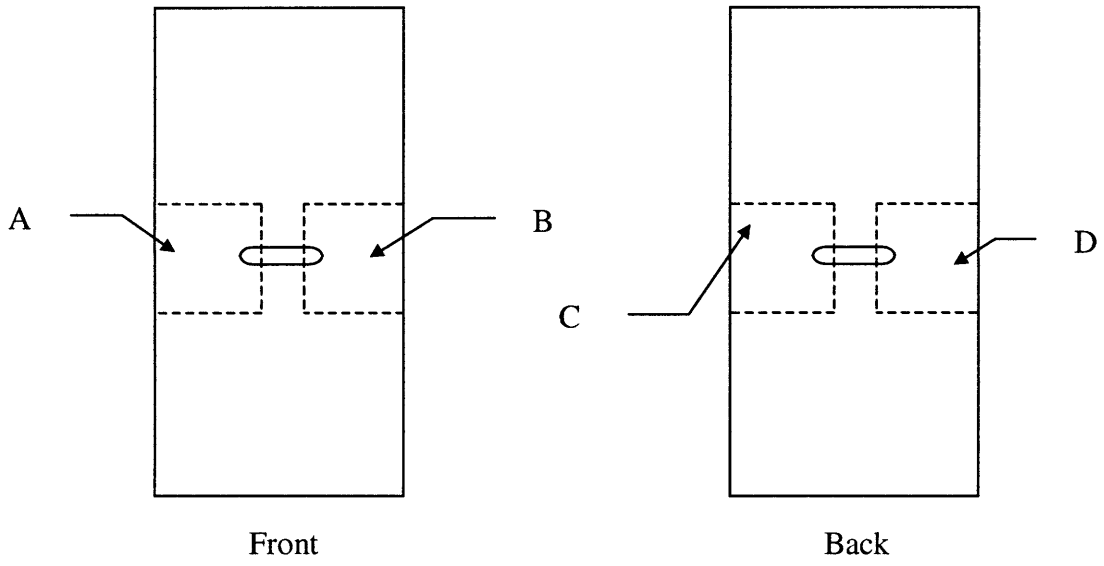

Figure 3.7. Specimen sectioning.

3.6.3 Polishing and Microscopy

The final step in the post-mortem damage evaluation was to view the inside of the material. This was achieved by polishing (or grinding) the potted material pressing it face-down against a rotating Silicon Carbide wheel. The directions in which the specimens were potted are illustrated in Figures 3.8a and 3.8b.

The sharp edges of each potted section had to be smoothed out with a coarse grit size wheel to avoid tearing of the finer wheels. Struers© wheels were employed, decreasing from 30μm (500 Struers code) grit size to start each section down to 5μm (4000 Struers code) grit size to lightly polish each section before taking a picture. All the grit sizes used are listed in Table 3.6.

Optical microscopes were used to monitor each section while it was being polished. Each section was repeatedly taken from the automated polishing machine to the microscope in order to see at every step if any sub-critical damage could be identified.

When a damage mechanism was identified, the potted section was taken to a more powerful microscope and a picture was taken.

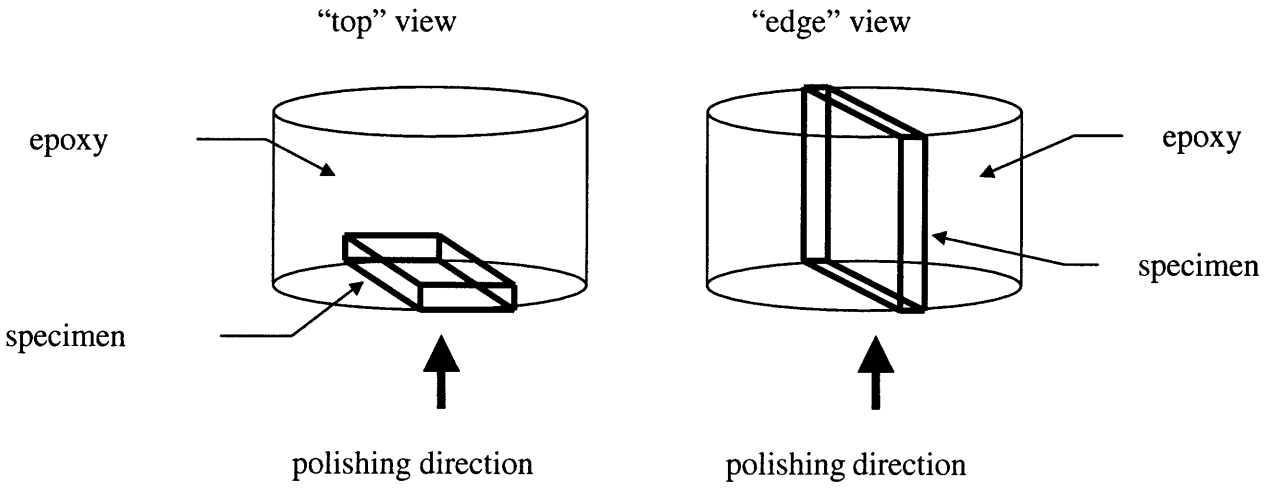

Figure 3.8. Section potting and polishing orientations.

Struers Code (grit)	Grit Size (μm)
500	30
800	22
1200	14
2400	8
4000	5

Table 3.6. Grit sizes and corresponding grit codes.

Chapter 4

Experimental Results

4.1 Compression Tests

4.1.1 Alignment

The validity of each test had to be determined before any of the data could be used for analysis. The parameter used throughout this work to determine whether a test was valid or not was the percentage difference between strain levels measured in the same position in the front and back facesheets, as defined in Equation 3.1. This provides a measure of the bending of the specimen. The alignment monitoring strain gauges measured axial strain, and were positioned as far away from the notch as possible, so as not to be located in a region of high strain gradients. Their location was chosen to be midway between the notch tip and the edge of the coupon along its width and height, and it is depicted in Figure 3.3a.

The standard for validity used for compression tests of sandwich specimens in the present work is a maximum of 5% difference (from Equation 3.1) between strains on the

front and back facesheets during initial loading. This was difficult to obtain because initial strain values were of the order of the differences in strain, which produced relatively large percentage differences. However, as the strain values increased, the differences between front and back strains remained almost constant, and hence the percentage differences dropped accordingly. This typical behavior is shown in Figure 4.1, yielding very small (and constant) values of strain percentage difference between the two sandwich panel facesheets after initial loading. Since the initial large percentage differences can be explained with the above argument, tests were concluded to be acceptable as far as alignment was concerned. Furthermore, since the bending strain levels off to a near-constant value it may be assumed that some of the apparent bending strain may be due to slight misalignment of the gauges and not the specimen itself.

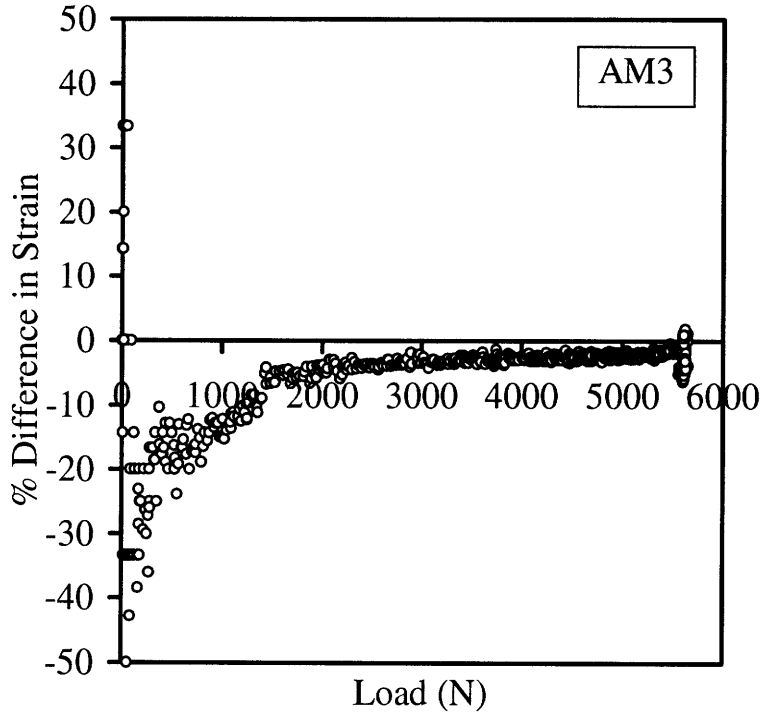

Figure 4.1: Typical front-to-back strain percentage difference as a function of load.

4.1.2 Sub-Critical Damage and Catastrophic Failure

As explained in Section 3.3.2, all tests were performed in displacement control mode and at very slow loading rates. For the most part, this approach succeeded in

controlling sub-critical damage when it did occur, although in some cases this damage would propagate in an uncontrolled manner at constant or even decreasing loads. This relatively "brittle" behavior was more frequently observed with the small coupons.

Perfect alignment and material uniformity would have produced symmetric damage; i.e. both facesheets would have exhibited the same damage type simultaneously. Furthermore, if the coupons had been flawlessly manufactured and perfectly machined, both sides of the notch would have shown the same damage as well. This ideal scenario would have produced four identical damage zones for each coupon, two on either side of the slit of each facesheet, which would have propagated at the same rate and failed catastrophically at the same load. However, in reality minor imperfections caused damage to occur preferentially at one location rather than the others. There was no systematic dependence as to which facesheet was more prone to fail either due to the difference in their surface roughness mentioned in Chapter 3 (smooth-front and rough-back) or their orientation in the load frame (front/back).

Sub-critical damage was typically observed emanating from one notch tip only, in the form of a linear damage zone (LDZ) or a delamination/bulge zone (DBZ) propagating perpendicular to the load direction. Once damage initiated it is presumed that the stress concentrations ahead of it would become higher than on any of the other notch tips and hence further damage propagation would concentrate on that flaw alone. Whenever sub-critical damage occurred, the applied load dropped since the tests were performed in displacement control, which tended to stabilize the growth of damage. Most coupons exhibited a toughening behavior, with damage only increasing in length with increasing applied load, until a critical damage length was reached. Damage would then propagate in an uncontrolled way and the facesheet would fail catastrophically. In a few cases damage growth was not stabilized, and damage propagated in an uncontrolled manner despite the decrease in load, causing catastrophic failure of the facesheet it was located in. In either case, catastrophic failure of a coupon was defined as the point at which damage was observed to propagate unstably from one of the notch tips to the edge of the laminate.

4.1.3 Facesheet Stiffness

All coupons exhibited elastic behavior prior to catastrophic failure, as is shown in Figure 4.2 which displays the linear relationship between applied stress and measured far-field strain for a medium-sized coupon. The difference between strain levels for the front and the back facesheets illustrates the strain mismatch discussed in Section 4.1.1. However, it must be noted that Figures 4.1 and 4.2 originate from the same data set, meaning that the strain level differences that seem so obvious in Figure 4.2 represent the very low (and acceptable) percentage differences in strain shown in Figure 4.1.

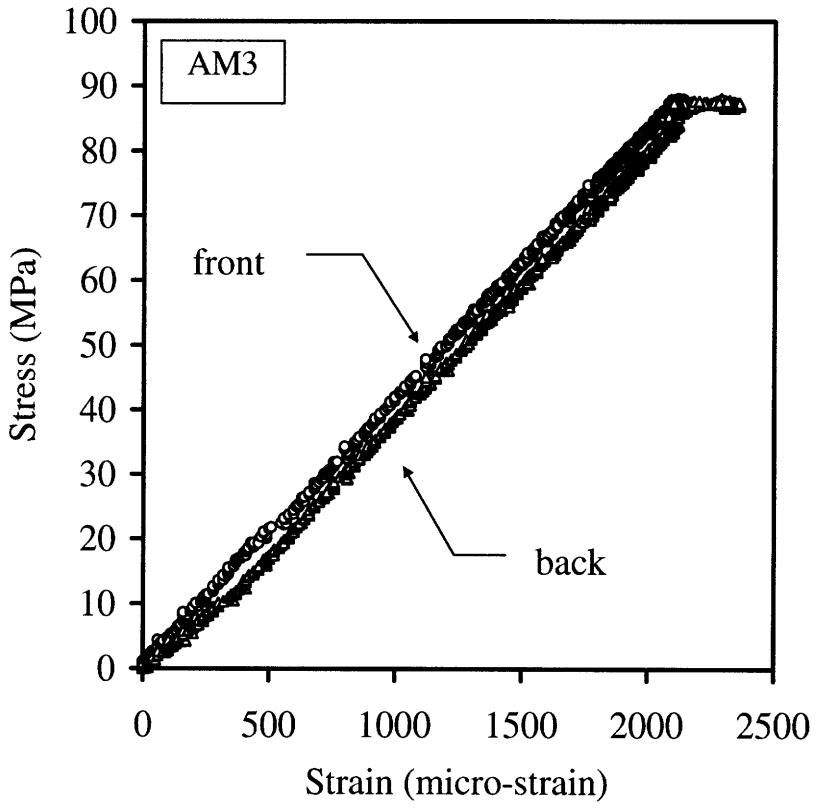

Figure 4.2: Typical stress-strain correlation.

Stiffness values were analytically determined using Classical Laminated Plate Theory (CLPT), and compared to the experimental values calculated from stress-strain plots such as the one depicted in Figure 4.2. The MATLAB™ CLPT code used is reproduced in Appendix 1, and the experimental values were obtained by computing the

gradient of the stress-strain plots for each coupon. Table 4.1 includes all experimental stiffnesses, and Table 4.2 compares the average value for each series (computed from Table 4.1) to the theoretical value (computed from the CLPT code).

	Stiffness (GPa)			Stiffness (GPa)	
T45 Series	**Front**	**Back**	**T0 Series**	**Front**	**Back**
AS1	36.3	33.6	**BS1**	43.2	45.9
AS2	37.0	35.4	**BS2**	47.0	44.1
AS3	37.2	32.3	**BS3**	42.1	47.3
AS4	39.4	41.1	**BM1**	58.5	56.3
AM1	38.7	43.0	**BM2**	44.3	42.4
AM2	42.4	49.2	**BM3**	51.9	49.1
AM3	41.3	40.0	**BM4**	48.8	50.0
AM4	41.1	39.0	**BM5**	58.9	99.2
AL1	37.6	40.8	**BL1**	52.8	71.0
AL2	39.8	39.4	**BL2**	48.7	66.1

Table 4.1: Experimental values for facesheet stiffness.

Test Series	Theoretical E_x (GPa)	Experimental E_x (GPa)	% Difference
T45	47.7	39.2	-17.8
T0	57.2	53.4	-6.7

Table 4.2: Theoretical and experimental facesheet stiffness values.

4.1.4 Ultimate Notched Strength

Catastrophic failure of a panel is defined in Section 4.1.2 above. Since load usually dropped after every increase in sub-critical damage, and because of the "brittle" behavior of the material system studied (uncontrolled damage propagation was sometimes observed with constant or even decreasing loads), catastrophic failure sometimes occurred at a load below the maximum load reached by a coupon. However, the ultimate failure load of each panel was defined as the maximum load reached by each

coupon. The ultimate failure loads for each sandwich panel (P_{fail}) and the ultimate failure stresses for the corresponding facesheets (σ_{fail}) are summarized in Table 4.3.

T45 Series	P_{fail} (kN)	σ_{fail} (MPa)	T0 Series	P_{fail} (kN)	σ_{fail} (MPa)
AS1	6.6	103	**BS1**	8.7	135
AS2	6.7	105	**BS2**	10.5	163
AS3	7.1	110	**BS3**	9.2	143
AS4	6.6	103	**BM1**	15.9	124
AM1	11.5	89.8	**BM2**	16.2	126
AM2	10.4	80.6	**BM3**	13.4	104
AM3	11.3	88.1	**BM4**	16.9	131
AM4	12.0	93.0	**BM5**	16.0	124
AL1	18.9	73.7	**BL1**	21.4	83.3
AL2	18.1	70.4	**BL2**	23.6	91.7

Table 4.3: Failure loads and stresses for all coupons tested.

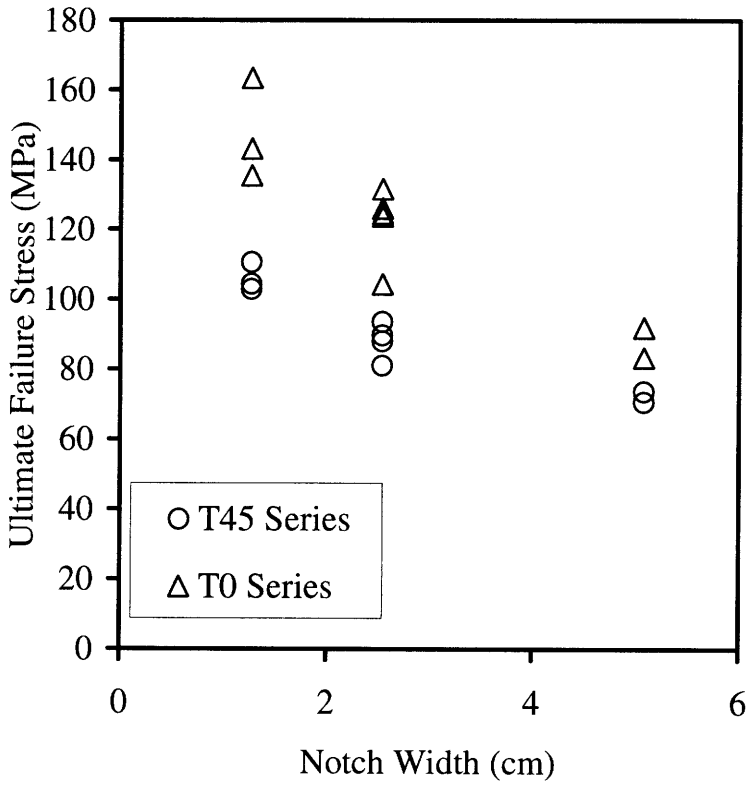

Figure 4.3: Notch size effect on laminate ultimate failure stress.

Ultimate facesheet failure stress decreased with increasing notch size, a common observation made by other researchers (as discussed in Chapter 2). Figure 4.3 depicts the trend observed with the two material systems studied in this work. This is further discussed in Chapters 5 and 6.

4.2 Damage Propagation

4.2.1 Overview

Compression tests confirmed that different lay-ups behave distinctly at the macroscopic as well as the microscopic level. It was also observed that coupon size plays an important role in determining the stability of sub-critical damage. The various damage observation techniques employed on each coupon revealed the different mechanisms responsible for catastrophic failure in the two lay-ups studied.

4.2.2 In-situ Audible Damage Observations

The most common form of sub-critical damage detected were audible "popping" sounds during loading. This behavior was observed on both series (T45 and T0) equally. Typical tests would involve anywhere between one and five distinct "pops" prior to catastrophic failure, sometimes more. Every time a "pop" was heard, the data file containing load and strain measurements was marked; subsequent analysis showed that the "pops" always corresponded to a load drop. This observation leads to the conclusion that stable damage was occurring under the surface of the composite facesheets during loading. It is presumed that every time a new "pop" was heard it meant that either a new damaged area had been created, or an existing one had grown.

4.2.3 In-situ Visual Damage Observations

The T45 series generally exhibited a less "brittle" behavior. Sub-critical damage was more easily controlled with this material system, even with the small coupons that exhibited the least stable damage growth. However, sub-critical damage was successfully controlled and visually observed with both the T45 and the T0 series, and is discussed in detail in the following pages.

Observing damage with the naked eye was not straight-forward due to the lack of contrast afforded by the material. The black, shiny surface of the coupon facesheets made it difficult to spot any of the anticipated cracks, splinters, crush zones or humps. However, the application of a thin "white-out" coat spanning the notch height from the notch tip to the edge of the coupon (as described in Section 3.4.1) simplified damage detection considerably. If damage appeared on the surface of either of the facesheets, it was obvious due to the brittle "white-out" coat cracking. Such cracks enabled accurate measurements of damage lengths on the surface of the laminates.

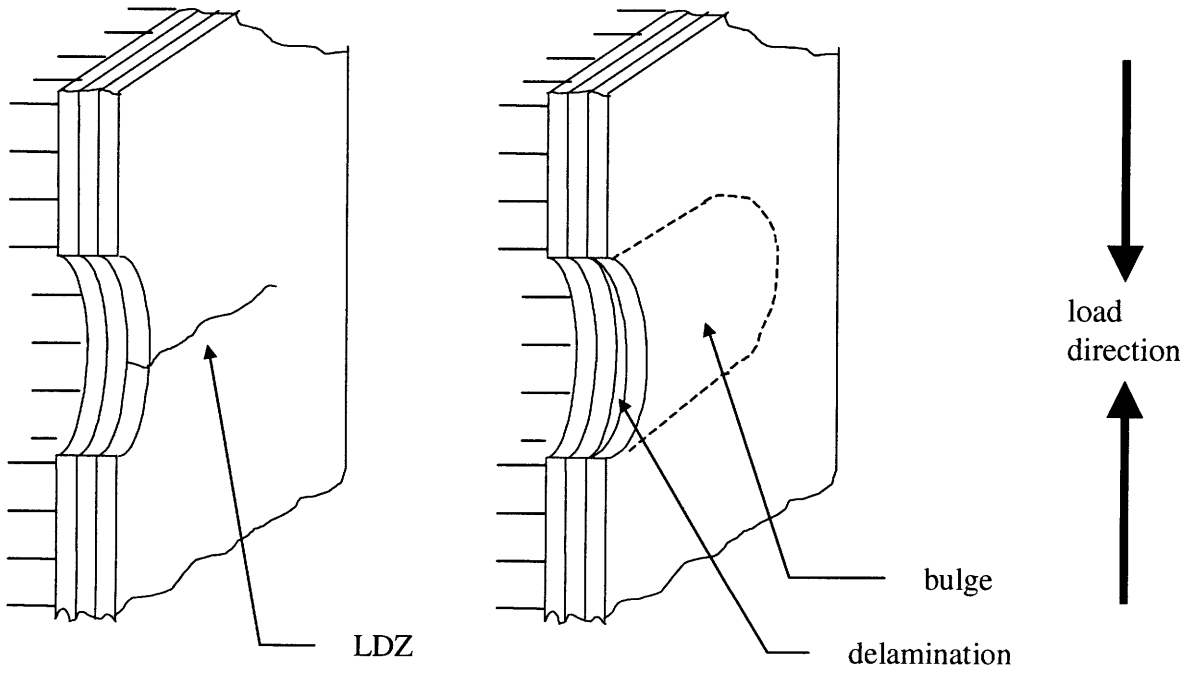

Figure 4.4: Observed macroscopic damage types: (a) LDZ; (b) DBZ.

Visual damage took one of two forms: a crack-like linear damage zone (LDZ) or a bulging of the exterior ply coupled with interior delamination, or delamination/bulge zone (DBZ). LDZ's and DBZ's emanated from one (or more) of the facesheet notch tips and propagated perpendicular to the load direction. Figure 4.4 shows an edge view depiction of these two damage types. The cartoon shows one of the sandwich panel facesheets, with the honeycomb core being to the left of the facesheet.

LDZ's differ substantially from the cracks typically seen in tension tests. They consist of a load-bearing "crush zone" that arises due to the applied compressive load. This is explained in more detail in Section 4.2.4. Such LDZ's could only be identified *in-situ* if they were present in the outer-most ply of either facesheet, so if they were present in the inside layers it was impossible to detect them with the naked eye. LDZ's were sometimes confined to one ply (as depicted in Figure 4.4a), and in other cases they would run through two or three of the facesheet plies.

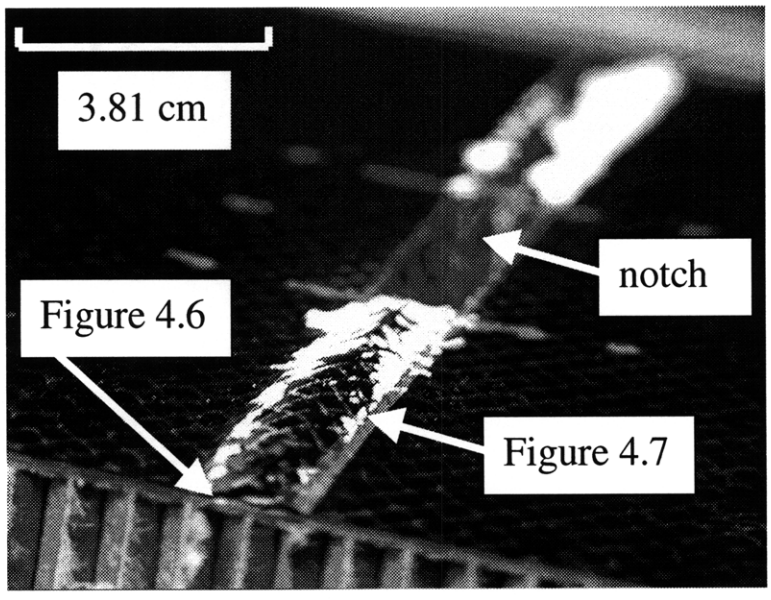

Figure 4.5: Oblique view of DBZ (AM4).

DBZ's were less frequent, but they were generally (and consistently) observed when sub-critical damage growth was more stable. The term describes an out-of-plane deflection of one (as seen in Figures 4.5 through 4.7), two or three plies spanning the diameter of the notch and propagating away from the notch tip perpendicular to the load direction (refer to Figures 4.5 through 4.8). The instability appeared as an elongated blistering of the outer ply. As depicted in Figure 4.4b, bulges were always accompanied by a delamination at one of the ply interfaces which enabled the out-of-plane bending phenomenon. It was also observed that these bulges were elastic in nature, since the facesheets returned to their original (flat) configuration upon load removal in most cases. Therefore, a five-minute epoxy layer was applied on one of the bulges to make a cross-sectional study possible (see Figure 4.7). Figure 4.6 shows the edge of the coupon at the location of a fractured DBZ, and Figure 4.7 depicts an interior (polished) cross-section of an intact DBZ.

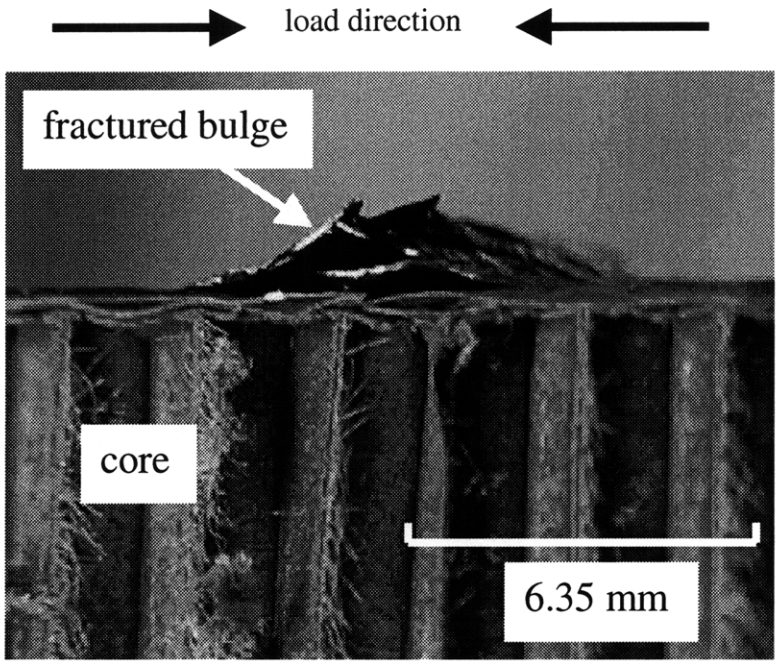

Figure 4.6: Edge cross-section of DBZ (AM4).

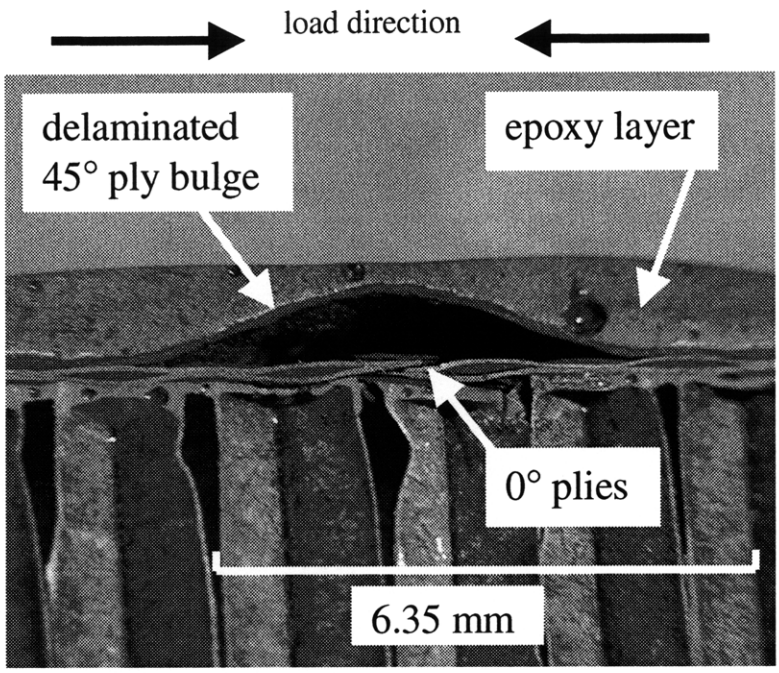

Figure 4.7: Interior cross-section of DBZ (AM4).

Sub-critical damage generally manifested itself as either an LDZ or a DBZ, but not both (they were observed concurrently only in one coupon: an LDZ was seen to originate from the tip of a bulge). LDZ's were observed on both material systems, whereas DBZ's were exclusive to the less brittle T45 series, clearly suggesting that material system (and more specifically lay-up) plays an important role in determining the compressive failure mode.

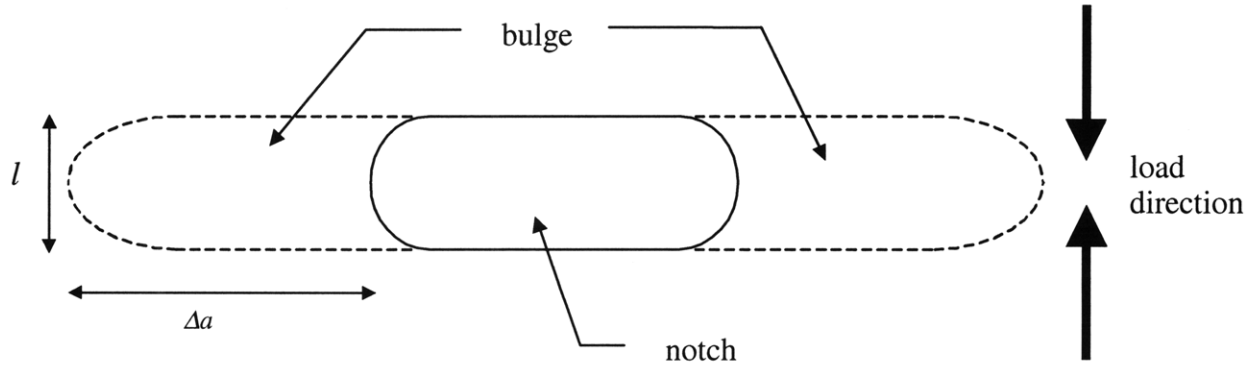

Figure 4.8: DBZ geometry (front view).

Both LDZ's and DBZ's propagated in a discontinuous manner, consisting of a series of rapid growth and arrest events. These increments in damage growth usually ended where a weave tow ended. This observation strongly suggests that the tow spacing in the ply weave has a strong effect on damage growth mechanics. Damage was never observed to grow, in a controlled manner, beyond half the distance from the notch tip to the edge of the coupon.

4.2.4 Post-mortem Damage Observations

Unmagnified visual observations of damage are useful since they provide an overview of the nature of the problem. However, they provide no information as to the damage occurring beneath the surface of the material, which is usually present in laminated materials such as those studied here.

Compressive tests complicate *post-mortem* damage evaluation of laminated materials because, upon crushing during final failure, the plies tend to overlap and the crush zone becomes a mesh of fiber ligaments and splinters running into each other. It is usually difficult to determine conclusively which microscopic failure mechanisms were present prior to, and which were the result of, crushing upon catastrophic failure (Figure 4.9).

For this reason, the relevant specimens for *post-mortem* inspection were those that did not fail catastrophically. It was here that the sandwich configuration presented an advantage. Since most of the coupons exhibited catastrophic failure in one of the facesheets only, it was possible to section and inspect the surviving facesheet using the procedures described in Sections 3.6.2 and 3.6.3. The polishing directions depicted in Figure 3.8a and 3.8b will be called "top" and "edge" respectively for simplicity.

Top and edge views of polished specimen sections revealed a series of failure mechanisms, including matrix and fiber breaks, delamination, LDZ and fiber micro-buckling. Figures 4.10 through 4.18 depict these mechanisms . The capital letter

following the specimen number refers to the section photographed (see Figure 3.7). Load direction in Figures 4.9 through 4.19 is vertical.

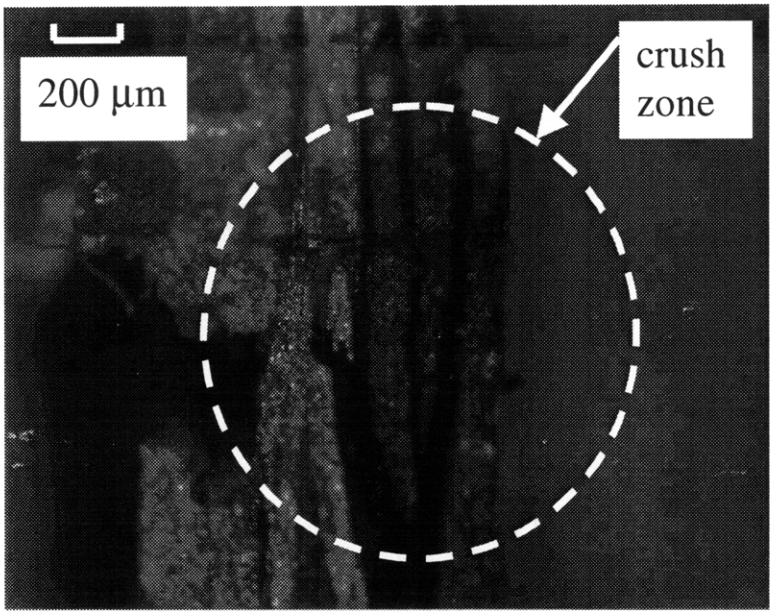

Figure 4.9: Crush zone following catastrophic failure (AM3-C, edge view).

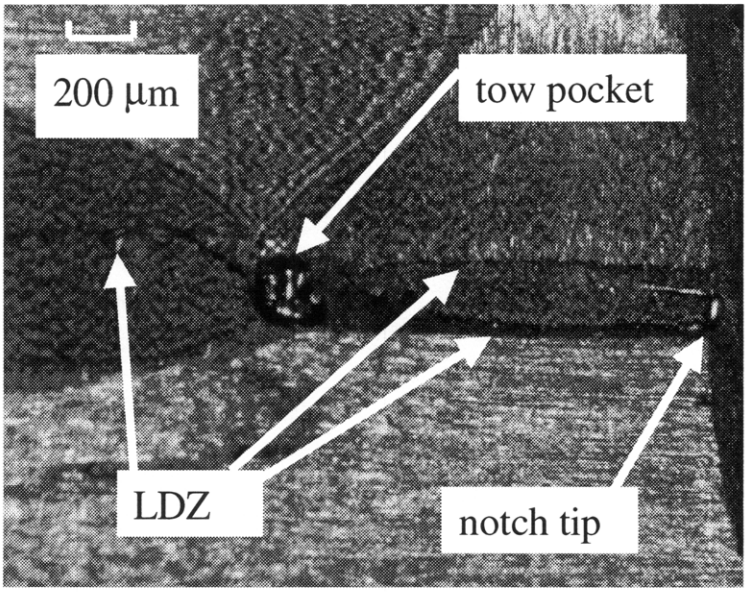

Figure 4.10: LDZ origin at the notch tip (AM3-B, top view).

Microscopic damage was observed mostly in the plies parallel to the load direction (0° plies). The LDZ reproduced in Figures 4.10 to 4.12 was observed in the middle 0° ply of a T45 series coupon only after completely removing (by grinding) the top 45° ply. Figure 4.10 shows the start of the damage, emanating from the notch tip and growing towards the left. The damage initiated as two separate LDZ's, running parallel to each other and meeting at a tow pocket (a void that arises during manufacture due to the composite woven architecture). From that point on the damage continued to propagate as a single LDZ with the 0° fibers kinking and fracturing.

LDZ propagation is depicted in Figure 4.11 which shows another view of the LDZ running through individual tows and not along the boundaries created by the weave. The behavior of this damage type was quite consistent, running from one tow pocket to another cutting through 0° fibers.

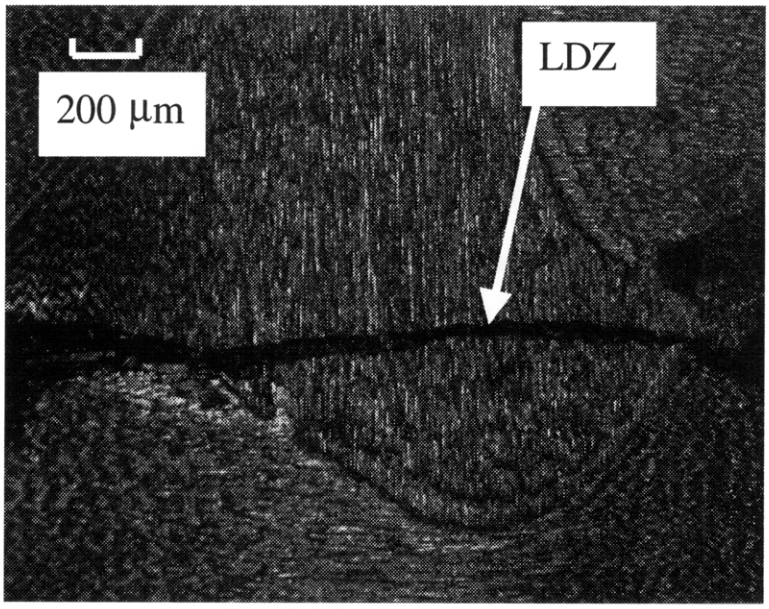

Figure 4.11: LDZ path (AM3-B, top view).

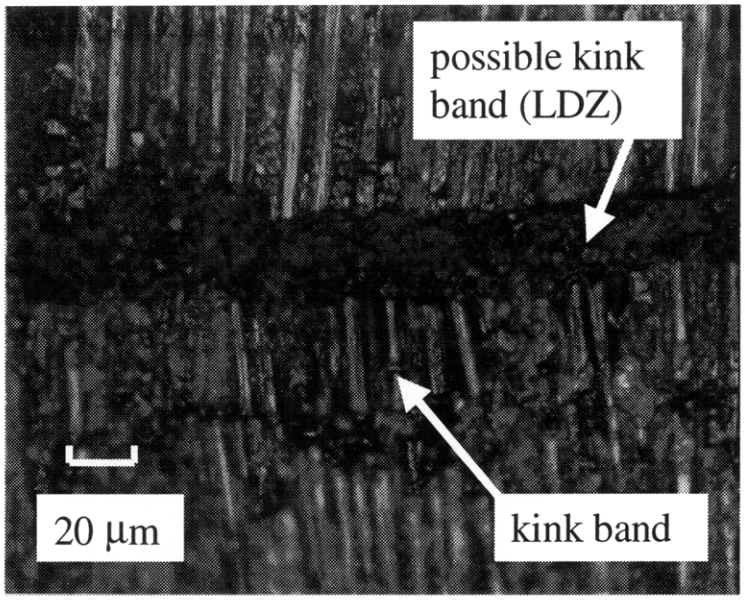

Figure 4.12: Possible fiber micro-buckling in an LDZ (AM3-A, top view).

Closer inspection gave better insight as to the damage mechanisms comprising this LDZ. Figure 4.12 reproduces a higher magnification image of the same damage type. The LDZ has been filled with the potting epoxy, and the picture clearly reveals a constant spacing between the broken fiber ends. Due to the compressive nature of the loading, it is impossible that the spacing occurred by fibers breaking in tension and separating.

Fiber micro-buckling is a typical failure mechanism for composites loaded in compression. The gap seen between the fibers in Figure 4.12 might be a kink band whose micro-buckled fiber ligaments have either fallen off when the damage occurred, or been removed in the polishing process. The same conclusion can be drawn from Figures 4.13 and 4.14, edge views which reveal fiber breaks in the inner 0° plies.

Edge polishing provided another view of the damage, and enabled damage modes running along the ply interfaces to be detected. Extensive delamination was observed surrounding fiber damage (Figures 4.13 through 4.16). The consistent presence of delamination suggests that it might be one of the driving mechanisms for final failure.

Furthermore, it can be inferred that delamination removes some lateral constraint which allows other forms of damage to occur.

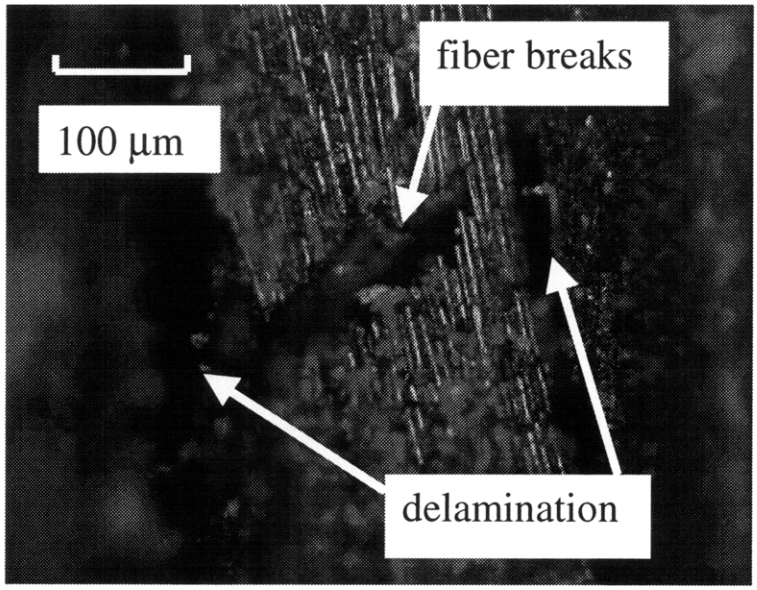

Figure 4.13: Fiber breaks and delamination (AM3-A, edge view).

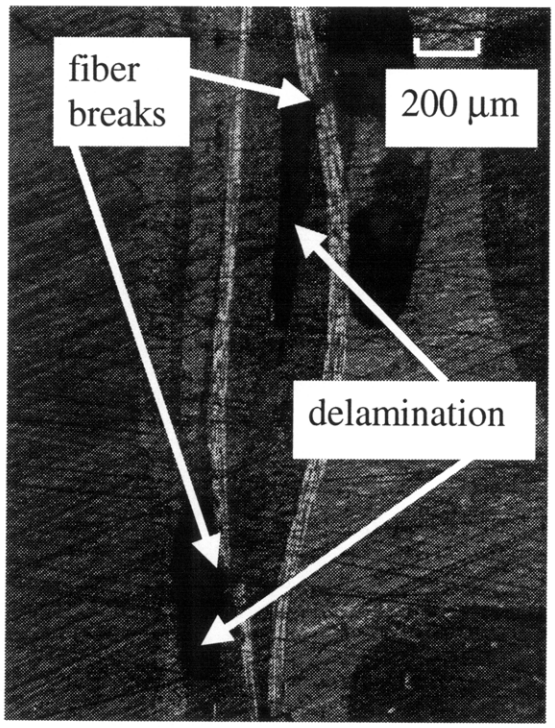

Figure 4.14: Fiber breaks surrounded by delamination (AL1-B, edge view).

Although not observed in all specimens, fiber micro-buckling was a common failure mode, which was most easily seen in edge-polished sections. Figure 4.15 shows this failure type in which all the fibers in the middle (0°) ply have buckled and formed a kink band. The extensive delamination surrounding the kink band is also observed.

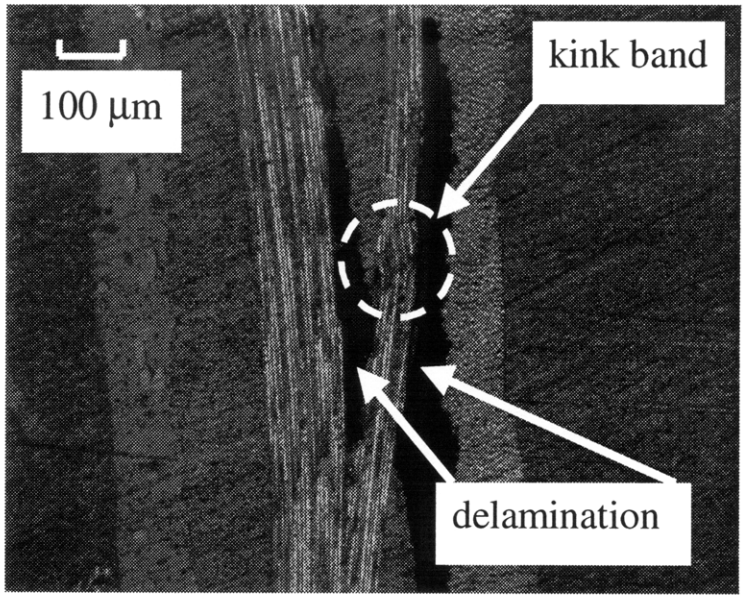

Figure 4.15: Fiber micro-buckling surrounded by delamination (AM2-B, edge view).

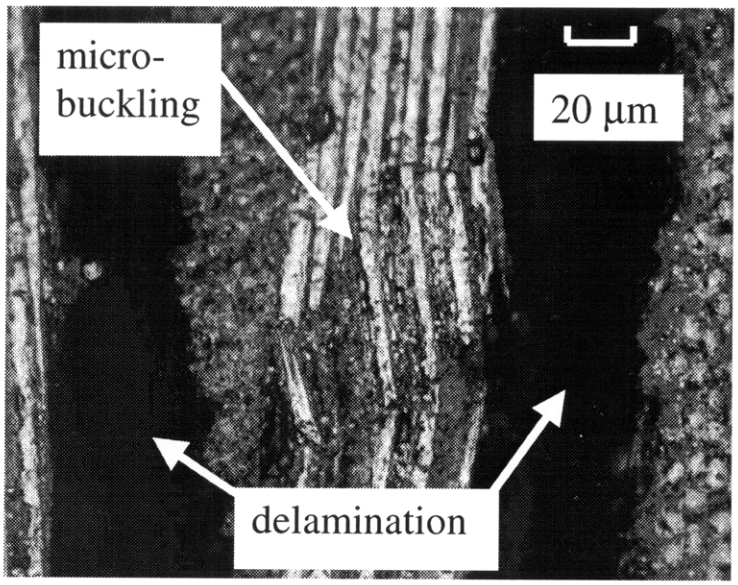

Figure 4.16: Fiber micro-buckling magnified (AM2-B, edge view).

Figure 4.16 represents the same damage depicted in Figure 4.15 only at a higher magnification. The geometry of the kink band is easily observed. Since buckled structures carry their buckling load, this failure mode could very well explain the load transfer observed through the damage which is discussed in detail in Section 4.3.

Kink band formation is sometimes described as "shear crimping". This occurs by the fibers failing in shear at two points, forming a band which contains fiber ligaments at an angle to the original fiber direction. This is seen in Figures 4.15 and 4.16, and again in Figure 4.17. In this last figure, the overall shear displacement of all the fibers in the ply is more pronounced, and the resulting misalignment between the two ply sections which have become separated by the kink band is prominent.

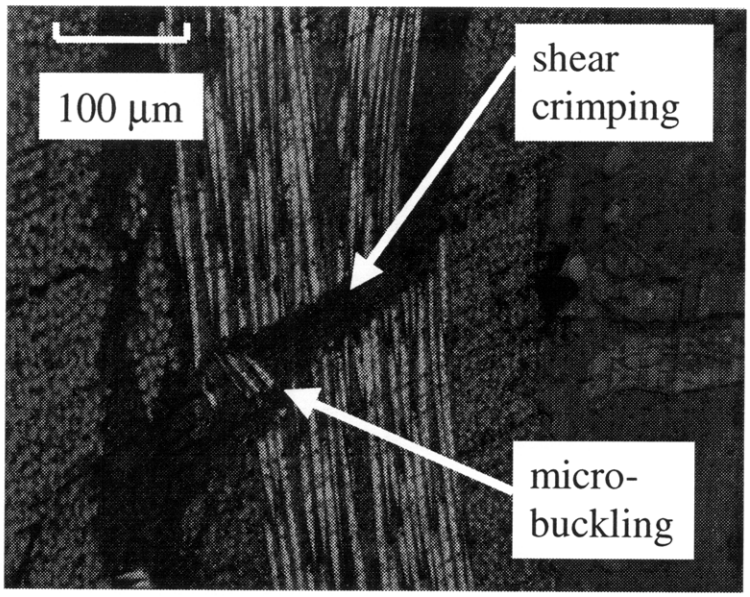

Figure 4.17: Shear crimping (AL1-B, edge view).

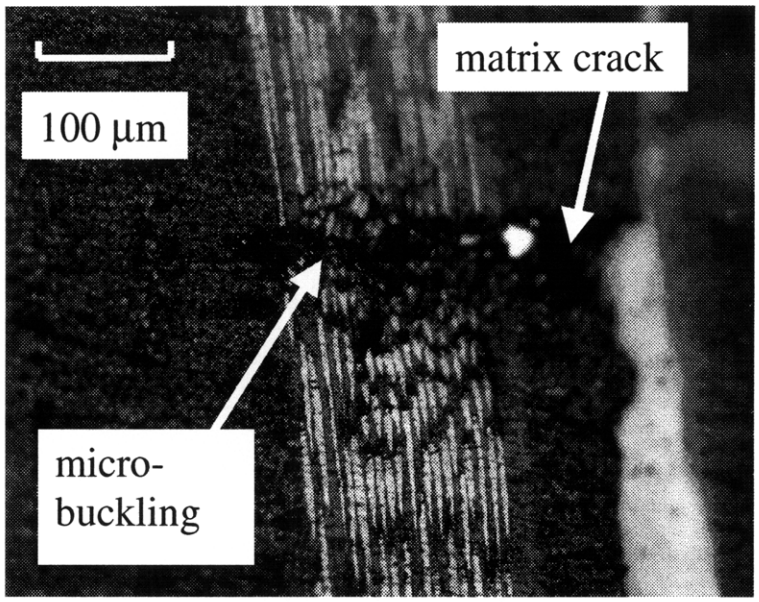

Figure 4.18: Matrix cracking and fiber micro-buckling (BM1-D, edge view).

Figure 4.18 shows an interesting form of fiber break/micro-buckle. This T0 series coupon reveals extensive matrix cracking adjacent to the kink band. The sequence of events cannot be determined definitively from this micrograph; however, it appears as though the 90° weave of the outer ply has crushed and the resulting ligaments have disappeared either upon load removal or during the potting/polishing process, which removed enough lateral constraint for the fibers in the 0° direction to fail (out-of-plane) in a shear mode. Hence the formation of the kink band of which remnants are obvious towards the left of the ply.

4.2.5 Similarities and Contrasts

The first signs of sub-critical damage were small "popping" sounds which probably involved individual fiber breaks or instabilities. The applied load was observed to decrease systematically with every "pop", confirming that indeed the noises heard were some form of damage possibly occurring below the material surface, which prevented its visual detection. This form of damage was detected in both T45 and T0 material systems.

Coupon "brittleness" proved to be very dependent not only on coupon size, but also on facesheet material lay-up. Small coupons exhibited a more "brittle" behavior, with catastrophic failure occurring almost instantaneously with practically no sub-critical damage. Of the two material systems investigated, the T0 series behaved in a more "brittle" manner, with stable damage growth only observed with medium and large sized coupons, whereas damage growth was stable in the T45 series at all coupon sizes. The large coupon geometries provided the best environment for studying sub-critical damage propagation since damage growth was very stable for both material systems.

Whenever sub-critical damage occurred, the applied load dropped accordingly. In order for the damage to grow, or new damage to be created, the applied load had to exceed the load that had caused the previous damage (except for the very brittle coupons which failed catastrophically even under decreasing loads with little or no sub-critical damage). This toughening of the material was observed in both series.

Macroscopic failure modes were very different for the two lay-ups investigated. Whereas LDZ's were observed on both material systems, DBZ's were exclusive to T45 series coupons. This suggests that the outermost 45° ply in the T45 series plays an important role in allowing this bulge to develop, or perhaps the outermost 0° ply in the T0 series is too stiff for the out-of-plane deflection to occur. Bulges always had the same width, which was dictated by the notch diameter, l (see Figure 4.8).

Careful evaluation of the micrographs led to the conclusion that fiber micro-buckling surrounded by extensive delamination is the most common form of microscopic sub-critical damage. The fact that delamination was observed in the absence of fiber micro-buckling (Figure 4.19), but not *vice-versa*, suggests that delamination might be the first failure mechanism to occur, and that it acts as a precursor to fiber micro-buckling by removing the lateral constraint on the 0° plies.

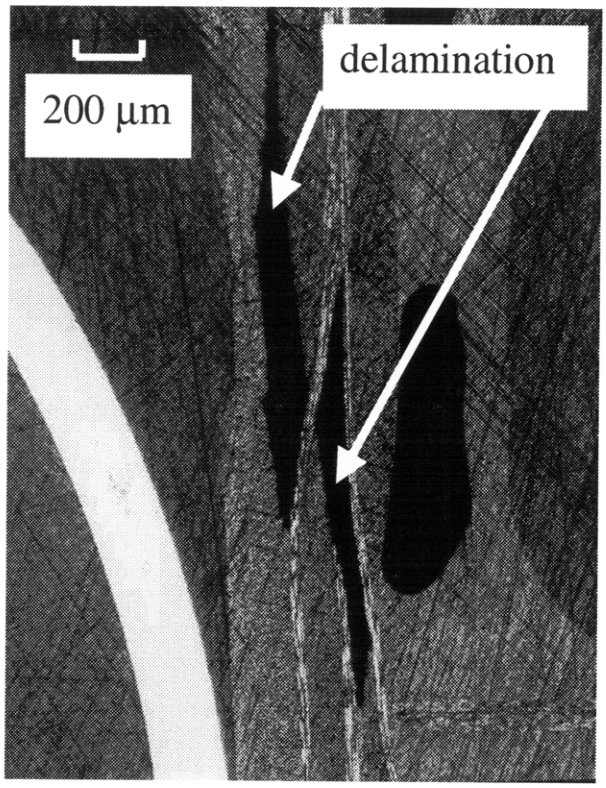

Figure 4.19: Delamination at both ply interfaces (AL1-B, edge view).

4.3 Cohesive Zone Measurements

4.3.1 Load vs. Strain Plots

As described in Section 3.4.3, strain gauges were placed along the anticipated LDZ path for two large coupons (AL2 and BL2) since they exhibited controlled sub-critical damage. Similar trends were observed for both material systems.

Figure 4.20 shows strain variation with applied (facesheet) load for gauges 1 through 5 for test coupon AL2. Gauges 1 and 2 are the alignment monitoring gauges (1 = front and 2 = back). Gauges 3, 4 and 5 are the cohesive zone strain measuring gauges, placed 3.5mm, 9mm and 14.5mm respectively away from the notch tip on the back facesheet.

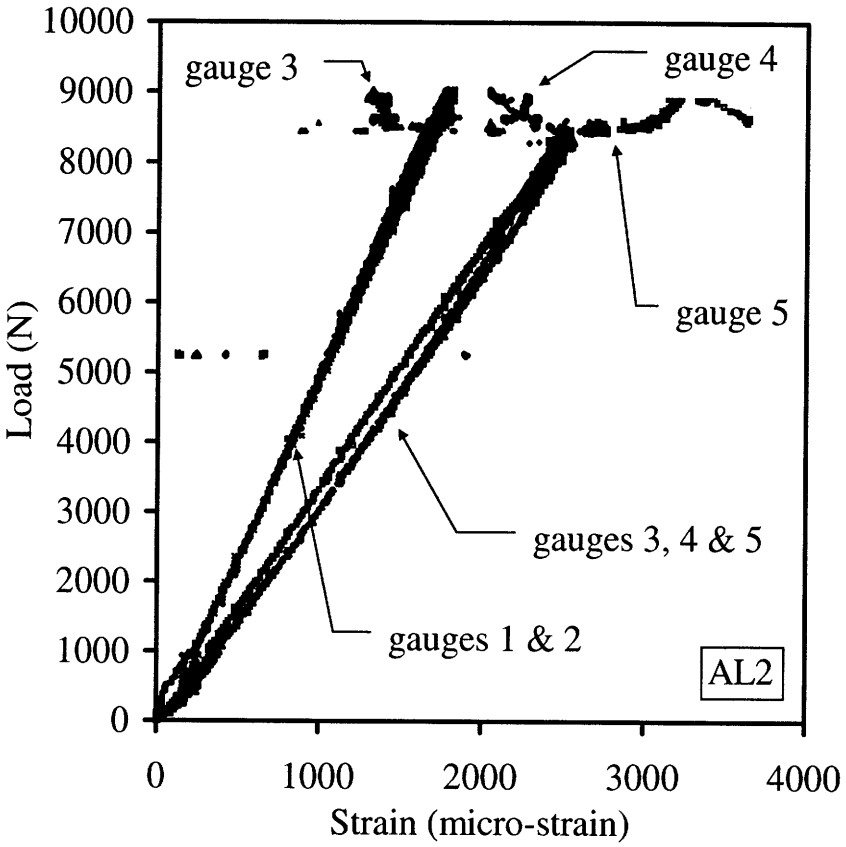

Figure 4.20: Variation of local strain with applied load (AL2).

The stress-strain plot above reveals several points; first, good alignment was achieved, as confirmed by the good correlation between strain readings for gauges 1 and 2. The stress concentration expected due to the presence of a notch is confirmed by the higher strain readings for gauges 3, 4 and 5 compared to the far-field gauges 1 and 2. Careful observation also reveals that gauge 3 is the first of the cohesive zone gauges (3, 4 and 5) to experience a drop in strain level, followed by gauge 4 and eventually gauge 5. This sequence of events is better seen in Figure 4.21 and is explained in detail in Section 4.3.2. The above plot is useful in confirming that the test was performed under acceptable alignment and that the material behaved in an elastic manner prior to the initiation of damage. Specimen BL2 behaved in a similar manner, with different stress and strain levels due to the difference in lay-up.

4.3.2 Local Strain Response

The progression of strain in the damage zone with increasing applied displacement is presented for the two coupons. Figure 4.21 depicts the behavior for coupon AL2 and Figure 4.22 represents coupon BL2. Both plots have been truncated to display more clearly the strain variation as the cohesive zone passes the monitoring gauges (3-5).

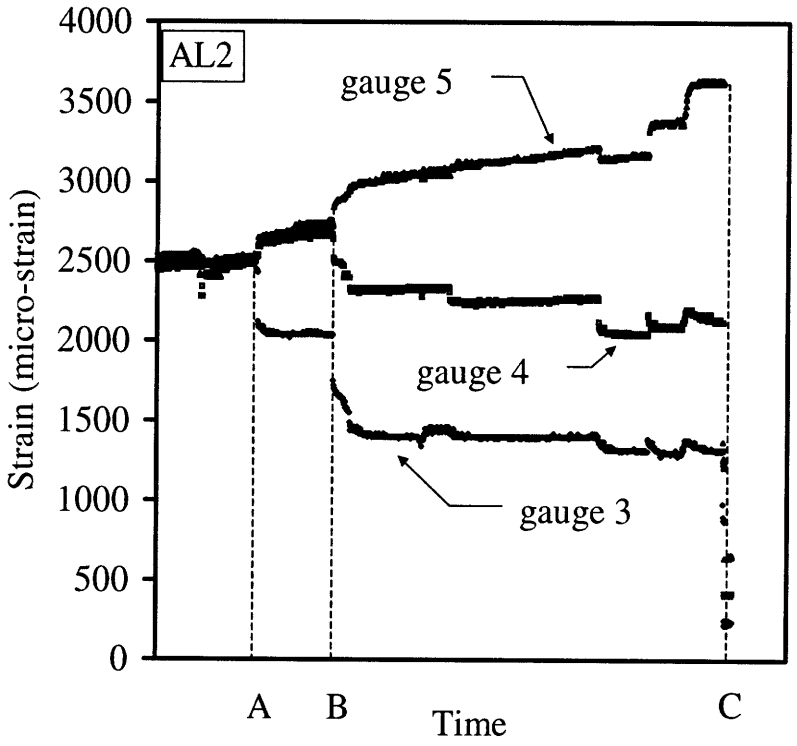

Figure 4.21: Strain progression in the cohesive zone (AL2).

For coupon AL2, gauge 3 was located slightly ahead of the observed LDZ in the first part of the test. The three gauges had similar strain levels up to this point, with the reading from gauge 3 being slightly higher than those of gauges 4 and 5, and that of gauge 4 being higher than that of gauge 5 (which is due to the stress concentration introduced by the LDZ adjacent to gauge 3 which decreases as distance from the LDZ tip

increases). At point A, the strain level of gauge 3 drops suddenly, and those of gauges 4 and 5 rise. At point B, the strain level of gauge 3 drops again, as does that for gauge 4 while gauge 5 experiences another rise in strain. Final failure is reached at C, at which point the strain goes to zero for all gauges.

From these observations, it can be inferred that point A corresponds to the damage growing past gauge 3, causing the strain measured by it to drop, but not completely, due to the residual load-bearing capability of the crush zone, as was discussed earlier. This would also explain the increase in the strain measured by gauges 4 and 5, since they are now affected by the stress concentration caused by the LDZ tip. Similarly, point B can be presumed to represent the damage propagating past gauge 4, causing the strain levels measured by gauges 3 and 4 to drop to a non-zero value and that measured by gauge 5 to rise further. Finally, point C could represent the damage growing past gauge 5 and propagating to the edge of the coupon causing final failure, since all strains measured go to zero.

Coupon BL2 exhibited a slightly different behavior. Gauge 3 for this specimen was located directly above the observed LDZ, so that it would already be in its wake and a shorter LDZ growth would still be able to display strain behavior in the cohesive zone fully (since sub-critical damage was expected to be less controllable for this lay-up than for coupon AL2). Figure 4.22 starts showing the strain level for gauge 3 below that of gauge 4, since it is in the wake of the LDZ already. The strain level at gauge 5 is still below that of gauge 3, however, so the ability of the crush zone to carry load is confirmed once again.

At point A, the strain level at gauge 3 drops significantly, while those of gauges 4 and 5 rise slightly. Strain measured by gauge 3 drops below that of gauge 5. The fact that the strain level for gauge 4 goes up reveals that the LDZ has not propagated past it yet. In fact, it is approaching the location of gauge 4 since the stress concentration introduced by the LDZ tip is becoming more acute causing the strain levels of gauges 4 and 5 to rise. The strain level for gauge 3 dropping further confirms that the LDZ has propagated away

from it, and now the traction carried by the cohesive zone at the location of gauge 3 has decreased, which is consistent with observations for coupon AL2. Point B signals final failure since all the strain levels go to zero. Since this coupon failed in a more "brittle" manner, the LDZ behavior observed for coupon AL2 was not reproduced.

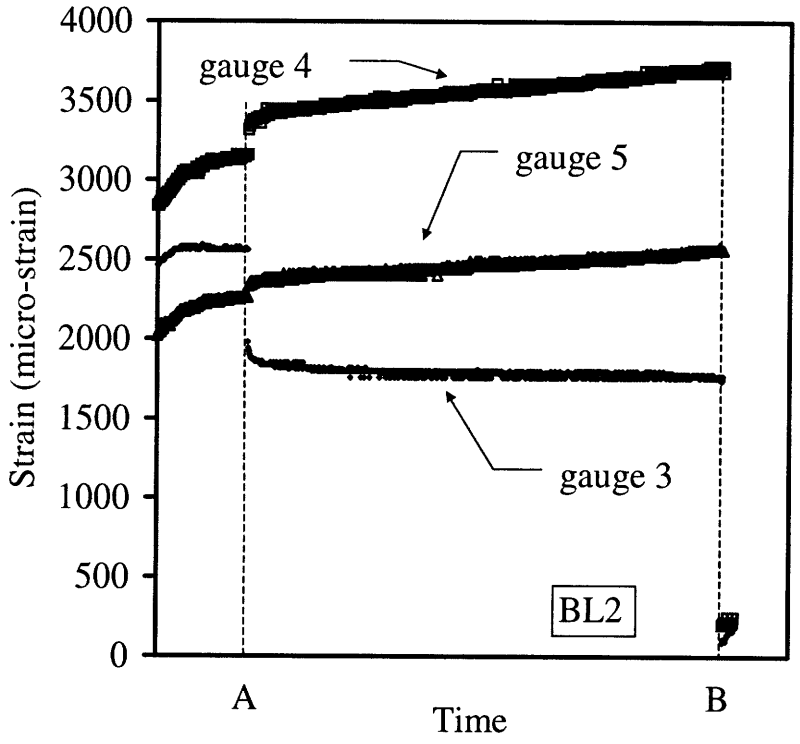

Figure 4.22: Strain progression in the cohesive zone (BL2).

4.3.3 Load vs. Crack Length Plots

Although the actual LDZ was not visually detected in coupon AL2 for the whole duration of the test, the above argument is strong enough to allow an LDZ length (which could very well run in one of the inner 0° plies) to be inferred from the strain data. There is an irrefutable initial LDZ length of 1.5mm which was visually detected before placing the cohesive zone strain gauges. Subsequent LDZ lengths are therefore equated to the

location of the cohesive zone strain gauges and correlated with the applied load that causes the respective strain drops in these gauges.

Thus, the LDZ length that causes the first drop (point A in Figure 4.21) is 3.5mm, the LDZ length corresponding to point B is 9mm and that of point C is 14.5mm. These LDZ lengths are correlated to the respective applied loads at points A, B and C to produce Figure 4.23, which is a simple form of a resistance curve which shows that a slightly increased applied load is required to obtain an increase in damage length.

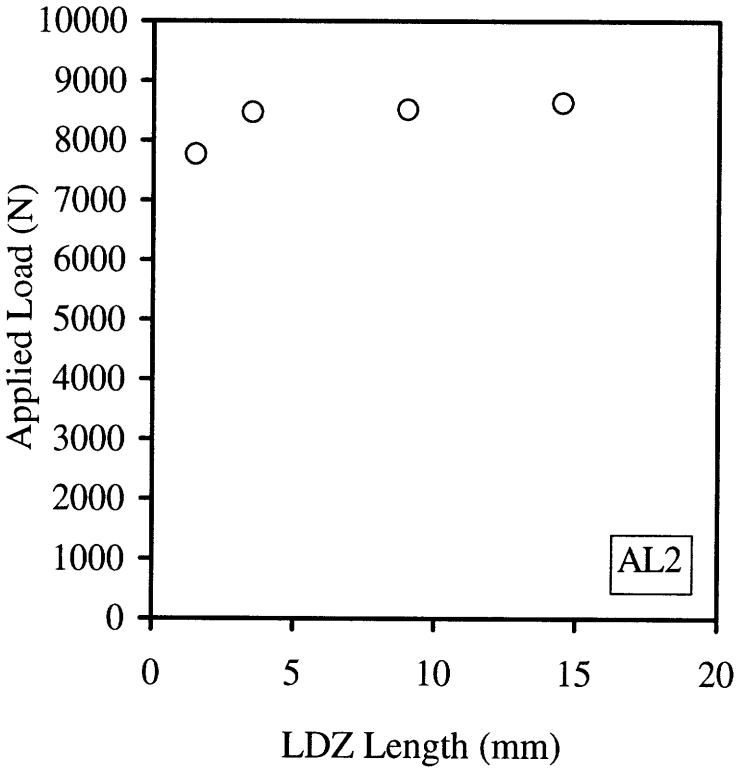

Figure 4.23: Applied load vs. linear damage length (AL2).

It is acknowledged that these LDZ lengths may very well not be the actual LDZ lengths for the test. The fact that the LDZ propagates past a gauge does not mean that it stops precisely at that gauge location. Therefore, the LDZ length once the strain levels reveal that it has gone past gauge 3 could be anywhere between gauge 3 and gauge 4.

Similarly, the LDZ length after it has traversed gauge 4 could be anywhere between it and gauge 5.

More direct resistance curves can be produced from data from specimens AL1, BM4, BM5 and BL1, for which sub-critical damage was visually observed to grow in a controlled manner throughout the entire tests. Panels AL1 and BM5 experienced extensive sub-critical damage, emanating from two notch tips simultaneously. Panels BM4 and BL1 exhibited controlled damage emanating from one notch tip only. The correlations between applied load and measured crack lengths for these coupons are depicted in Figures 4.24 through 4.27.

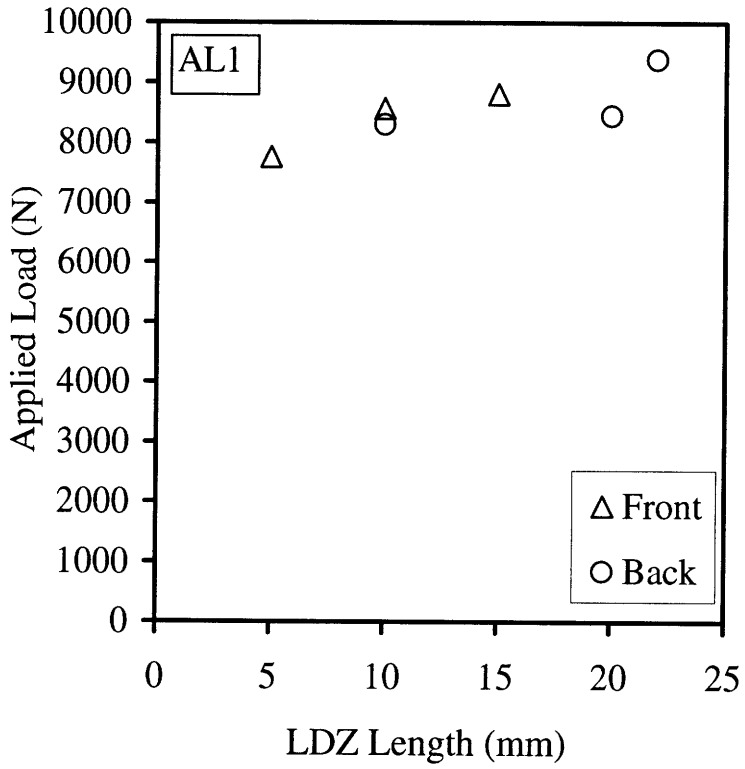

Figure 4.24: Applied load vs. linear damage length (AL1).

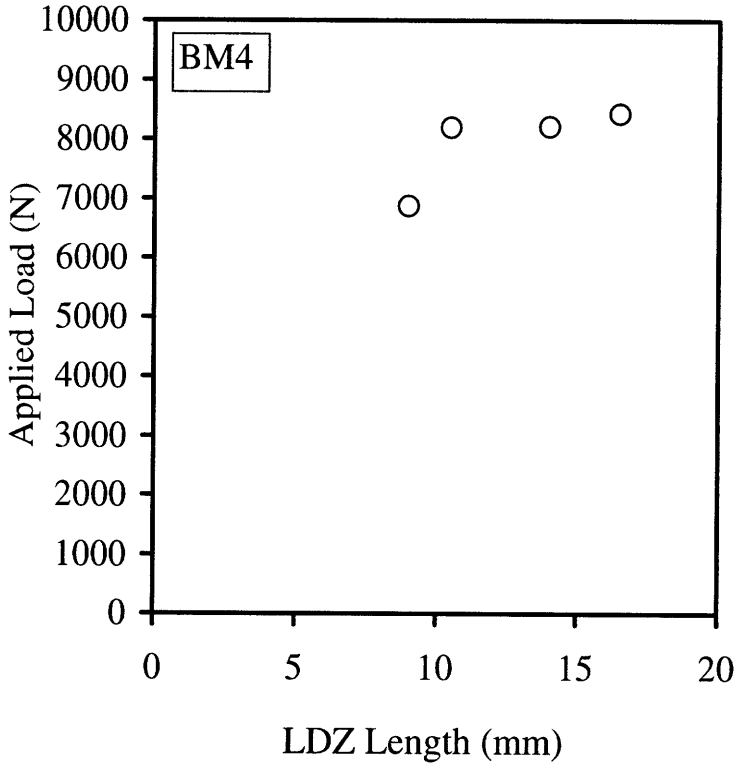

Figure 4.25: Applied load vs. linear damage length (BM4).

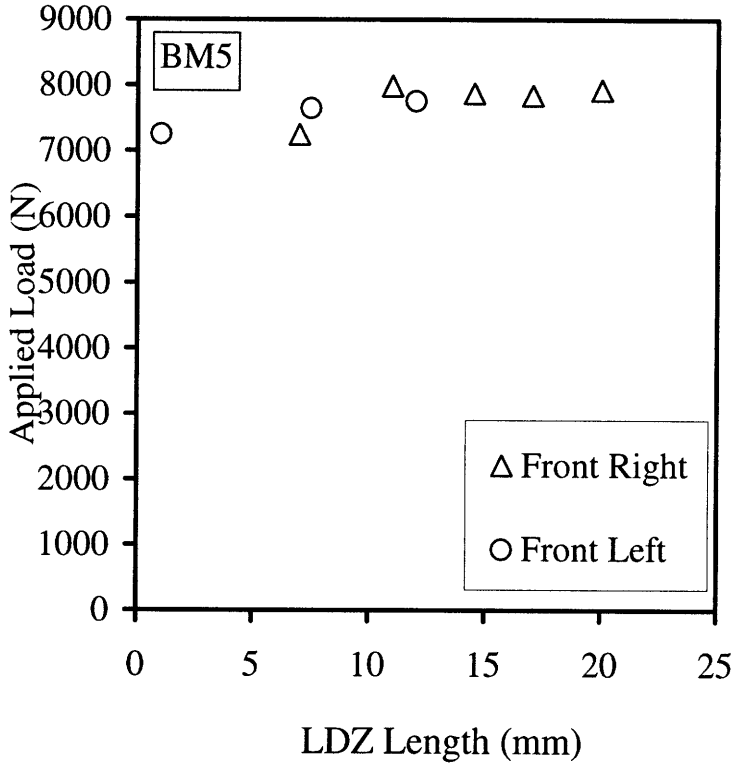

Figure 4.26: Applied load vs. linear damage length (BM5).

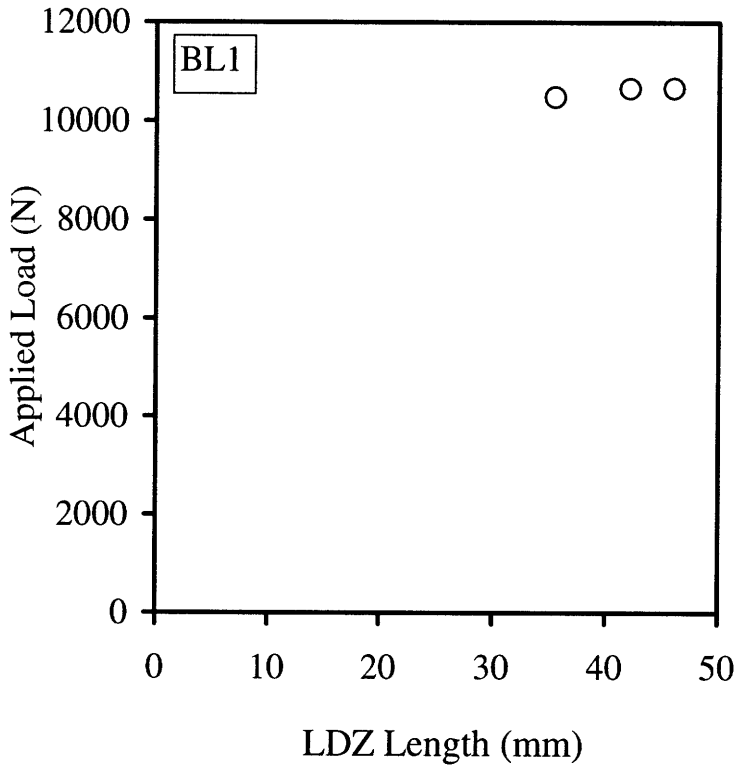

Figure 4.27: Applied load vs. linear damage length (BL1).

4.4 Summary

The observations and measurements presented in this chapter can be summarized as follows:

(1) All tests were performed under acceptable alignment conditions, with a maximum ratio of bending to axial strain of 15%, and in most cases better than 5%.

(2) The extent of stable sub-critical damage growth of the test coupons was affected by panel size and material system: large panels exhibited more controlled sub-critical damage growth than medium and small ones, and T45 series coupons were less "brittle" than T0 series ones.

(3) Experimental values for facesheet stiffness are in good agreement with calculated values derived from classical laminated plate theory.

(4) Both material systems exhibit a decrease in ultimate facesheet compressive stress with increasing panel size.

(5) Sub-critical damage was detected audibly in all coupons, and visually only in the less "brittle" ones (medium- or large-sized panels).

(6) Visual sub-critical damage manifested itself in one of two forms: a linear damage zone (LDZ) or a delamination/bulge zone (DBZ). LDZ's were observed in both material systems whereas DBZ's were exclusive to T45 series coupons.

(7) *Post-mortem* damage evaluation revealed multiple damage mechanisms, including delamination, fiber micro-buckling, shear crimping and matrix cracking.

(8) Fiber micro-buckling, surrounded by delamination, was identified as the driving failure mechanism.

(9) Strain measurements in the cohesive zone confirm that the damage zones retained some load carrying capability.

(10) LDZ length observations were correlated with applied load to produce simple forms of resistance curves depicting the need for an increase in applied load to grow the crack, which is consistent with well-established laminated material behavior.

Chapter 5

Presentation of Models

5.1 Foreword

There is a wide variety of well-established analytical models that can be applied to the damage and failure behaviors observed and described in this work. Some examples of these are empirical correlations, damage zone and delamination propagation models.

Empirical models [44-47], which usually involve a simple correlation between material and geometrical parameters and the strength of the coupon, are very effective in describing the failure load of many materials. However, they have no true predictive capability since every specific material system and geometry requires individual testing to calibrate the model. This means that an expression that works for one particular laminate, with specific dimensions and material properties, may not work for a different coupon type or loading case. This requires extensive testing which results in a very cost-inefficient model. In addition, empirical models provide no insight as to the damage mechanisms which govern failure.

Cohesive or damage zone models [25,34,49] appear to have more potential to offer a genuine predictive capability. These models assume a "crack-like" damage zone, which retains some load carrying capability. Although such damage zones are not always observed, these models appear to offer an increased physical basis. By simplifying and lumping into one the multiple and co-existent damage modes, it is possible to develop an analytical model for the propagation of damage until final failure. If a physical basis can be introduced into such models which enables materials exhibiting similar failure behavior to be modeled in a similar manner, the predictive capacity of damage zone models could be significantly increased, which would presumably translate into reduced costs in the design and operation phases of the product cycle.

Delamination/buckling models [40-42] have been implemented recently for composite laminates. The observed delaminations are modeled as buckled columns, and the necessary loads to initiate and propagate the delamination are calculated. Existing models have studied the propagation of the delamination/buckle along the load direction. Observations in the present work (see Chapter 4), however, exhibit this type of failure initiating at a notch tip and propagating in a direction perpendicular to the load direction. If the existing models can be modified to represent the observed behavior, they might be capable of describing the propagation of these bulges. As for the proposed cohesive zone model, this model would have a built-in physical basis which would make it possible to use it on other material systems exhibiting the same damage mechanism.

The application of these three modeling approaches to the present work is discussed below in detail, and a brief note follows on the future implementation of finite element (FE) modeling.

5.2 Mar-Lin Correlation

This semi-empirical model was originally developed to correlate/predict the strength of notched composite laminates loaded in tension [45]. The model has

subsequently been applied to laminates loaded in compression with reasonable success [44,46]. For tensile loading, it was originally proposed that this model had a physical basis due to the relationship between a macroscopic crack in a composite laminate and a micro-crack at the fiber/matrix interface. However, subsequent analysis suggests that this argument is dubious, particularly in compression. The successful application of this model to compressive loading is more an indication of the utility of the general form of the correlation than an indication that similar damage mechanisms occur in all composite systems and loading cases.

Good agreement with experimental data is achieved by use of a simple equation that relates applied far-field failure stress (σ_f) to notch length ($2b$):

$$\sigma_f = H_c (2b)^{-m} \tag{5.1}$$

where H_c is a composite fracture parameter and m is related to the singularity of the crack tip at the micro-mechanical level. These two correlation parameters must be determined by testing, making this an empirical method.

Since small variations in the experimental data can result in large variations in m if both parameters are determined by a logarithmic least-squares best fit, some researchers [44,47] have fixed m based on the theoretical value of the singularity of a crack at a bi-material interface [48]. For typical Graphite/Epoxy material systems, the value of m is 0.28.

Material System	H_c (MPa cm$^{0.28}$)	m
T45 Series	113	0.28
T0 Series	154	0.28

Table 5.1: Mar-Lin correlation parameters for T45 and T0 series.

The value of m is hence fixed at 0.28 for all coupons in this work. In order to determine the value of H_c for the two material systems tested (T45 and T0 series), its

value is calculated from Equation 5.1 for each test coupon. These values are then averaged and a value for H_c is obtained for each test series (see Table 5.1). This calculated value of H_c is then inserted into Equation 5.1 to predict the notched strength of laminates of the same material system with different notch sizes.

5.3 Damage Zone Model (DZM)

The linear damage zones observed macroscopically in some of the tests resembles that typically seen in monolithic materials which exhibit "R-curve" behavior loaded in tension: a crack emanating from the edge of the notch and propagating perpendicular to load direction along the specimen width. The mechanical behavior is also similar in various ways. First, the damage propagates in a controlled manner with increasing applied load until a certain critical damage length is reached, causing catastrophic failure. This confirms toughening of the material as one of the phenomena taking place. Second, load is transferred across the damaged zone as is revealed by the strain measurements taken directly above it and presented in Chapter 4. This confirms that the crush zone is load-bearing, and further suggests that toughening mechanisms operate in the wake of the damage zone.

Due to the crack-like appearance, some researchers [25,49] have compared the damage zone at each end of the hole to a crack with a plastic zone, and applied the Dugdale model [5] to predict the size of the buckled region as a function of compressive load. For their analysis, they viewed the micro-buckled region as a crack loaded on its faces by a constant stress, which is analogous to the yield stress in Dugdale's model.

In tensile tests with no bridging, the crack would tend to open as the crack propagated, with a specific crack opening profile dictated by the applied load. With bridging in the wake of the crack, the local tractions affect the crack profile and the crack opening displacement (COD) is reduced. The analogy with compressive loading is simple: the applied compressive load produces a crack closing displacement (CCD),

which is affected by the load-bearing crush zone since it provides local stresses that work against the remote compressive load. Therefore, the local tractions reduce the crack closing displacement, resist crack growth and in essence toughen the material.

However, this constant cohesive stress predicts a greater amount of stable micro-buckling growth than is observed in practice, and therefore does not accurately predict the compressive failure stress of notched laminates [34]. A more realistic assumption is that the local cohesive stresses vary as a function of CCD, since fiber micro-buckling reduces the load-bearing capacity of the material. This is confirmed by the strain measurements taken in the cohesive zone described in Chapter 4, which reveal that as the damage zone propagates, the strain (and hence stress) carried by the damage zone is reduced. A linear strain-softening law describes the variation of local stress with crack closing displacement, which has zero stress at the critical CCD (v_c) and a maximum stress (σ_{un}) at zero CCD. The area under the σ-v plot corresponds to the steady-state material fracture energy, G_{SS},

$$G_{SS} = 2\int_0^{v_c} \sigma(v)dv = \sigma_{un} v_c \tag{5.2}$$

which represents the total energy per unit projected area dissipated in the different microscopic failure processes, i.e. fiber micro-buckling, delamination and matrix cracking. A strain softening law is depicted in Figure A2.1 (in Appendix 2).

The linear stress-displacement relationship in the crush zone allows direct calculation of the local tractions σ_i from the local crack surface displacements v_i using the expression:

$$v_i = v_c\left(\delta_i - \frac{\sigma_i}{\sigma_{un}}\right) \tag{5.3}$$

where $\delta_i \equiv 1$ for $i = 1,2,\ldots n$, and n is the number of segments (in x-direction) into which the cohesive zone is divided.

The condition for damage propagation is the following:

$$K_h^S + K_h^\sigma \geq K_{Ic} \tag{5.4}$$

where K_h^S and K_h^σ are the stress intensity factors for a double-cracked open hole specimen due to the remote stress S and to the local bridging stress σ, respectively, and $K_{Ic} = \sqrt{G_c E}$ is the intrinsic material fracture toughness associated with fiber kinking.

The stress intensity factors (SIF), and the crack surface displacements, $v(x)$, are determined from equations for a circular hole in a finite plate which were determined by Newman [50], who modified results from Tada [51] for a crack in an infinite plate. This analysis, further modified by Soutis [34] for a strain softening bridging law, is reproduced in Appendix 2.

It is claimed that the σ-v relationship is a material property, so that the damage tolerant behavior of coupons with different geometries and applied load cases can be described using only one traction law. Knowledge of only two of the three calibrating parameters (G_{SS}, σ_{un} and v_c) is sufficient to predict the behavior of a material, the other is obtained from Equation 5.2.

The intrinsic fracture energy of the material (G_0) can be determined from the tests performed: it is the applied strain energy release rate corresponding to sub-critical damage nucleation. By assuming a very small crack length (of the order of one micron) and using the applied load when damage is first detected, the value of G_0 can be determined. Since different sized panels exhibit damage nucleation at different loads (and hence different stresses), the value of G_0 is taken to be the smallest of the three tested panel geometries. Even though the large panels have the highest failure load, they have the lowest failure stress, and hence it is the value of G when damage initiated for the large panels that is used as G_0.

The critical crack surface displacement (v_c) would ideally also be determined directly from experiment. It is the maximum displacement experienced by the facesheets sliding into each other that still allows for load to be transferred across the damage zone.

5.4 Delamination/Buckling Model (DBM)

5.4.1 Rationale

Some of the T45 series coupons exhibited a very different macroscopic failure mode to the LDZ's, in the form of DBZ's running perpendicular to load direction. Close-up edgewise observation of these DBZ's revealed a delamination between the top 45° ply and the interior plies (see Figure 4.7). The delaminated ply exhibited a curved deformation, typical of Euler buckling, which "popped" in an out-of-plane direction when a critical load was reached. The resulting bulge had the geometry depicted in Figure 4.8, with length Δa (analogous to the crack length described in the DZM) and a width l (which was bound by the slit diameter).

The buckling and propagation problems for delaminations in the absence of stitching have been modeled previously [40,41]. These analyses focus on the delamination propagating parallel to the applied load, which would effectively translate into increasing l in Figure 4.8. However, the present experiments revealed that the width of the bulge (l) remained constant throughout damage propagation, apparently restrained by the diameter of the slit. Therefore, the previous analyses cannot be applied directly to the present problem, yet clearly the two problems are related.

5.4.2 Plate Buckling

Before analyzing the specific problem, it is essential to fully understand the progression of a plate in compression from an un-buckled to a buckled state. Figure 5.1 shows an isotropic buckled plate with modulus E loaded in compression, where u is the

applied displacement, P is the force resulting from u, t is the plate thickness, l is the plate length, and δa is the plate width. The stored elastic strain energy (U_{el}) in the plate and the work done (W) on the plate by the applied displacement are of particular interest in this analysis. Expressions for these terms in the three plate states (un-buckled, buckled and post-buckling) are reproduced below.

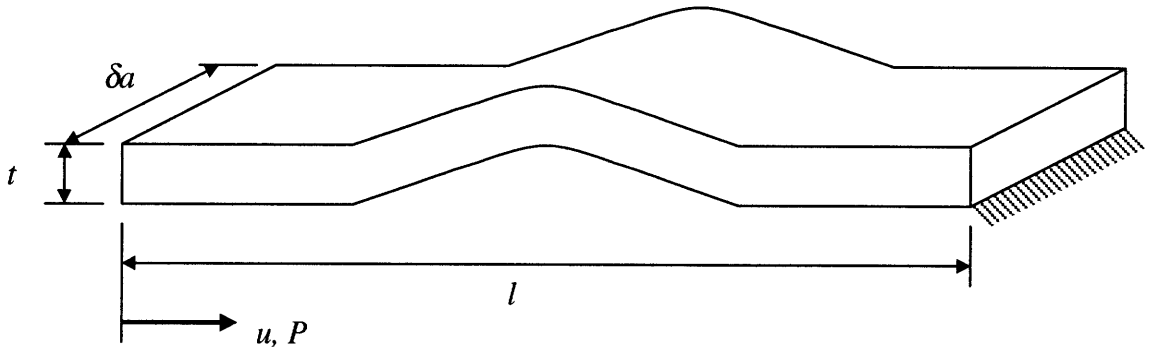

Figure 5.1: Buckled plate loaded in compression.

Before Buckling

$$P = \sigma A \equiv E\varepsilon l \tag{5.5}$$

$$\therefore \quad U_{el} = \frac{\sigma\varepsilon}{2} lt\delta a = \frac{E\varepsilon^2}{2} lt\delta a \tag{5.6}$$

$$\text{and} \quad W = Pu = E\varepsilon A \frac{\varepsilon}{l} = E\varepsilon^2 lt\delta a \tag{5.7}$$

At Buckling

$$P = P_{cr} \equiv \sigma_{cr} A \equiv E\varepsilon_{cr} A = \frac{4\pi^2 EI}{l^2} = \frac{4\pi^2 Et^3 \delta a}{12l^2} \tag{5.8}$$

$$\therefore \quad U_{el} = \frac{E\varepsilon_{cr}^2}{2} lt\delta a \tag{5.9}$$

$$\text{and} \quad W = P_{cr} u_{cr} = P_{cr} \varepsilon_{cr} l \tag{5.10}$$

After Buckling

$$P = P_{cr} \tag{5.11}$$

$$\therefore \quad U_{el} = \left[\frac{E\varepsilon_{cr}^2}{2} + \sigma_{cr}(\varepsilon - \varepsilon_{cr}) \right] lt\delta a = \left[E\varepsilon_{cr} \left(\varepsilon - \frac{\varepsilon_{cr}}{2} \right) \right] lt\delta a \tag{5.12}$$

$$\text{and} \quad W = P_{cr} u = P_{cr} \varepsilon l \tag{5.13}$$

Critical Applied Displacement

An expression for the critical applied strain at which buckling occurs can be obtained from Equation 5.8:

$$\varepsilon_{cr} = \frac{\pi^2}{3} \left(\frac{t}{l} \right)^2 \equiv \frac{u_{cr}}{l} \tag{5.14}$$

5.4.3 Bulge Analysis

It was observed in experiments that the coupons sometimes exhibited a behavior in which a delamination occurred at an interface inside the laminate, creating two sub-laminates. Local buckling was observed to propagate perpendicular to the load direction in the form of a transverse "bulge", and hence it is of particular interest to determine the applied displacements necessary to cause buckling of either of these sub-laminates (u_{cr1} and u_{cr2}), and the associated stored elastic strain energy and work terms associated with each of the sub-laminate states (which are obtained from Equations 5.5 through 5.13). When the applied displacement exceeds either u_{cr1} or u_{cr2}, a single bulge will be formed on the side corresponding to the buckled sub-laminate. When the necessary displacement for the other sub-laminate to buckle is reached, a double bulge will be formed (Figure

5.2). The sub-laminates have moduli E_1 and E_2 and thicknesses t_1 and t_2, respectively. The core is assumed to have negligible stiffness in the load direction.

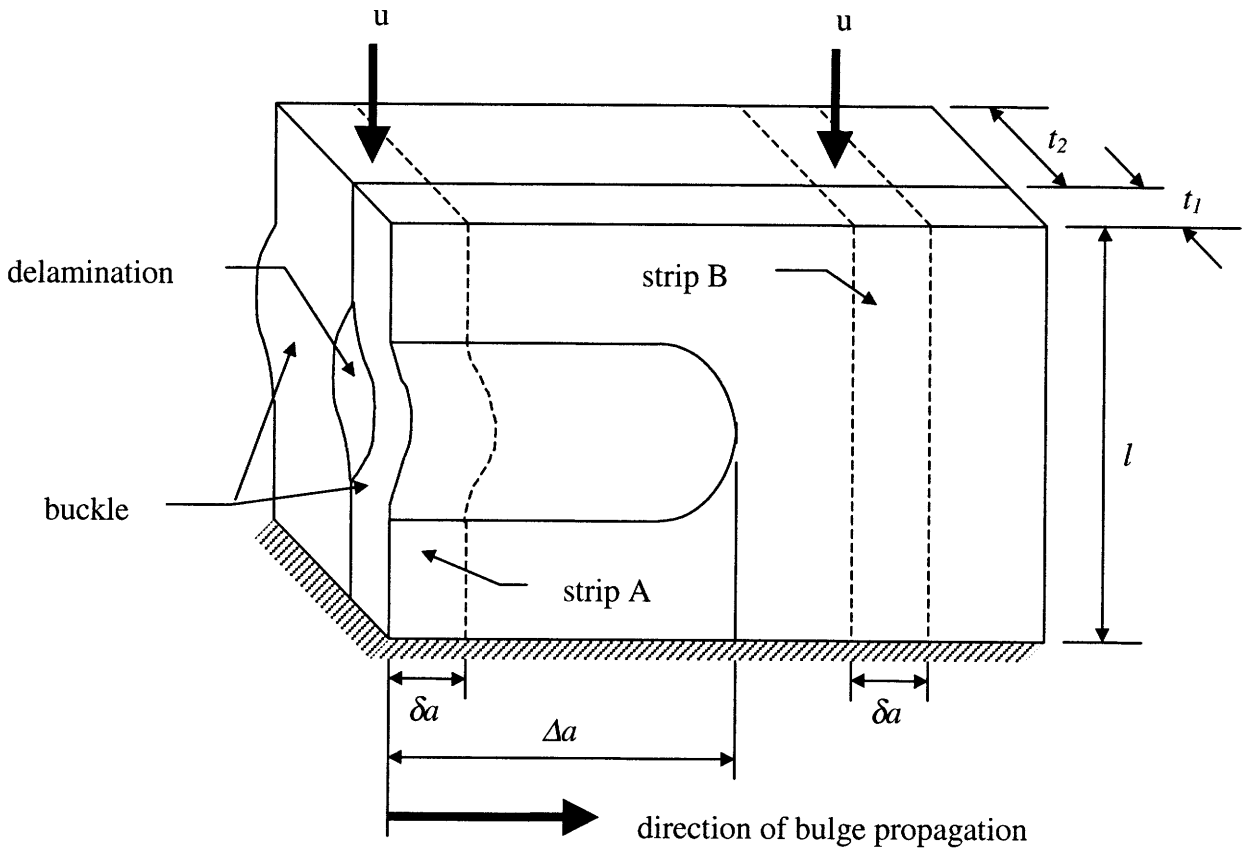

Figure 5.2: Double bulge problem geometry.

From Equations 5.6 through 5.13, it can be inferred that the amount of stored elastic strain energy in the sub-laminates, and the work done on them, depend on the applied displacement. As the sub-laminates change from an un-buckled to a buckled state, the stored elastic strain energy in them is reduced. This progression involves a discontinuity at the critical applied displacements (u_{cr1} and u_{cr2}).

The key difference between strips A and B in Figure 5.2 is that the delamination exists in strip A, and hence the two sub-laminates are free to buckle once their respective critical applied displacements are reached. Strip B, however, is "defect-free", and hence

the two sub-laminates are restrained from buckling and they will not experience an out-of-plane deflection until the energy conditions are favorable.

Hence, for strip A:

if $u < u_{crl}$:

$$\left(U_{el}^{A}\right)_1 = \left[\left(\frac{E_1 t_1}{2l}\right)u^2\right]\delta a \tag{5.15}$$

$$\text{and} \quad \left(W^{A}\right)_1 = \left[\left(\frac{E_1 t_1}{l}\right)u^2\right]\delta a \tag{5.16}$$

if $u = u_{crl}$:

$$\left(U_{el}^{A}\right)_1 = \left[\frac{\pi^4 E_1 t_1^5}{18l^3}\right]\delta a \tag{5.17}$$

$$\text{and} \quad \left(W^{A}\right)_1 = \left[\frac{\pi^4 E_1 t_1^5}{9l^3}\right]\delta a \tag{5.18}$$

if $u > u_{crl}$:

$$\left(U_{el}^{A}\right)_1 = \left[\left(\frac{\pi^2 E_1 t_1^3}{3l^2}\right)u - \frac{\pi^4 E_1 t_1^5}{18l^3}\right]\delta a \tag{5.19}$$

$$\text{and} \quad \left(W^{A}\right)_1 = \left[\left(\frac{\pi^2 E_1 t_1^3}{3l^2}\right)u\right]\delta a \tag{5.20}$$

For the sub-laminate with modulus E_2 and thickness t_2, the expressions are identical to Equations 5.15 through 5.20 except that all subscripts are changed from 1 to 2.

The energy and work terms for strip A hence become:

$$U_{el}^{A} = \left(U_{el}^{A}\right)_1 + \left(U_{el}^{A}\right)_2 \tag{5.21}$$

$$\text{and} \quad W^{A} = \left(W^{A}\right)_1 + \left(W^{A}\right)_2 \tag{5.22}$$

For strip B, there is only one effective laminate and it is restrained from buckling due to its adhesion to the sandwich panel core, so:

$$U_{el}^{B} = \left[\left(\frac{E_1 t_1 + E_2 t_2}{2l}\right)u^2\right]\delta a \tag{5.23}$$

$$\text{and} \quad W^{B} = \left[\left(\frac{E_1 t_1 + E_2 t_2}{l}\right)u^2\right]\delta a \tag{5.24}$$

5.4.4 Bulge Propagation

A fracture mechanics approach is proposed to determine the applied displacement at which the bulge will propagate. The difference between the stored elastic strain energy in each of the strips (U_{el}), and the work done on each of the strips (W), is compared to the energy required to create an equal-width new delaminated surface, and the limiting case provides the necessary condition for damage growth perpendicular to displacement application. Thus:

$$\Delta U_{el} - \Delta W = G_{app}\delta A_{crack} \geq G_c \delta A_{crack} \tag{5.25}$$

where $\Delta U_{el} = U_{el}^{A} - U_{el}^{B}$, $\Delta W = W^{A} - W^{B}$, G_{app} is the applied strain energy release rate, G_c is the material intrinsic fracture energy for delamination and $\delta A_{crack} = l\delta a$.

Depending on the applied displacement, the energy and work terms will change according to the conditional statements from Equations 5.15 through 5.20. Consequently, the terms in Equation 5.25 vary as the applied displacement increases, namely when it reaches the critical applied displacements (for buckling to occur) for the two sub-laminates. As an illustration of the non-linearity of the problem with respect to its geometry and to the applied displacement, the expression for G_{app} for the case where the

thinner sub-laminate (with modulus E_1 and thickness t_1) has buckled, but the thicker one (with modulus E_2 and thickness t_2) has not, is reproduced below:

$$G_{app} = \left(\frac{E_1 t_1}{2l^2} \right) u^2 - \left(\frac{\pi^4 E_1 t_1^5}{18 l^4} \right) \tag{5.26}$$

Then, from Equation 5.25 it can be stated that bulge propagation will occur when

$$G_{app} \geq G_c \tag{5.27}$$

from which the applied displacement for bulge propagation (u_{prop}) can be obtained.

5.5 Finite Element Modeling

Finite element (FE) codes have become very popular due to their increased modeling power compared to conventional analytical methods. The three-dimensional stress states occurring in multi-layered materials, such as composite materials, further complicates analysis, even with FE codes. Nevertheless, such modeling of the specimens tested could be used to verify some of the experimental observations.

Strain mappings of the damage propagation zone can be obtained through appropriate modeling of the cohesive zone with elastic spring elements. Such strain distributions could then be compared to the strain measurements taken experimentally, thus providing extra arguments for the compatibility of the bridging law utilized.

FE implementation in this work was left as a possibility for future research.

5.6 Summary

The application of each of the described models and the comparison of their respective results to the experimental observations will determine the predictive capability of each of the models. The following chapter focuses on evaluating the usefulness of each model in improving the effectiveness of the design process for composite sandwich structures.

Chapter 6

Discussion

6.1 Sandwich Structures

6.1.1 Alignment Concerns

One of the key issues arising from this work is the validity of the experimental data when applied to a single facesheet. The symmetry of the coupons with respect to the center of the honeycomb core suggests an analytical simplification of the problem by treating each facesheet as if it were loaded individually. Load was applied directly to the facesheets, and the fact that the core's stiffness in the direction of load application is negligible compared to that of the facesheets validates the assumption that the panel faces carried all the load. This is further supported by the observation that sub-critical damage propagated in the facesheets and not in the core, which only experienced damage upon final catastrophic failure.

Such an approach greatly simplifies the task of modeling the damage tolerant behavior of sandwich panels. However, it is essential to verify that even (or close to

even) loading is actually applied in the experiments. The method employed in this work, an alignment metric which is defined in Equation 3.1, provides a measure of the bending of the specimens.

Two major factors contribute to the slight differences in measured strain between front and back facesheets: (1) initial imperfections in the coupon and/or test frame, and (2) sub-critical damage initiation and stable propagation. In essence, both factors lead to bending of the coupon and give rise to the observed misalignment and the bending stresses arising from it.

Ideally, both panel facesheets would be identical in length and width, the core would be perfectly perpendicular to both facesheets, and the top and bottom platens would evenly distribute the applied load between the two facesheets. In practice, however, machining introduces physical defects into the coupons, cure procedures make the bond between the core and the facesheets irregular, and load is not perfectly divided between the two faces. Any one, or a combination of these can induce bending of the coupon during testing.

A facesheet containing an LDZ or a DBZ experiences an additional longitudinal displacement compared to an un-damaged facesheet. In the case of the observed LDZ's, sliding of the material from one side of the damage into the other accounts for the extra displacement. For the DBZ's, axial shortening due to the curved shape of the delaminated sub-laminate results in the additional displacement. In both cases, the side which experienced sub-critical damage would also experience an overall shortening, thus inducing overall bending of the coupon.

One of the important objectives of this work was to characterize the damage mechanisms leading to final failure in an uniaxial compressive loading. Uneven loading of the sandwich panel configuration would lead to a combined loading case consisting of axial stresses superimposed on bending stresses. If these bending stresses are not kept to a minimum during testing, it is more than probable that the observed damage modes are a

result of the mixed loading state and not of uniaxial loading alone. Therefore, any attempts to model the damage behavior as being due to uniaxial loads would produce incompatible results to those obtained experimentally.

ASTM standard C-364 states that the acceptable alignment in compressive tests is for there to be less than a 5% difference in strains between front and back facesheets in the initial stages of loading. Even though these requirements were not fully met for all the tests performed in this work, the results obtained were considered acceptable for individual facesheet compressive behavior description and subsequent modeling.

All tests displayed good alignment in the form of percentage differences below 10% for the most part of the test. Initial alignment values were usually large because strain levels were low for small loads, and hence the denominator in Equation 3.1 is small. As load (and hence strain) levels rise, the denominator becomes larger, and the differences between front and back strain levels become negligible compared to the absolute values of strain, making alignment values very small. Refer to Figure 4.1 for a typical strain percentage difference distribution. The fact that the bending stress decreases, or asymptotes to a constant value, suggests that the apparent bending strains may be due in part to strain gauge misalignment.

6.1.2 Influence of Honeycomb Core

The role of the core in the compressive behavior of the sandwich panels tested is not fully understood at this stage of the project. There is insufficient information to determine conclusively whether the honeycomb influences the damage mechanisms, although some of the qualitative damage observations suggest that it does. In the case of the linear damage zones, they were often seen to grow intermittently, in the facesheet, from one cell wall to another, i.e. the LDZ would stop propagating at the point where the honeycomb cell wall touched the facesheet (Figure 6.1a). This leaves to speculation and future research whether the damage would propagate in a continuous manner in the absence of the honeycomb core, or with a continuous core. In the case of the

delamination/bulge zones, out-of-plane deformations were only detected in the outer plies. This suggests that the core might be restricting similar out-of-plane deformations of the inner plies (Figure 6.1b). This is further discussed in Section 6.4.3.

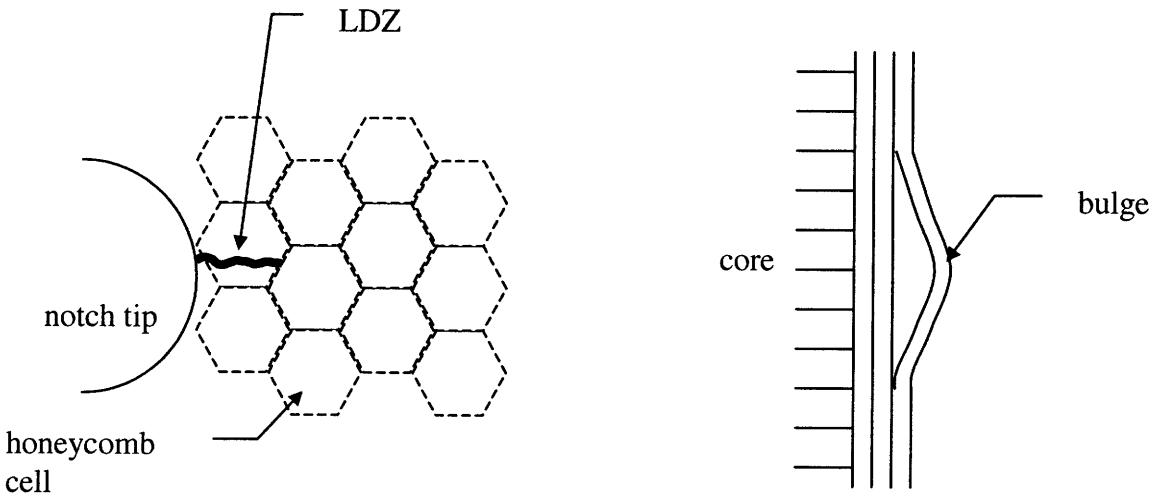

Figure 6.1: Sandwich panel core interactions with damage modes.

6.2 Compressive Behavior

The stress-strain relationship exhibited by most coupons was remarkably linear, as is shown in Figure 4.2. Stiffness is defined as the ratio of applied stress to measured strain. The stiffness values evaluated from experiment are slightly smaller than those computed from classical laminated plate theory. The logical explanation of this discrepancy is that the strain gauges were placed in the wake of the stress concentrations introduced by the presence of the notch. This would mean that the gauges were reading a higher level of strain than the assumed far-field strain, thus reducing the calculated value of stiffness. Nevertheless, the percentage differences between the two are no larger than 20%.

As expected, the stiffer [0/0/0] facesheet coupons (T0 series) displayed a better performance as far as ultimate failure stress is concerned; on the other hand, being more "brittle", they exhibited a lower strain to failure than the more compliant [45/0/0] facesheet coupons (T45 series). It is also interesting to note that there is a significant notch size effect as depicted in Figure 4.3. This plot is consistent with Figure 2.8, and confirms that the toughening mechanisms allow the material to behave somewhere between a notch insensitive and a notch sensitive case.

Sub-critical damage propagation did not always correlate with an increase in the applied stress. In some cases, damage continued to propagate with a constant or even decreasing applied stress. This suggests that there is some critical damage length at which the panel will fail. Even though catastrophic failure may not be instantaneous, as was the case in some panels for which damage growth could be seen to propagate steadily at constant stress levels, the panel has reached its final failure point when this critical length is reached. The damage lengths at which this phenomenon was observed were measured, and larger panels typically allowed more damage growth prior to this point. Stable damage growth was never observed to occur beyond half the ligament width (distance from the edge of the notch to the edge of the coupon), i.e. every time the damage length reached half the ligament width, catastrophic failure was either instantaneous or subsequent damage propagated at decreasing stress levels.

6.3 Failure Mechanisms

6.3.1 General Trends

Although some coupons failed catastrophically without exhibiting sub-critical damage, most of the panels tested experienced stable damage growth. The fact that low displacement rates were employed was essential in allowing such damage propagation.

Experimental damage nucleation, in contrast to the ideal case assumed in the modeling, was never totally symmetric. Only in one panel was sub-critical damage observed to emanate from all four notch tips. The typical behavior was, however, for damage to nucleate only at one notch tip and to continue to propagate along that original path up to catastrophic failure.

Two different macroscopic failure mechanisms were observed in this work: linear damage zones (LDZ's) and delamination/bulge zones (DBZ's). While the latter was only observed in the T45 series coupons, the former was observed in all specimen configurations. Speculation as to the reasons behind this is provided later in Section 6.5. These two damage modes are not mutually exclusive: for example, a T45 series coupon might exhibit DBZ behavior in the outer 45° ply, while the inner 0° plies exhibited LDZ's. This is depicted in Figure 4.7, which shows minor damage in the form of delamination and ply fracture in the inner 0° plies.

Both LDZ's and DBZ's were observed to retain some load carrying capability. LDZ's were mostly composed of fiber kink-bands at the microscopic level, which have proven load-carrying capability. DBZ's consisted of a buckled ply which delaminated from the rest of the coupon, and it is well-established that buckled plates carry load. Conclusively, the local strain gauges at the damage edge verified this residual load bearing capacity.

6.3.2 Delamination

Microscopic inspection of the damage zones revealed extensive delamination occurring in all specimens, irrespective of the macroscopic failure mechanism. Interlaminar stresses build up with applied stress, causing separation at the relatively weak interfaces between the laminate plies compared to the fiber material. This is accentuated by the waviness associated with woven fabrics such as those studied here, since further stress concentrations are introduced at points with maximum curvature.

The fact that delamination was the only damage mechanism detected in all coupons exhibiting sub-critical damage suggests that it is the first failure mode to occur. Microscopy of polished cross-sections confirmed this by revealing that delamination is the only failure mode observed around the tip of the damage. It is hence valid to assume that delamination acts as a precursor to the other damage mechanisms.

6.3.3 Fiber Micro-buckling

The lack of lateral constraint provided by delamination may be the necessary condition for fiber micro-buckling to trigger. Out-of-plane fiber kinking was observed along the damage path on specimens from both series. The sharp fiber breaks observed at either end of the micro-buckle (see Figure 4.16) are consistent with the associated "brittleness" of graphite fiber reinforced material systems.

It is important to point out that fiber micro-buckling was always observed in the 0° plies. Therefore, for the particular case of bulging in a [45/0/0] facesheet, fiber kinking may have been detected in either of the inner 0° plies, whereas the outer 45° ply fibers would have remained intact and experienced the out-of-plane bulging deformation described in Section 4.2.3

Fiber micro-buckling is compatible with load transfer across the damage zone, since the micro-buckled fibers are capable of carrying load. As the crack closing displacement increases, the kink band rotation angle increases and the micro-buckle's ability to carry load is reduced.

6.4 Cohesive Zone Measurements

Load transfer across the damage zone was confirmed by the strain measurements discussed in Section 4.3. The drops in the strain readings for the gauges above the damage path were correlated with the instants when damage was seen to grow past them

(see Figures 4.21 and 4.22). Strain (and hence stress) did not drop to zero, but to some value which corresponds to the zone's residual ability to bear load. This supports the idea of a traction law operating in the cohesive zone. As damage length increased, the strain measured by the gauges decreased. This upholds the reasoning for a strain-softening traction law, since crack closing displacement (the analogy to crack opening displacement for tension) increases with increasing damage length. The more the faces slide into each other, the less stress can be transferred across the damage, until a critical damage length (and its associated critical crack closing displacement) is reached, at which point the damage zone has no load-carrying capability.

The load vs. linear damage length plots presented in Figures 4.23 through 4.27 depict the toughening of the material: an increase in the applied load (and hence stress) is necessary to grow the damage. Again, this toughening can be explained by means of the cohesive zone's ability to carry load in the wake of the LDZ tip.

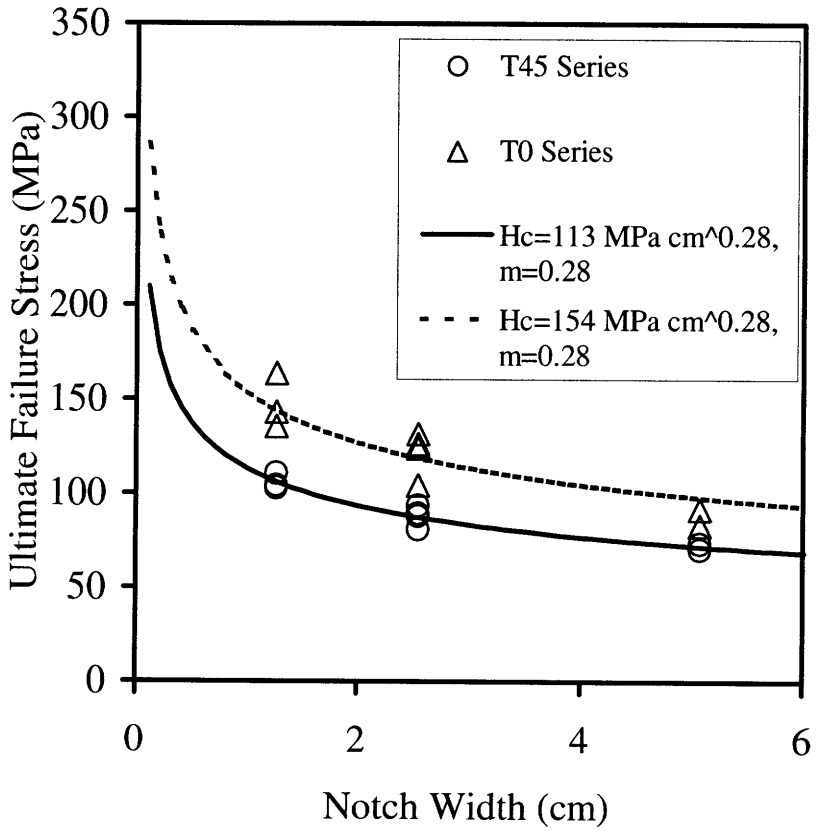

Figure 6.2: Results of Mar-Lin correlation for T45 and T0 series.

6.5 Discussion of Models

6.5.1 Mar-Lin Correlation

This approach yields a good fit (see Figure 6.2) to the experimental data using H_c = 113 MPa cm$^{0.28}$ and m = 0.28 for the T45 series, and H_c = 154 MPa cm$^{0.28}$ and m = 0.28 for the T0 series. The model is merely a fit to experimental data, and it confirms the form of the equation used to describe it. However, it provides no insight as to the actual damage mechanisms taking place, and consequently no predictive capability.

6.5.2 DZM

Damage zone models make use of an important simplifying assumption: that the effect of all the concurrent damage mechanisms can be described by a traction law. This simplification of the damage state around the notch tip allows for analytical treatment of the problem.

Nevertheless, the relevant damage mechanisms must be identified before the traction law can be defined. This was part of this work: to detect all the damage mechanisms and identify the ones leading to toughening of the material and, eventually, to catastrophic failure. Fiber micro-buckling, leading to kink-band formation, was established as the driving mechanism. Its similarity to a bridged crack in tension was used to justify the use of an analogous analysis for the case of compressive loading.

Ideally, the traction law would be a material property such that it could accurately describe the toughening of any sized panel made from the same material. In other words, the traction law would depend on the micro-mechanics of the problem, would be intrinsic to the material's mechanical behavior, and would not be altered by the large-scale effects of panel or notch size.

If this is the case, the toughening of the material should be described using one unique traction law for all sized panels. However, correlation with experimental data could not be obtained for all panel sizes using a unique law. Table 6.1 shows the traction law parameters used for each geometry, and Figure 6.3 shows resistance curves (obtained with the MATLAB™ code reproduced in Appendix 3) for the three panel geometries using the respective traction laws. Damage length was only correlated experimentally with applied load for medium and large coupons (which exhibited the most stable crack growth), and the corresponding data points for three coupons (BM4, BM5 and BL1) are plotted along the predicted behavior for the T0 series.

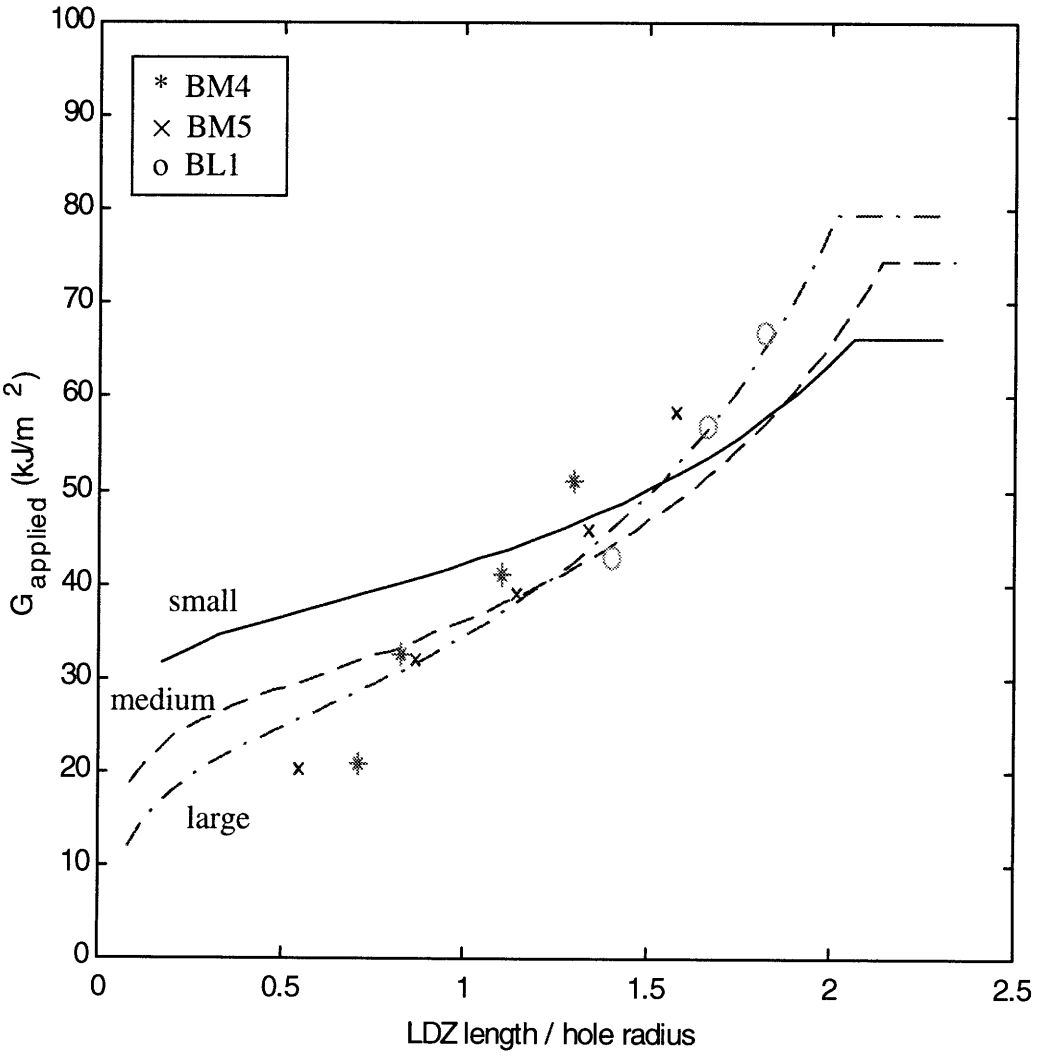

Figure 6.3: Resistance curves and experimental data for T0 series.

Panel Size	v_c (μm)	σ_{un} (MPa)	G_{SS} (kJ m^{-2})
Small	200	85	17
Medium	275	26	7
Large	350	4	1

Table 6.1: Traction law parameters for T0 series.

It is interesting to note from Figure 6.3 that the non-dimensional parameter (LDZ length / hole radius) achieves an effective normalization between the three panel sizes described by the model. Nevertheless, this is probably due to the fact that the three panel geometries investigated have the same notch size to panel width ratio ($a/W = 4$). Varying this ratio for one of the geometries not only displaces the experimental values for that geometry, but also its predicted damage growth behavior.

Despite the good agreement of the predicted toughening behavior with experimental data for the medium and large panel sizes, the ultimate goal of describing damage propagation for a partially-bridged crack with a unique traction law for a specific material system was not achieved.

6.5.3 DBM

The analysis for the propagation of a delamination/buckling type of damage is included in Section 5.4. The expression in Equation 5.26 reveals that the problem is highly non-linear, and therefore cannot be non-dimensionalized.

A series of parametric studies were performed on the bulge propagation model in order to determine the effect that varying one parameter while keeping the others constant had on applied displacement for bulge propagation (u_{prop}). The parameters varied were bulge width (l), ply thickness (t), ply elastic modulus (E), outer ply orientation angle (α) and material intrinsic fracture energy for delamination (G_c). The plots in Figures 6.4 through 6.8 show the results, respectively. A MATLAB™ sample code for a parametric study is included in Appendix 4.

The vertical dotted lines in the plots represent the coupons tested. The values of the different DBM parameters for these coupons are reproduced in Table 6.2. The value for material intrinsic fracture energy for delamination was chosen arbitrarily, acknowledging that resistance to delamination is considerably smaller than resistance to fiber kinking. The value of 300 J/m^2 was used for all parametric studies, and the effect of varying this parameter is depicted in Figure 6.8.

l (cm)	t (μm)	E (GPa)	α (°)	G_c (J/m^2)
0.635	211	57.2	45	300

Table 6.2: Tested coupon values for DBM.

The coupons tested consisted of three-ply facesheet laminates bonded to a non-rigid honeycomb core in a sandwich panel configuration. If the two facesheets are treated separately, there are three possible locations for the delamination to occur: between the outer and the middle plies, between the middle and the inner plies, and between the inner ply and the core. These are labeled cases I, II and III respectively in the plots.

Note that an orientation angle of 45° was chosen for the outer ply in order to differentiate cases I and II (if the outer ply orientation angle were 0°, then a delamination between the outer and middle plies would be equivalent to a delamination between the middle and inner plies, and cases I and II would be superimposed on each other, which is confirmed by the two plots converging at 0° in Figure 6.7).

Figure 6.4 reveals a general decrease in the necessary applied displacement for bulge propagation with increasing bulge width. There is a slight "hump" in the plot around the 7 mm mark, suggesting that there is a critical bulge width which retards bulge propagation while keeping the bulge width small.

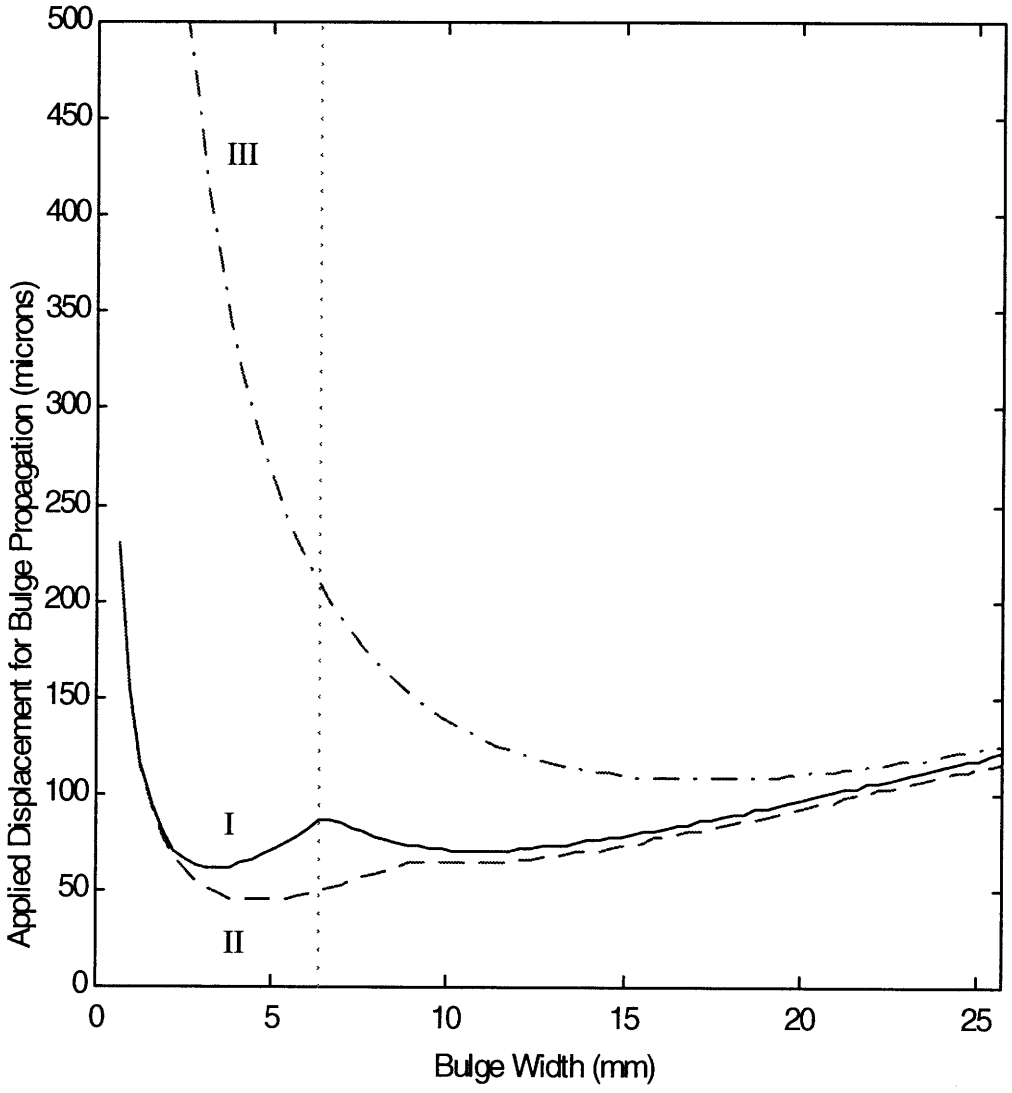

Figure 6.4: Effect of bulge width on applied displacement for bulge propagation.

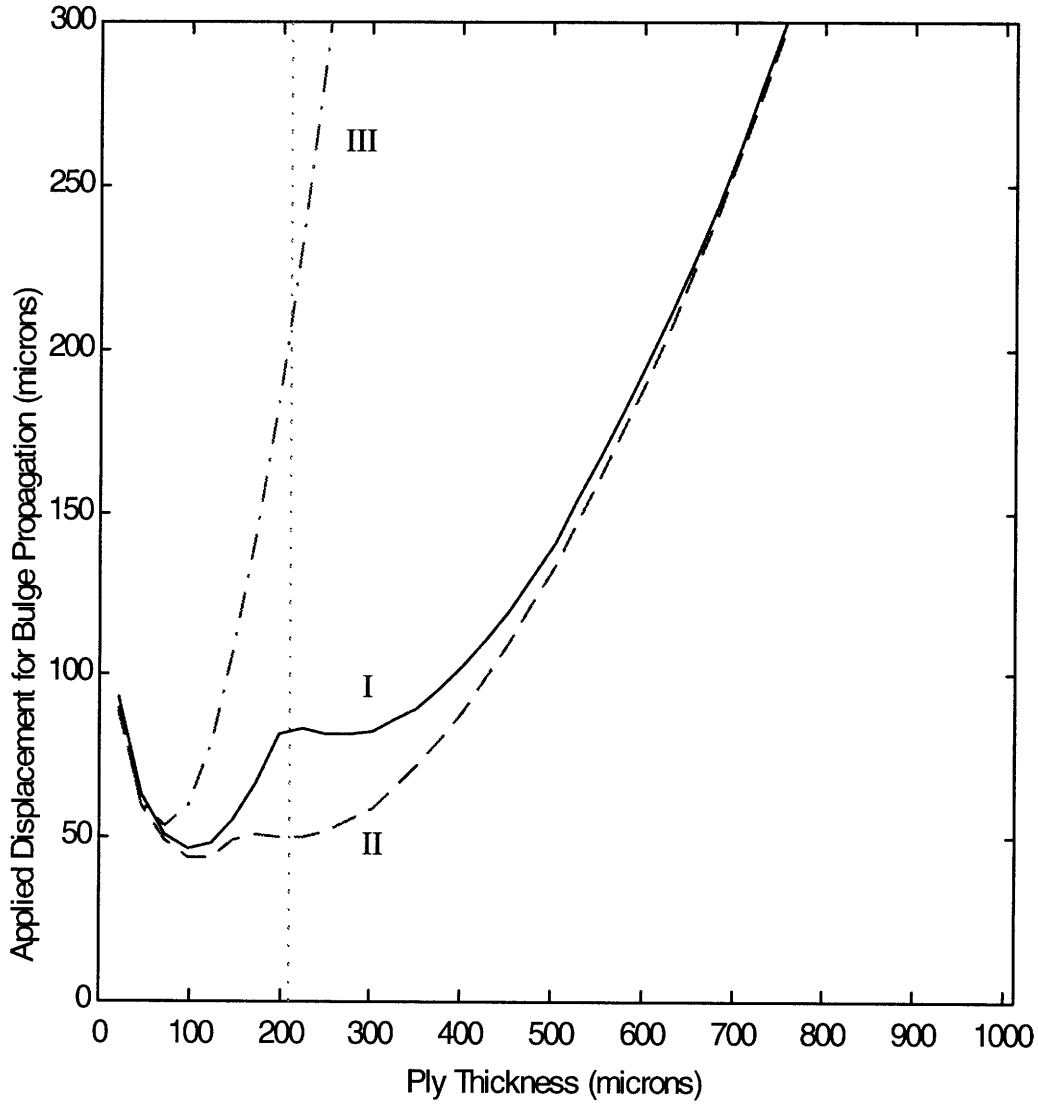

Figure 6.5: Effect of ply thickness on applied displacement for bulge propagation.

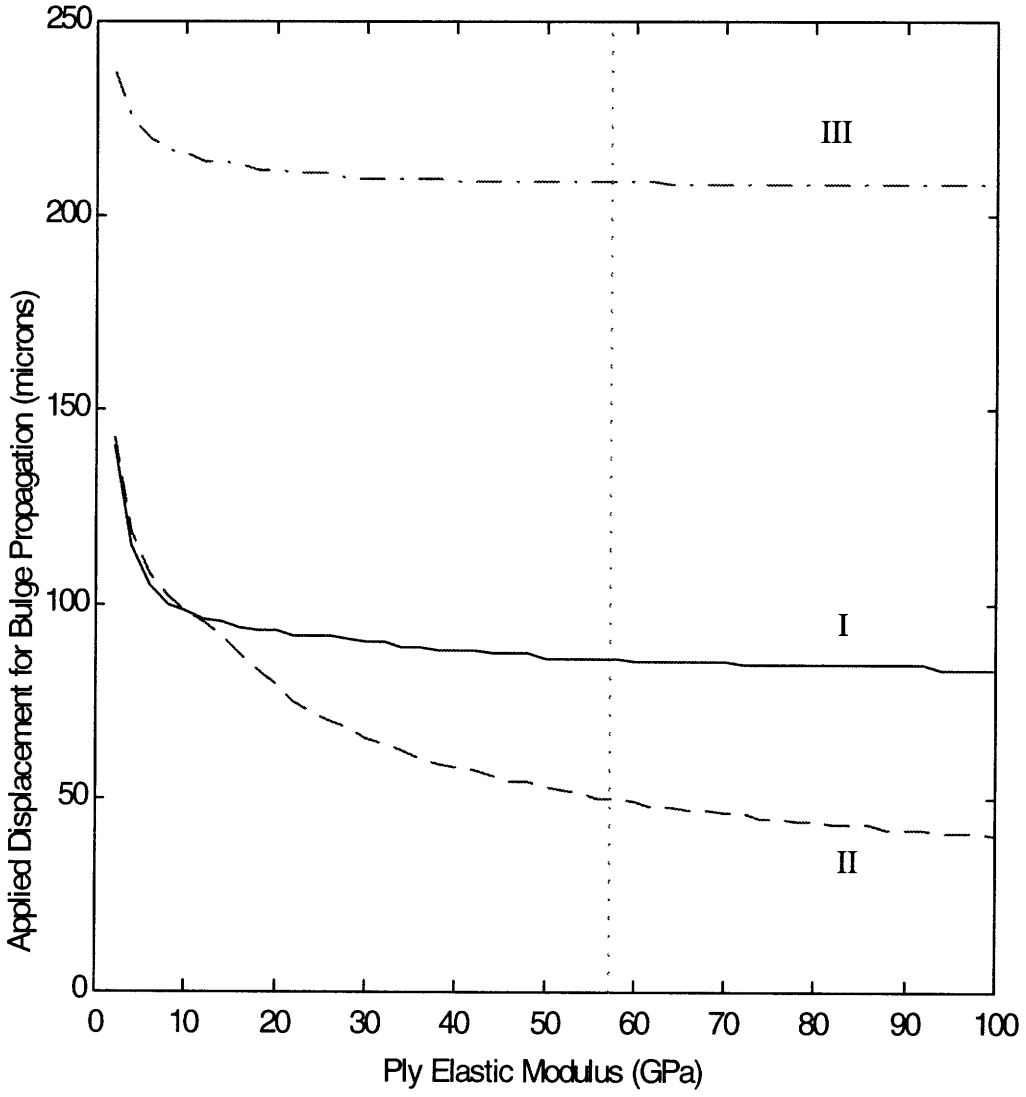

Figure 6.6: Effect of ply elastic modulus on applied displacement for bulge propagation.

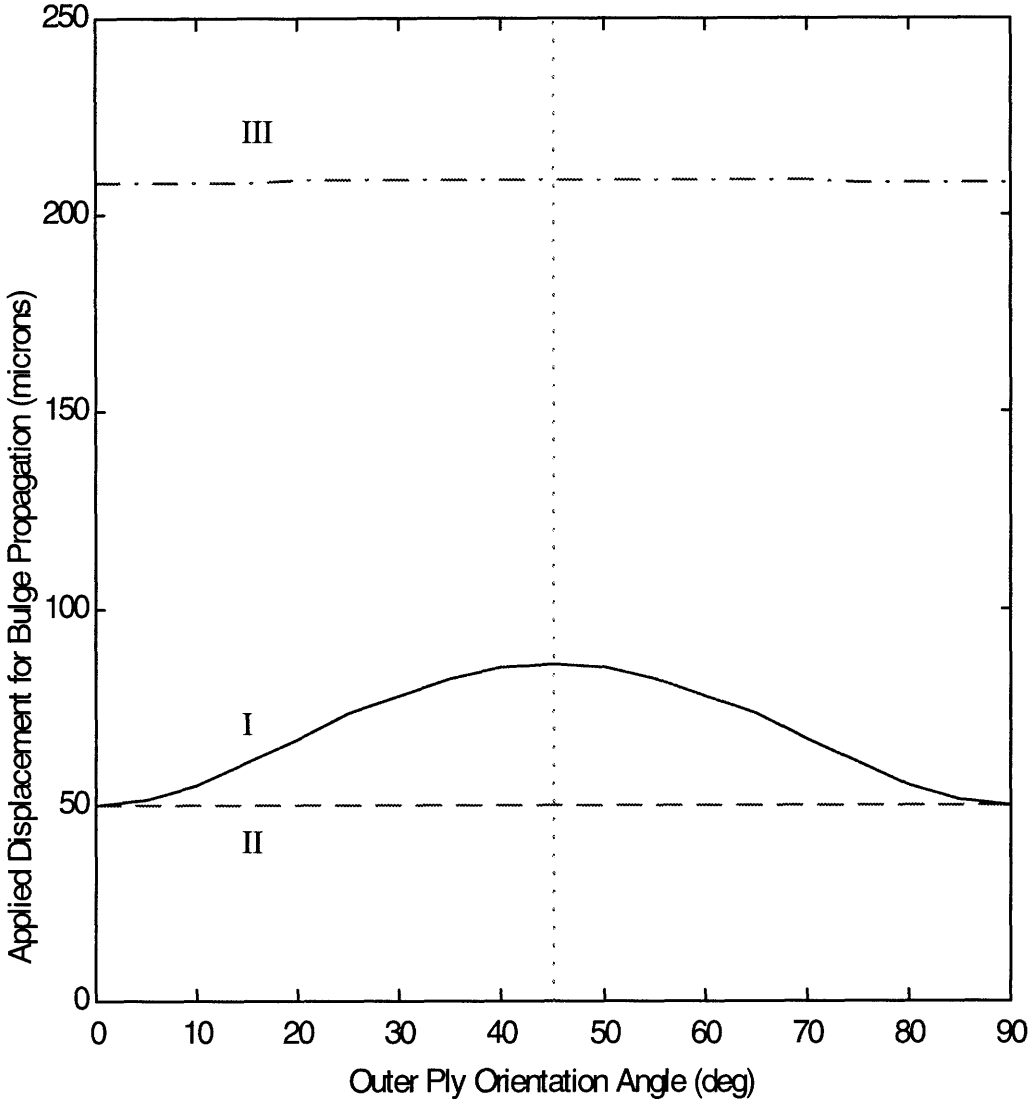

Figure 6.7: Effect of outer ply orientation angle on applied displacement for bulge propagation.

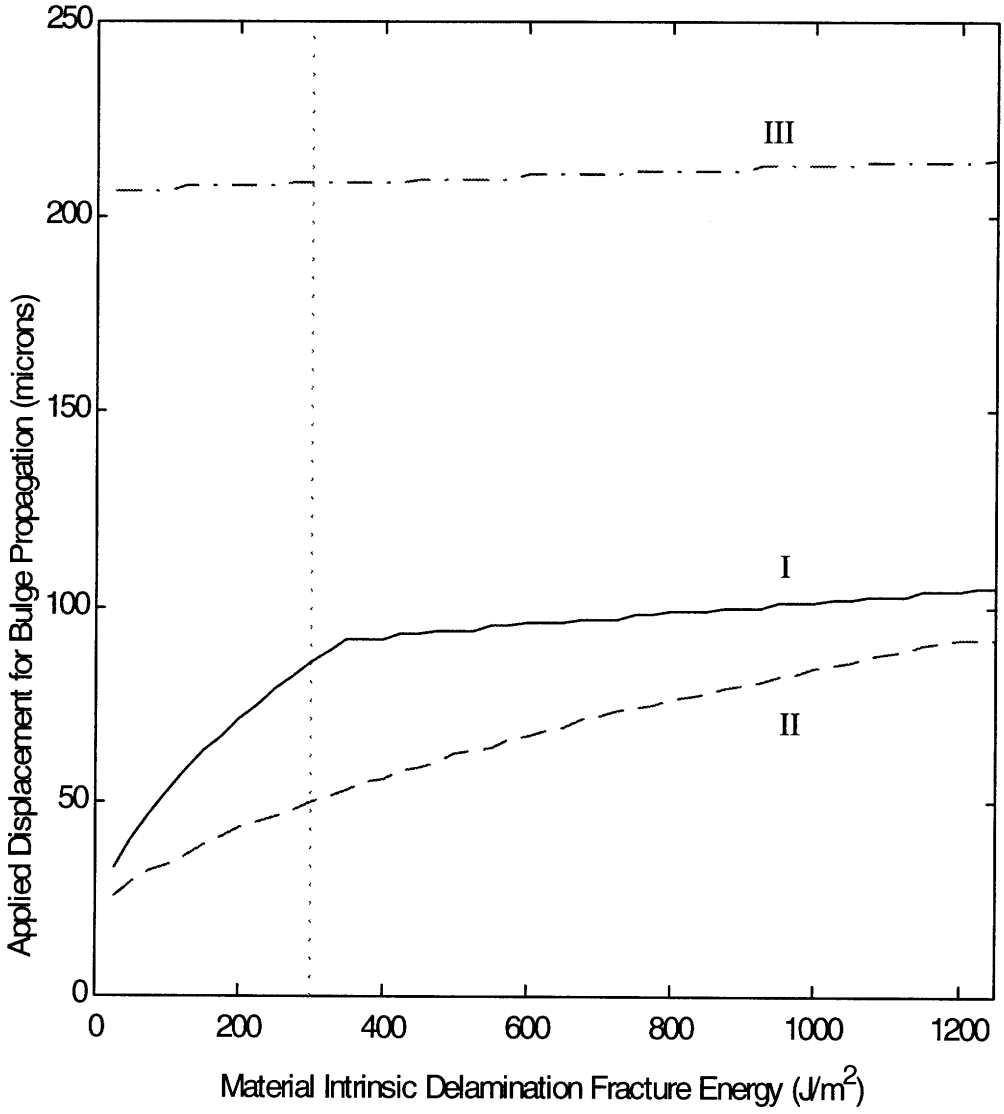

Figure 6.8: Effect of delamination fracture energy on applied displacement for bulge propagation.

A similar behavior is observed in Figure 6.5, which portrays the effect of varying ply thickness on the necessary applied displacement for bulge propagation. In this case, however, the general trend is of an increase in applied displacement with increasing ply thickness. This makes sense, since a thicker ply increases the critical displacement for buckling of the sub-laminates, and hence retards the propagation of the bulge. The "hump" is located around 200 μm, suggesting that a ply thickness of this order is favorable for bulge growth retardation.

The variation of applied displacement for bulge propagation with ply elastic modulus reveals a general decreasing trend with increasing stiffness, but not as pronounced as with bulge width. The stiffer the ply, the more "brittle" it becomes, and hence the earlier it will buckle, which is confirmed in the plot in Figure 6.6.

The symmetry about the 45° outer ply orientation angle in Figure 6.7 is explained by the fact that the fabric is woven, and hence a 0° ply has equal stiffness in the longitudinal and the transverse directions. Hence, a rotation angle of 35° is equivalent to a rotation angle of 55°. The convergence of cases I and II at 0° and 90° is logical. The laminate analyzed is of the [α/0/0] family, and hence when $\alpha = 0°$ or 90°, all plies are the same. Therefore, a delamination occurring between the outer ply and the rest of the laminate is equivalent to one occurring between the inner ply and the rest of the laminate.

The effect of varying the material intrinsic fracture energy on the applied displacement required for bulge propagation is depicted in Figure 6.8. As G_c is increased, the strain energy release rate necessary for bulge propagation increases, and hence more applied displacement is required.

It is worth noting that, in all the parametric studies discussed, a lower applied displacement is predicted for case II. In other words, all other parameters remaining constant, a delamination in the interface between the middle and the inner plies would propagate as a bulge before that in the other two cases. This was not observed in experiments, where case I was always observed. The fact that the core material was not

included in the model might account for this inconsistency with experimental data. The model does not account for the resistance to out-of-plane deformation of the inner ply provided by the core, which may be considered to act as an elastic foundation absorbing the energy released by the inner ply attempting to buckle against it, thereby retarding its buckling.

An additional plot that is of specific interest to this work, and serves as a comparison with experimental data to confirm when bulge-like failure is prone to occur, is that of applied stress for bulge propagation vs. notch size. Figures 6.9 and 6.10 show this comparison for case I (which was the delamination location observed to occur consistently in experiments) for the T45 and T0 series, respectively, and compares the model to experimental data.

The model predicts that bulge-like damage propagation is only possible in large panels, for which the experimental ultimate failure stress is larger than the applied stress required for bulge propagation. It is important to note here that the DBM deals with local applied displacements, which are larger than the far-field applied displacements due to the stress concentrations around the notch tip. Therefore, bulge propagation might occur at a far-field applied displacement that is lower than the calculated local applied displacement. Consequently, bulge propagation will occur at the far-field stress that generates the local applied stress necessary for bulge propagation calculated from the model.

The model predicts that DBZ's are equally likely in the large panels for the T0 series as for the T45 series, which is not consistent with experimental observations (in which bulges were exclusive to the panels with [45/0/0] facesheets). 0° plies are stiffer than 45° plies. Consequently, the strain to failure for a 0° ply is considerably less than that for a 45° ply. In order for the out-of-plane curved deformation in the observed bulges to occur, a certain compressive strain is required. If this minimum strain is larger than the strain to failure, the bulge cannot develop because the ply will fail first. This might be the case with the T0 series, for which bulges would develop if the necessary compressive

strain were reached. For the T45 facesheets, the strain to failure is larger than the strain needed for bulging, and hence DBZ formation is possible for these coupons.

The difference between the predicted and the observed stresses for bulge propagation may also be attributed to the initial ply waviness which effectively reduces the failure stress compared to a perfectly flat ply and is not accounted for in the DBM.

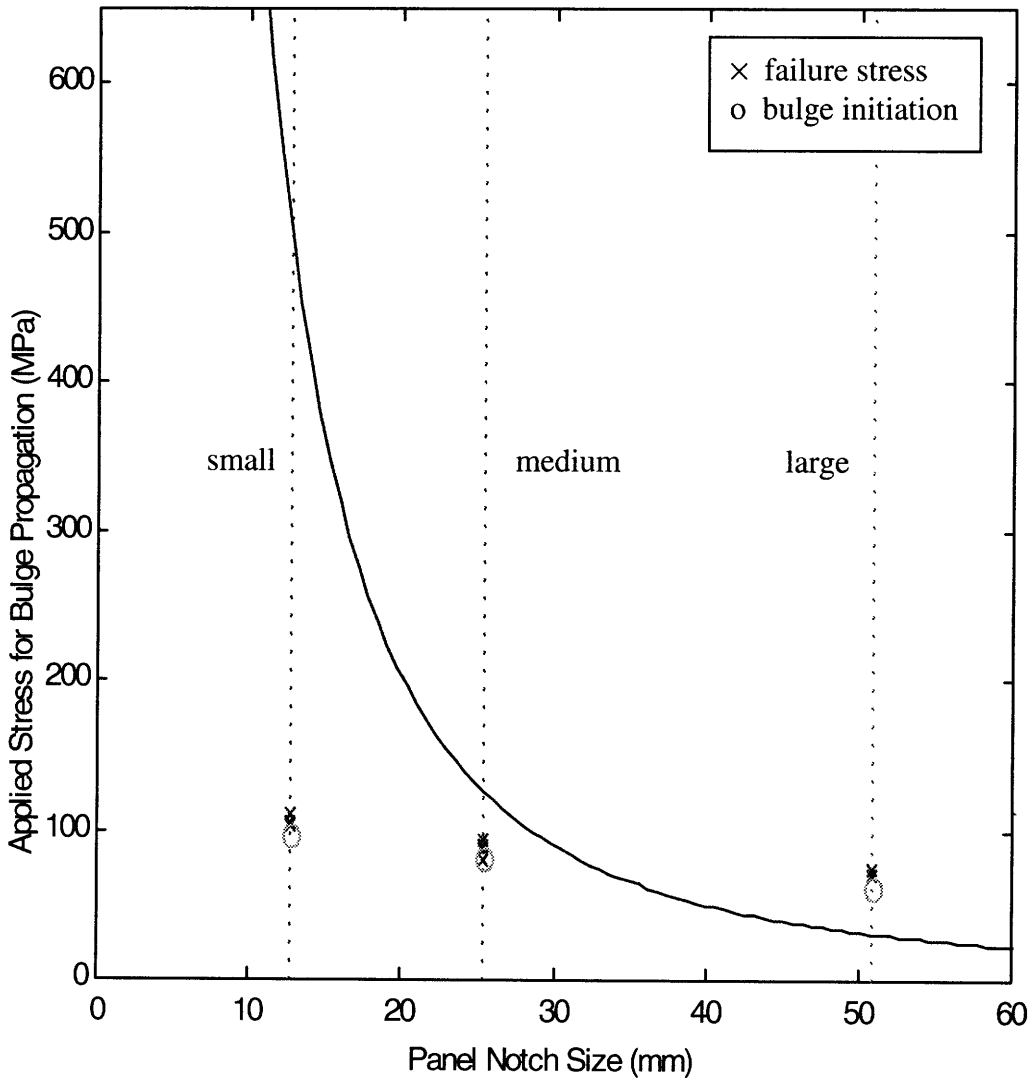

Figure 6.9: Notch size effect on local applied stress for bulge propagation for T45 series.

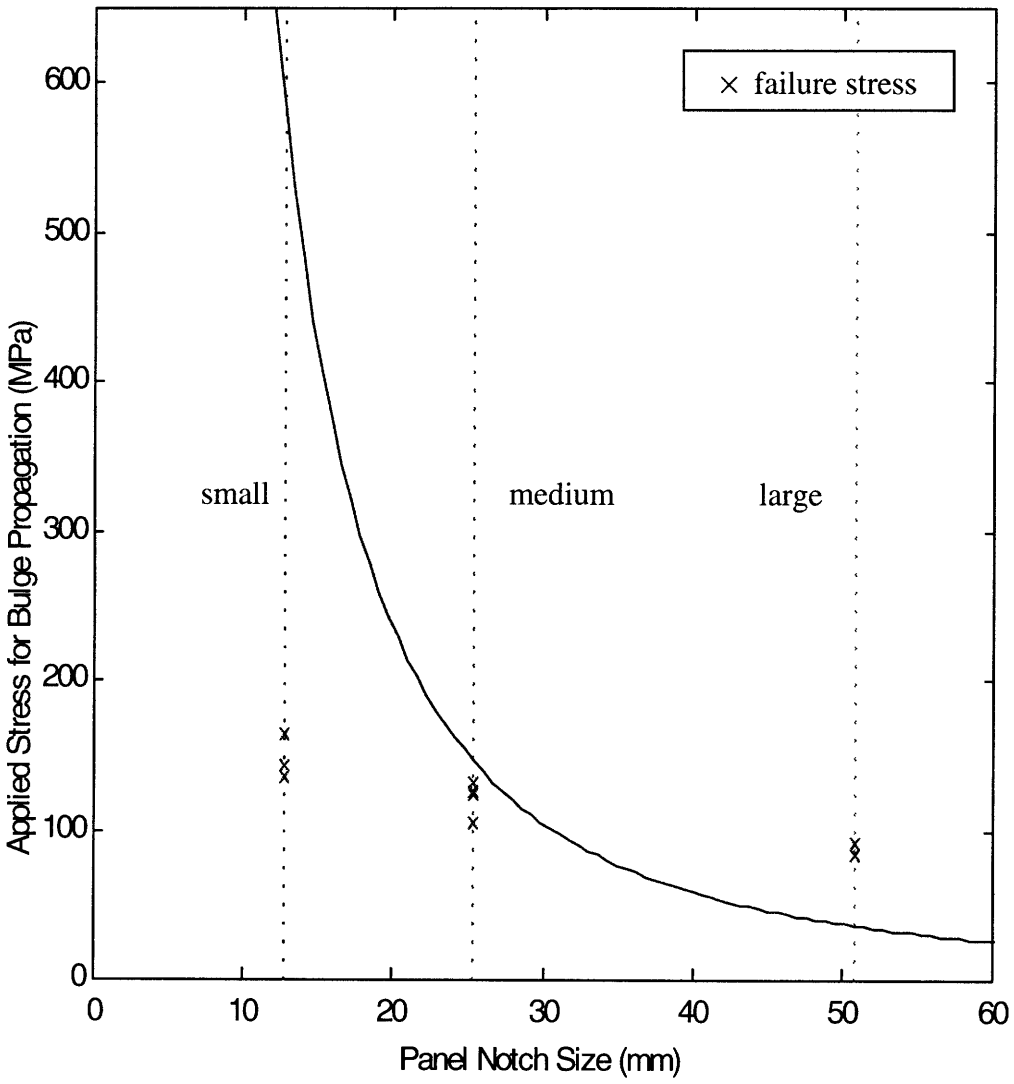

Figure 6.10: Notch size effect on local applied stress for bulge propagation for T0 series.

6.5.4 DZM-DBM Comparison

Fiber micro-buckling was observed in coupons of all geometries for both material systems tested, whereas the macroscopic "bulges" were only observed in T45 series specimens. In some cases where bulge-like damage was observed, *post-mortem* evaluation revealed fiber micro-buckling in the two inner 0° plies.

(all stresses in MPa)	**Panel Size**	σ_{prop} **(DZM)**	σ_{prop} **(DBM)**	σ_{fail} ***(experiment)***
T45 Series	Small	167	500	110
	Medium	118	128	90
	Large	83	28 (*)	70
T0 Series	Small	183	579	150
	Medium	129 (*)	143	130
	Large	91	36 (*)	90

Table 6.3: Predicted damage propagation stresses using DZM and DBM.

The applied stress required for damage propagation using both models is compared to the panel's failure stress in Table 6.3. An asterisk (*) by the stress value indicates the conditions in which sub-critical damage will occur, i.e. the cases where the stress required for damage propagation is lower than the failure stress.

Table 6.4 includes the required stress for damage propagation for DZM and DBM for a range of outer ply orientation angles. Comparing the stresses for each failure mode for equal panel sizes determines the most favorable failure mode, depicted by the shaded boxes for each panel geometry. An extra panel size between the Medium and Large geometries was included in this analysis, labeled as "New" in Table 6.4. The dimensions for this geometry are $W = 15.24$ cm, $H = 45.72$ cm and $2a = 3.81$ cm.

The results in Table 6.4 can be displayed in the form of a diagram. Outer ply orientation angle and notch size are correlated, and the corresponding failure type for each case is labeled: "K" for kink-band formation (LDZ) and "B" for bulging (DBZ). The

plot in Figure 6.11 reveals that the change-over from a LDZ to a DBZ is predicted to occur somewhere between the Medium and New panel geometries. A more comprehensive analysis is necessary to determine the precise location of this change-over. Performing such an analysis places the cross-over location at a notch size of 2.79 cm.

α (°)	σ_{prop} (MPa)							
	Small		**Medium**		**New**		**Large**	
	DZM	**DBM**	**DZM**	**DBM**	**DZM**	**DBM**	**DZM**	**DBM**
0	182	579	129	143	105	73	91	36
10	179	560	127	140	103	67	90	34
20	173	530	122	137	100	63	87	32
30	168	520	119	132	97	58	84	30
40	167	507	118	129	96	56	83	29
45	167	500	118	128	96	55	83	28

Table 6.4: Predicted damage propagation stresses for various panel sizes.

Figure 6.11 is extremely useful because it provides a prediction of the failure mechanism occurring prior to testing with only top ply orientation angle and notch size (assumed to be circular) as inputs.

From Figure 6.11 and experimental observations, it can be concluded that if the energy conditions are favorable for fiber micro-buckling to occur, it will, whereas bulging is not certain to occur even though the energy release upon its creation would be favorable. This is the case for $\alpha = 0°$ for which, according to Figure 6.11, bulging should be the failure mechanism for the larger notch sizes, whereas experiments reveal that only LDZ occurs in the large T0 series coupons.

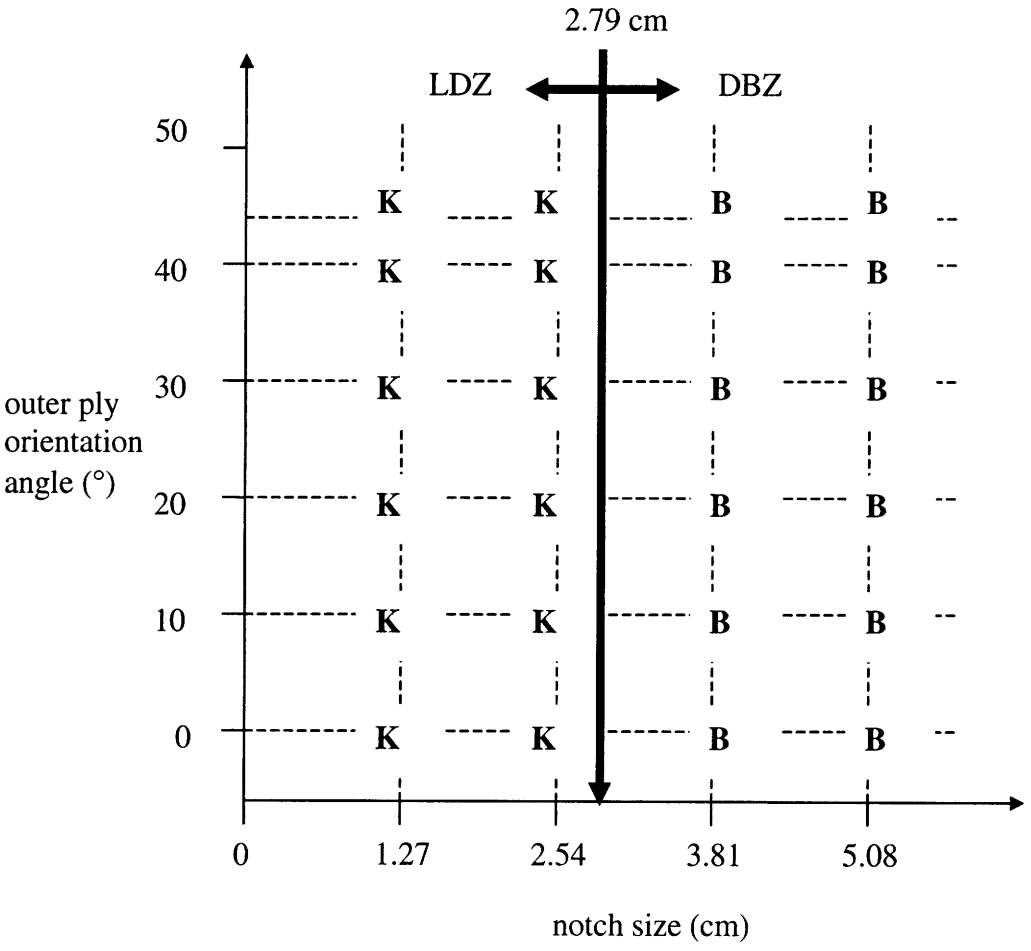

Figure 6.11: Failure mechanism diagram for [α/0/0] laminate family.

Chapter 7

Conclusions

7.1 Project Summary

This project focused on characterizing and modeling the damage mechanisms arising from uniaxial compressive loading of notched sandwich panels with graphite fiber reinforced facesheets and honeycomb cores. Coupons were loaded in displacement control to failure, which was defined as fast fracture of either one of the facesheets from the notch tip to the edge of the coupon. The expected pattern of decreasing ultimate failure stress with increasing notch size was confirmed.

Various damage evaluation techniques were used to describe both qualitatively and quantitatively the observed sub-critical damage. Two microscopic failure modes were identified as the driving mechanisms for catastrophic failure: delamination and fiber micro-buckling. Two macroscopic failure types were observed: linear damage zones (LDZ's) and delamination/bulge zones (DBZ's).

Experimental observations of the damage mechanisms were used to model damage growth using two approaches: damage zone models and delamination/buckling models. Both modeling approaches are consistent with the reported ability of the crush zone to carry load. From the analysis, large panels are more prone to fail via DBZ whereas smaller panels will tend to form LDZ's.

Comparison between the predicted failure mechanisms and those observed experimentally leads to the conclusion that fiber micro-buckling will always occur if the required applied stress is reached for its nucleation, whereas the out-of-plane deformation involved in bulge propagation will not occur every time its required applied stress is reached.

7.2 Recommendations for Future Study

The following list presents some suggestions for future research in this area:

- Testing of a more comprehensive family of laminates to fully understand the effect of outer ply orientation angle on the failure mechanism.
- Change stacking sequence to place the angled ply in the middle and determine whether bulging is still observed.
- Test round holes as well as round-edged slits to determine the differences, if any.
- Test different notch size to panel width ratios.
- Experimental strain mapping of the area around the notch tip to obtain a two-dimensional picture of the stress state around the damage.
- Investigate the implementation of new non-destructive evaluation techniques to describe sub-critical damage with more precision.
- Finite element modeling of a bridged crack to determine a strain distribution around the notch tip and compare it to the measured strain values in the cohesive zone.

- Include core material in DBM and model its resistance to out-of-plane deformations of the inner plies.
- Explore effects of fiber waviness on modeling.
- Test facesheets individually to determine the experimental issues arising from sandwich panel configuration. Use anti-buckling guide to prevent large-scale buckling.

References

[1] Lagace, P.A., Spearing, S. M. and McManus, H. L., "A proposed Design Methodology for the failure and Durability of Composite Structures", *Technology Laboratory for Advanced Composites (TELAC) Report 96-14, Department of Aeronautics and Astronautics, Massachusetts Institute of Technology*, 1996.

[2] Bäcklund, J., "Fracture Analysis of Notched Composites", *Computers and Structures, Vol. 13, pp. 145-154*, 1981.

[3] Sørensen, B. F. and Jacobsen, T. K., "Large Scale Bridging in Composites: R-Curves and Bridging Laws", *Composites Part A – Applied Science and Manufacturing, 29 (11), pp. 1443-1451*, 1998.

[4] Spearing, S. M. and Evans, A. G., "The Role of Fiber Bridging in the Delamination Resistance of Fiber-Reinforced Composites", *Acta Metall. Mater., Vol. 40, No. 9, pp. 2191-2199*, 1992.

[5] Dugdale, D. S., "Yielding of Steel Sheets Containing Slits", *Journal of the Mechanics and Physics of Solids, 8, pp. 100-108*, 1960.

[6] Spearing, S.M., "Direct Calibration of Damage Zone Models", *Technology Laboratory for Advanced Composites (TELAC), Department of Aeronautics and Astronautics, Massachusetts Institute of Technology*, 1996.

[7] Afaghi-Khatibi, A., Ye, L. and Mai, Y. W., "An Effective Crack Growth Model for Residual Strength Evaluation of Composite Laminates with Circular Holes", *Journal of Composite Materials, Vol. 30, No. 2, pp. 142-163*, 1996.

[8] Bäcklund, J. and Aronsson, C. G., "Tensile Fracture of Laminates with Holes", *Journal of Composite Materials, Vol. 20, pp. 259-286*, 1986.

[9] Dopker, B., Murphy, D. P., Ilcewicz, L. and Walker, T., "Damage Tolerance Analysis of Composite Transport Fuselage Structure", *AIAA/ASME/ASCE/AHS/ ASC Structures, Structural Dynamics, and Materials Conference, 35th, Hilton Head, SC, Apr. 18-20, 1994, Technical Papers, Part 2 (A94-23876 06-39), Washington D.C., American Institute of Aeronautics and Astronautics, pp. 803-810*, 1994.

[10] Eriksson, I. And Aronsson, C. G., "Strength of Tensile Loaded Graphite/Epoxy Laminates Containing Cracks, Open and Filled Holes", *Journal of Composite Materials, Vol. 24, pp. 456-482*, 1990.

[11] Walker, T. H., Ilcewicz, L. B., Polland, D. R. and Poe, C. C. Jr., "Tension Fracture of Laminates for Transport Fuselage, Part II: Large Notches", *private communication.*

[12] Minguet, P., Dugundji, J. and Lagace, P. A., "Buckling and Failure of Sandwich Plates with Graphite-Epoxy Faces and Various Cores", *Journal of Aircraft, Vol. 25, No. 4, pp. 372-379*, 1987.

[13] Kassapoglou, C., Fantle, S. C. and Chou, J. C., "Wrinkling of Composite Sandwich Structures Under Compression", *Journal of Composites Technology & Research, JCTRER, Vol. 17, No. 4, pp. 308-316*, 1995.

[14] Hoff, N. J. and Mautner, S. E., "The Buckling of Sandwich Type Panels", *Journal of Aeronautical Sciences, pp. 285-297*, 1945.

[15] Yussuff, S., "Face Wrinkling and Core Strength in Sandwich Construction", *Journal of the Royal Aeronautical Society, Vol. 64, pp. 164-167*, 1960.

[16] Gutierrez, A. J. and Webber, J. P. H., "Flexural Wrinkling of Honey-comb Sandwich Beams with Laminated Faces", *International Journal of Solids and Structures, Vol. 16, pp. 645-651*, 1980.

[17] *Structural Sandwich Composites*, MIL-HDBK-23, Ch. 3, U.S. Department of Defense, Washington, DC, 1968.

[18] Webber, J. P. H., Kyriakides, S. and Lee, C. T., "On the Wrinkling of Honeycomb Sandwich Columns with Laminated Cross-Ply Faces", *Aeronautics Journal, pp. 264-272*, 1976.

[19] Lagace, P. A. and Vizzini, A. J., "The Sandwich Column as a Compressive Characterization Specimen for Thin Laminates", *Composite Materials: Testing and Design (Eighth Conference), ASTM STP 972, J. D. Whitcomb, Ed., American Society for Testing and Materials, Philadelphia, pp. 143-160*, 1988.

[20] Kim, R. Y. and Crasto, A. S., "A Longitudinal Compression Test for Composites Using a Sandwich Specimen", *Journal of Composite Materials, Vol. 26, No. 13, pp. 1915-1929*, 1992.

[21] *Standard Test Method for Edgewise Compressive Strength of Sandwich Constructions*, ASTM Standard, Designation C 364 – 94.

[22] Hahn, H. T. and Williams, J. G., "Compression Failure Mechanisms in Unidirectional Composites", *Composite Materials: Testing and Design (Seventh Conference), ASTM STP 893, J. M. Whitney, Ed., American Society for Testing and Materials, Philadelphia, pp. 115-139*, 1986.

[23] Greszczuk, L. B. in Proceedings, *2nd USA-USSR Symposium on Fracture of Composite Materials, G. C. Sih, Ed., pp. 231-246*, 1981.

[24] Williams, J. G. and Rhodes, M. D., "The Effect of Resin on the Impact Damage Tolerance of Graphite/Epoxy Laminates", *NASA TM 83213, National Aeronautics and Space Administration*, 1981.

[25] Guynn, E. G., Bradley, W. L. and Elber, W. "Micromechanics of Compression Failures in Open Hole Composite Laminates", *Composite Materials: Fatigue and Fracture, Second Volume, ASTM STP 1012, Paul A. Lagace, Ed., American Society for Testing and Materials, Philadelphia, pp. 118-136*, 1989.

[26] Guynn, E. G. and Bradley, W. L., "Measurements of the Stress Supported by the Crush Zone in Open Hole Composite Laminates Loaded in Compression", *Journal of Reinforced Plastics and Composites, Vol. 8, pp. 133-149*, 1989.

[27] Fleck, N. A., Jelf, P. M. and Curtis, P. T., "Compressive Failure of Laminated and Woven Composites", *Journal of Composites & Technology Research, JCTRER, Vol. 17, No. 3, pp.212-220*, 1995.

[28] Soutis, C., Fleck, N. A. and Smith, P. A., "Failure Prediction Technique for Compression Loaded Carbon Fibre-Epoxy Laminate with Open Holes", *Journal of Composite Materials, Vol. 25, pp. 1476-1498*, 1991.

[29] Soutis, C. and Fleck, N. A. "Static Compression Failure of Carbon Fibre T800/924C Composite Plate with a Single Hole", *Journal of Composite Materials, Vol. 24, pp. 536-558*, 1990.

[30] Jelf, P. M. and Fleck, N. A., "Compression Failure Mechanisms in Unidirectional Composites", *Journal of Composite Materials, Vol. 26,No. 18, pp. 2706-2726*, 1992.

[31] Budiansky, B and Fleck, N. A., "Compressive Failure of Fibre Composites", *J. Mech. Phys. Solids, Vol. 41, No. 1, pp.183-211*, 1993.

[32] Williams, T. O. and Cairns, D. S., "A Model for the Compressive Failure of Composite Materials", *Journal of Composite Materials, Vol. 28, No. 2, pp. 92-111*, 1994.

[33] Barbero, E. J., "Prediction of Compression Strength of Unidirectional Polymer Matrix Composites", *Journal of Composite Materials, Vol. 32, No. 5, pp. 483-502*, 1998.

[34] Soutis, C., "Compressive Failure of Notched Carbon Fibre-Epoxy Panels", *Ph. D. Thesis, Cambridge University, Engineering Department (UK)*, 1989.

[35] Ward, S. H. and Razi, H., "Effect of Thickness on the Compression Residual Strength of Notched Carbon Fiber/Epoxy Composites", *private communication.*

[36] Shu, D. and Mai, Y. W., "Buckling of Delaminated Composites Re-examined", *Composites Science and Technology, Vol. 47, pp. 35-41*, 1993.

[37] Timoshenko, S., *Strength of Materials, Part II Advanced Theory and Problems, Third Edition, D. Van Nostrand Co. Inc., Princeton, pp.161-165*, 1956.

[38] Hutchinson, J. W. and Suo, Z., "Mixed Mode Cracking in Layered Materials", *Advanced Applied Mechanics, Vol. 28, pp. 63-191*, 1991.

[39] Yin, W. L., Sallam, S. N. and Simitses, G. J., "Ultimate Axial Load Capacity of a Delaminated Beam-Plate", *AIAA Journal, Vol. 24, No. 1, pp. 123-128*, 1986.

[40] Cox, B. N., "Delamination and Buckling in 3D Composites", *Journal of Composite Materials, Vol. 28, No. 12, pp.1114-1126*, 1994.

[41] Mouritz and Cox, B. N., "Appendix – Simple, Conservative Criteria for Buckling and Delamination Propagation in the Presence of Stitching", *document in preparation.*

[42] Shu, D. and Mai, Y. W., "Effect of Stitching on Interlaminar Delamination Extension in Composite Laminates", *Composites Science and Technology, Vol. 49, No. 2, pp. 165-171*, 1993.

[43] Mikulas, M. M., "Failure Prediction Techniques for Compression Loaded Composite Laminates with Holes", *NASA CP 2142*, 1980.

[44] Vogler, T., "Compressive Behavior and Failure of Composite Sandwich Panels", *S. M. Thesis, Department of Aeronautics and Astronautics, Massachusetts Institute of Technology*, 1994.

[45] Mar, J. W. and Lin, K. Y., "Fracture of Boron/Aluminum Composites with Discontinuities", *Journal of Composite Materials, Vol. 11, pp. 405-421*, 1977.

[46] Iki, K. N., "Notch Sensitivity of Graphite/Epoxy Under Compression", TELAC Report 87-13, Massachusetts Institute of Technology, 1987.

[47] Lagace, P. A., "Notch Sensitivity and Stacking Sequence of Laminated Composites", *Composite Materials: Testing and Design (Seventh Conference), ASTM STP 893, ASTM, pp. 161-176*, 1986.

[48] Fenner, D. N., "Stress Singularities in Composite Materials with an Arbitrarily Oriented Crack Meeting an Interface', *International Journal of Fracture, Vol. 12, No. 5, pp. 705-721*, 1976.

[49] Guynn, E. G. and Bradley, W. L., "Measurements of the Stress Supported by the Crush Zone in Open Hole Composite Laminates Loaded in Compression", *Journal of Reinforced Plastics and Composites, 8, pp.133-149*, 1989.

[50] Newman, J. C., "A Nonlinear Fracture Mechanics Approach to the Growth of Small Cracks", *Behavior of Short cracks on Airframe Components, AGARD Conf. Proc., France*, 1982.

[51] Tada, H., Paris, P. C. and Irwin, G. R., *The Stress Analysis of cracks Handbook, Del Research Corporation, St. Louis, MO 63105*, 1973.

Appendix 1 – CLPT Stiffness Code

```
clear all;

% Define the Ply Properties:
k1=6894.75729317;    %conversion factor from psi to Pa
k2=0.0254;           %conversion factor from in to m
EL=k1*8.3E6;
ET=k1*8.3E6;
nuLT=0.06;
nuTL=(ET/EL)*nuLT;
GLT=k1*0.7E6;
t=k2*0.0083;

% Define the Ply Stiffness Matrix:
Q11=EL/(1-nuLT*nuTL);
Q12=nuLT*ET/(1-nuLT*nuTL);
Q22=ET/(1-nuLT*nuTL);
Q66=GLT;

Q=[];
Q(1,1)=Q11;
Q(1,2)=Q12;
Q(1,3)=0;
Q(2,1)=Q12;
Q(2,2)=Q22;
Q(2,3)=0;
Q(3,1)=0;
Q(3,2)=0;
Q(3,3)=Q66;

% Define ply angles for T45 Series:
deg=[45 0 0];
rad=deg*pi/180;

% Define ply angles for T0 Series:
%deg=[0 0 0];
%rad=deg*pi/180;

for i=1:3

theta=rad(i);

% Define the Transformation Matrices:

% Stress Transformation Matrix:
Tsigma=[];
Tsigma(1,1)=(cos(theta))^2;
Tsigma(1,2)=(sin(theta))^2;
Tsigma(1,3)=2*cos(theta)*sin(theta);
Tsigma(2,1)=(sin(theta))^2;
```

```
Tsigma(2,2)=(cos(theta))^2;
Tsigma(2,3)=-2*cos(theta)*sin(theta);
Tsigma(3,1)=-cos(theta)*sin(theta);
Tsigma(3,2)=cos(theta)*sin(theta);
Tsigma(3,3)=(cos(theta))^2-(sin(theta))^2;


% Strain Transformation Matrix:
Tepsilon=[];
Tepsilon(1,1)=(cos(theta))^2;
Tepsilon(1,2)=(sin(theta))^2;
Tepsilon(1,3)=cos(theta)*sin(theta);
Tepsilon(2,1)=(sin(theta))^2;
Tepsilon(2,2)=(cos(theta))^2;
Tepsilon(2,3)=-cos(theta)*sin(theta);
Tepsilon(3,1)=-2*cos(theta)*sin(theta);
Tepsilon(3,2)=2*cos(theta)*sin(theta);
Tepsilon(3,3)=(cos(theta))^2-(sin(theta))^2;


% Define the Laminate Stiffness Matrix:
Qbar=inv(Tsigma)*Q*Tepsilon;

if i==1
   Qbar1=Qbar;
else if i==2
      Qbar2=Qbar;
   else if i==3
         Qbar3=Qbar;
      end
   end
end

end

% Define the Extensional Stiffness Matrix:
A=t*(Qbar1+Qbar2+Qbar3);
a=inv(A);

% Calculate the Laminate Stiffness in the Load Direction:
Ex45=inv(a(1,1)*t*3)/10^9;
%Ex0=inv(a(1,1)*t*3)/10^9;
Ex45
%Ex0
```

Appendix 2 – DZM Analysis

The following pages describe the analysis performed by Newman [50] in which equations for SIF and COD for cracks emanating from a circular hole in a finite plate are obtained by modifying solutions provided by Tada [51] for cracks in an infinite plate. The geometry of the problem is depicted in Figure A2.1, and equations A2.1 through A2.3 define the segmentation of the cohesive zone.

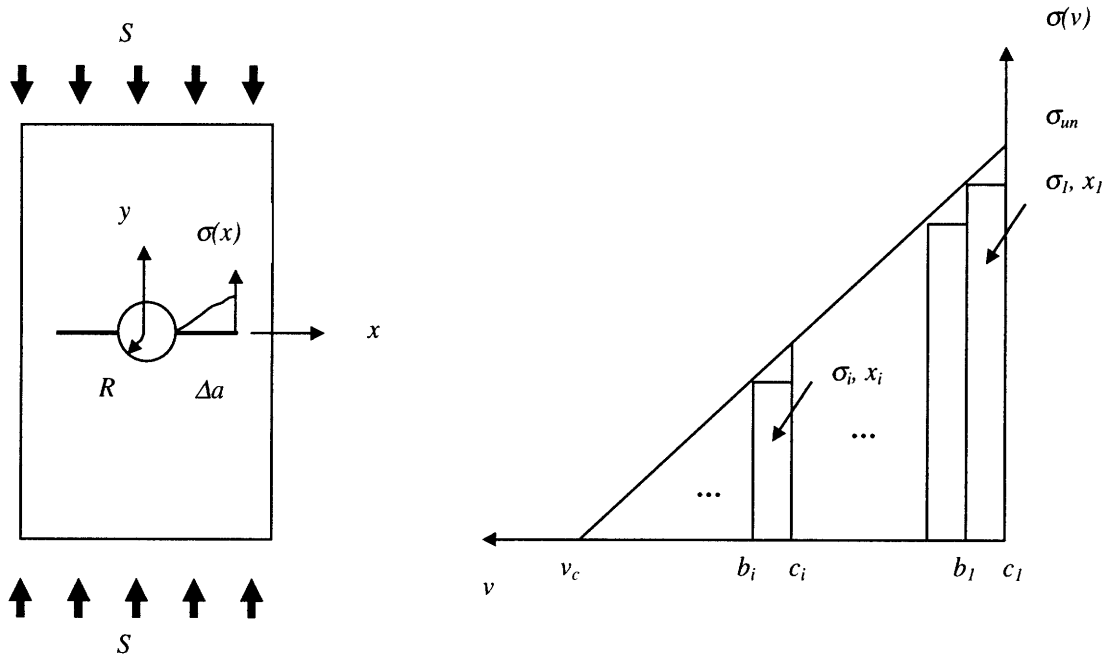

Figure A2.1: Strain softening traction law geometry.

$$x_i = (R+\Delta a) - \left(\frac{i-1/2}{n}\right)\Delta a \tag{A2.1}$$

$$c_i = (R+\Delta a) - \left(\frac{i-1}{n}\right)\Delta a \tag{A2.2}$$

$$b_i = (R+\Delta a) - \left(\frac{i}{n}\right)\Delta a \tag{A2.3}$$

(i) Stress Intensity Factors

Crack propagation is dictated by equation 5.7 which is reproduced below:

$$K_h^S + K_h^\sigma \geq K_{Ic} \tag{A2.4}$$

where K_h^S and K_h^σ are the stress intensity factors for a cracked-hole specimen due to the remote stress S and to the local stress σ, respectively, and $K_{Ic} = \sqrt{G_c E}$ is the intrinsic material fracture toughness.

(a) Remote uniform stress

The stress intensity factor due to the applied remote stress S is given by:

$$K_h^S = K_\infty^S F_h^S F_w^S \tag{A2.5}$$

where K_∞^S is the SIF for a crack in an infinite plate without a hole, F_h^S is the circular hole correction factor and F_w^S is the finite width correction factor. These are determined by:

$$K_\infty^S = S\sqrt{\pi d} \tag{A2.6}$$

$$F_h^S = f_n\sqrt{1-\frac{R}{d}} \tag{A2.7}$$

$$F_w^S = \sqrt{\sec\left(\frac{\pi R}{2W}\right)\sec\left(\frac{\pi d}{2W}\right)} \tag{A2.8}$$

where $d = R + \Delta a$ in which R is the hole radius and Δa is the crack length. Note that equation A2.4 accounts for the influence of width on stress concentration at the edge of the hole and the influence of width on stress intensity factors.

The function f_n for two symmetric cracks is given by:

$$f_n = 1 + 0.35\lambda + 1.425\lambda^2 - 1.578\lambda^3 + 2.156\lambda^4 \tag{A2.9}$$

where $\lambda = \frac{R}{d}$.

(b) Partially loaded crack

The stress intensity factor due to the local stresses σ_i is given by:

$$K_h^{\sigma} = \frac{2}{\pi}\sqrt{\pi d}\sum_{i=1}^{n}\sigma_i\left[\sin^{-1}\left(\frac{c_i}{d}\right) - \sin^{-1}\left(\frac{b_i}{d}\right)\right]F_{h\,i}^{\sigma}F_{w\,i}^{\sigma} \tag{A2.10}$$

where n is the number of elements in the cohesive zone under load $\sigma = \sigma(v)$, and $F_h{}^{\sigma}{}_i$ and $F_w{}^{\sigma}{}_i$ are the circular hole correction factor and the finite width correction factor, respectively, for the ith element. These are determined by:

$$F_{h\,i}^{\sigma} = \frac{G(\gamma,\lambda)_i}{\left[\sin^{-1}\left(\frac{c_i}{d}\right) - \sin^{-1}\left(\frac{b_i}{d}\right)\right]} \tag{A2.11}$$

$$F_{w\,i}^{\sigma} = \left[\frac{\sin^{-1}(C_i) - \sin^{-1}(B_i)}{\sin^{-1}\left(\frac{c_i}{d}\right) - \sin^{-1}\left(\frac{b_i}{d}\right)}\right]\sqrt{\sec\left(\frac{\pi d}{2W}\right)} \tag{A2.12}$$

where

$$G(\gamma,\lambda)_i = \left\{\left[1 + \frac{A_1}{(1-\lambda)} + \frac{3A_2}{2(1-\lambda)^2}\right]\sin^{-1}(\gamma) + \left[\frac{A_1}{(1-\lambda)} + \frac{(4-\gamma)A_2}{2(1-\lambda)^2}\right]\sqrt{1-\gamma^2}\right\}\Bigg|_{\gamma=\frac{b_i}{d}}^{\gamma=\frac{c_i}{d}} \tag{A2.13}$$

$$\begin{aligned} A_1 &= -0.02\lambda^2 + 0.558\lambda^4 \\ A_2 &= 0.221\lambda^2 + 0.046\lambda^4 \end{aligned} \tag{A2.14}$$

$$C_i = \frac{\sin\left(\frac{\pi c_i}{2W}\right)}{\sin\left(\frac{\pi d}{2W}\right)}$$
$$B_i = \frac{\sin\left(\frac{\pi b_i}{2W}\right)}{\sin\left(\frac{\pi d}{2W}\right)} \qquad \text{(A2.15)}$$

(ii) Crack Surface Displacements

The displacement at point *i* along the crack surface is calculated by adding the displacement v_i^S due to the remote stress *S* and v_i^σ due to the local stress σ_i:

$$v_i = v_i^S + v_i^\sigma \qquad \text{(A2.16)}$$

(a) Remote uniform stress

The crack surface displacement at point *i* due to the remote stress *S* in a finite plate is given by:

$$v_i^S = Sf(x_i) \qquad \text{(A2.17)}$$

where

$$f(x_i) = \frac{2}{E}\sqrt{d^2 - x_i^2}\,F_h^S F_w^S \qquad \text{(A2.18)}$$

(b) Partially loaded crack

The crack surface displacement at point *i* due to the local stress σ_i in a finite plate is given by:

$$v_i^\sigma = \sum_{j=1}^{n} \sigma_j \alpha(x_i, x_j) \qquad \text{(A2.19)}$$

where

$$\alpha(x_i, x_j) = A(x_i, x_j) + A(-x_i, x_j) \tag{A2.20}$$

The function $A(x_i,x_j)$ is given by:

$$A(x_i, x_j) = \frac{2}{\pi E}\left\{(c_j - x_i)\cosh^{-1}\left(\frac{d^2 - c_j x_i}{d|x_i - c_j|}\right) - (b_j - x_i)\cosh^{-1}\left(\frac{d^2 - b_j x_i}{d|x_i - b_j|}\right) + \sqrt{d^2 - x_i^2}\left[\sin^{-1}\left(\frac{c_j}{d}\right) - \sin^{-1}\left(\frac{b_j}{d}\right)\right]\right\} F_h^{\sigma} F_w^{\sigma} \tag{A2.21}$$

Appendix 3 – DZM Code

```
clear all;

%%%%%%%%%%%%%%%%%%%%%%%%%%%%%%%%%%%%%%%%%%%%%%%%%%%%%%%%%%%%%%%%%%%%%%%%%%%%
%%%%% Actual geometry, material and test data from coupon BM5 is  %%%%%
%%%%% included in this code, but it can be inter-changed with any %%%%%
%%%%% other coupon that exhibited controlled sub-critical damage  %%%%%
%%%%%%%%%%%%%%%%%%%%%%%%%%%%%%%%%%%%%%%%%%%%%%%%%%%%%%%%%%%%%%%%%%%%%%%%%%%%

% Define problem geometry and material properties:
% (assume circular hole instead of slit)
E=57.2E9;
tply=0.0083*0.0254;
W=2*0.0254;
R=0.5*0.0254;

% Input experimental data points:
daexpmm=[7 11 14.5 17 20];              % measured crack lengths
daexp=daexpmm*1E-3;
Pexp=[1628 1794.5 1770 1762.5 1782];    % measured applied loads
Sexp=Pexp*4.44822161526/(3*tply*2*W);

for l=1:length(daexp)
   ratioexp(l)=daexp(l)/R;
   dexp(l)=R+daexp(l);
   lambdaexp(l)=R/dexp(l);
   fnexp(l)=1+0.35*lambdaexp(l)+1.425*lambdaexp(l)^2-...
      1.578*lambdaexp(l)^3+2.156*lambdaexp(l)^4;
   Fhsexp(l)=fnexp(l)*sqrt(1-lambdaexp(l));
   Fwsexp(l)=sqrt(sec(pi*R/2/W)*sec(pi*dexp(l)/2/W));
   Khsexp(l)=Sexp(l)*sqrt(pi*dexp(l))*Fhsexp(l)*Fwsexp(l);
   GAexp(l)=(Khsexp(l))^2/E;
end

% Calibrate Model: input critical crack opening displacement (vc) and
% material intrinsic fracture energy (Gc):
ac=1.5E-6;        %assumed crack length when damage initiates
Sc=Sexp(1);       %applied stress when damage initiates
dc=R+ac;
lambdac=R/dc;
fnc=1+0.35*lambdac+1.425*lambdac^2-1.578*lambdac^3+2.156*lambdac^4;
Fhsc=fnc*sqrt(1-lambdac);
Fwsc=sqrt(sec(pi*R/2/W)*sec(pi*dc/2/W));
Kc=Sc*sqrt(pi*dc)*Fhsc*Fwsc;
Gc=Kc^2/E;
vc=275E-6;
Sun=Gc/vc;     % Eq. 5.2
```

```
% Assign initial crack length and increments of crack length and
% applied stress for the iterative loops:
a0=1E-4;
da=[a0:0.5E-3:3E-2];
dS=7E7;
n=10;

% R-curve starting point:
ratio(1)=a0/R;
GA(1)=Gc;

% Start loop that will increase the crack length:
for m=2:length(da)
   ratio(m)=da(m)/R;
   dK(m)=0;

   % Zero initial crack opening displacement:
   for i=1:n
      vs(i)=0;
      vsigma(i)=0;
      vtot(i)=0;
   end

   % Calculate applied stress for initial crack and no bridging:
   d(m)=R+da(m);
   lambda(m)=R/d(m);
   fn(m)=1+0.35*lambda(m)+1.425*lambda(m)^2-...
      1.578*lambda(m)^3+2.156*lambda(m)^4;          % Eq. A2.9
   Fhs(m)=fn(m)*sqrt(1-lambda(m));                  % Eq. A2.7
   Fws(m)=sqrt(sec(pi*R/2/W)*sec(pi*d(m)/2/W));     % Eq. A2.8
   S(m)=Kc/(sqrt(pi*d(m))*Fhs(m)*Fws(m));           % Eqs. A2.5 & A2.6

   % Start loop that will iterate until the applied strain energy
   % release rate minus the bridging strain energy release rate is
   % greater than the material intrinsic fracture energy:
   while (dK(m)<Kc)

      dazone=da(m);
      dzone=d(m);
      lambdazone=lambda(m);
      fnzone=fn(m);
      Fhszone=Fhs(m);
      Fwszone=Fws(m);
      Szone=S(m);

      % Split crack length into n segments and calculate the crack
      % opening displacement (COD) due to the remote stress, and the
      % corresponding tractions due to this COD:
      for i=1:n
         x(i)=(R+dazone)-((i-0.5)/n)*dazone;                % Eq. A2.1
         c(i)=(R+dazone)-((i-1)/n)*dazone;                  % Eq. A2.2
         b(i)=(R+dazone)-(i/n)*dazone;                      % Eq. A2.3
         f(i)=(2/E)*sqrt(dzone^2-x(i)^2)*Fhszone*Fwszone;   % Eq. A2.18
         vs(i)=Szone*f(i);                                  % Eq. A2.17
         vtot(i)=vs(i)+vsigma(i);                           % Eq. A2.16
         sigma(i)=Sun*(1-vtot(i)/vc);                       % Eq. 5.3
         A1=-0.02*lambdazone^2+0.558*lambdazone^4;          % Eq. A2.14
```

```
   A2=0.221*lambdazone^2+0.046*lambdazone^4;          % Eq. A2.14
   Ga(i)=(1+A1/(1-lambdazone)+3*A2/2/(1-lambdazone)^2)*...
      asin(c(i)/dzone)+(A1/(1-lambdazone)-(4-c(i)/dzone)*...
      A2/2/(1-lambdazone)^2)*sqrt(1-(c(i)/dzone)^2);
   Gb(i)=(1+A1/(1-lambdazone)+3*A2/2/(1-lambdazone)^2)*...
      asin(b(i)/dzone)+(A1/(1-lambdazone)-(4-b(i)/dzone)*...
      A2/2/(1-lambdazone)^2)*sqrt(1-(b(i)/dzone)^2);
   G(i)=Ga(i)-Gb(i);          % Eq. A2.13
   Fhsigma(i)=G(i)/(asin(c(i)/dzone)*asin(b(i)/dzone));
         % Eq.A2.11
   Fwsigma(i)=((asin(sin(pi*c(i)/2/W)/sin(pi*dzone/2/W))-...
      asin(sin(pi*b(i)/2/W)/sin(pi*dzone/2/W)))/(asin(c(i)/...
      dzone)-asin(b(i)/dzone)))*sqrt(sec(pi*dzone/2/W));
         % Eq. A2.12
   Khsig(i)=(2/pi)*sqrt(pi*dzone)*sigma(i)*(asin(c(i)/dzone)-...
      asin(b(i)/dzone))*Fhsigma(i)*Fwsigma(i);
         % Eq. A2.10

   % Calculate the crack opening displacement due to the
   % calculated tractions (each traction affects the COD of
   % all the segments!)
   for j=1:n
      x(j)=(R+dazone)-((j-0.5)/n)*dazone;
      c(j)=(R+dazone)-((j-1)/n)*dazone;
      b(j)=(R+dazone)-(j/n)*dazone;
      f(j)=(2/E)*sqrt(dzone^2-x(j)^2)*Fhszone*Fwszone;
      vs(j)=Szone*f(j);
      sigma(j)=Sun*(1-vs(j)/vc);
      Aplus(i,j)=2/(pi*E)*((c(j)-x(i))*acosh((dzone^2-...
         c(j)*x(i))/(dzone*abs(x(i)-c(j))))-(b(j)-x(i))*...
         acosh((dzone^2-b(j)*x(i))/(dzone*abs(x(i)-b(j))))+...
         sqrt(dzone^2-x(i)^2)*(asin(c(j)/dzone)-...
         asin(b(j)/dzone)))*Fhsigma(i)*Fwsigma(i);
            % Eq. A2.21
      Aminus(i,j)=2/(pi*E)*((c(j)-(-x(i)))*acosh((dzone^2-...
         c(j)*(-x(i)))/(dzone*abs((-x(i))-c(j))))-(b(j)-...
         (-x(i)))*acosh((dzone^2-b(j)*(-x(i)))/...
         (dzone*abs((-x(i))-b(j))))+sqrt(dzone^2-...
         (-x(i))^2)*(asin(c(j)/dzone)-...
         asin(b(j)/dzone)))*Fhsigma(i)*Fwsigma(i);
            % Eq. A2.21
      alpha(i,j)=Aplus(i,j)+Aminus(i,j);          % Eq. A2.20
      vsigma(i)=vsigma(i)+sigma(j).'*alpha(i,j);  % Eq. A2.19
   end

end

% Calculate stress concentration factor due to remote stress:
Khs(m)=S(m)*sqrt(pi*d(m))*Fhs(m)*Fws(m);          % Eq. A2.5

% Calculate stress concentration factor due to local tractions:
Khsigma(m)=sum(Khsig);                            % Eq. A2.10

% Compare the K's from remote stress and local tractions to
% determine if the crack will propagate:
dK(m)=Khs(m)-Khsigma(m);                          % Eq. 5.4
```

```
      % Increase applied stress if crack does not propagate:
      S(m)=S(m)+dS;

   end

   % Determine whether COD at root is larger than critical COD, at
   % which point steady-state crack growth will be reached:
   for i=1:n
      vtot(i)=vs(i)+vsigma(i);
   end

   vmax(m)=max(vtot);
   KA(m)=Khs(m);
   GA(m)=(Khs(m))^2/E;

   if (vmax(m)<=vc & vmax(m)>0)
      % critical COD not reached yet, ∴ toughening continues
      KA(m)=KA(m);
      GA(m)=(KA(m))^2/E;
   else
      % critical COD reached, ∴ steady-state crack growth follows
      KA(m)=KA(m-1);
      GA(m)=(KA(m-1))^2/E;
   end

if (GA(m)>GA(m-1))
   Lss(m)=da(m);
end

end

% Obtain outputs:
% (1) Bridging Law (values of vc, Sun and Gc)
% (2) Resistance Curve (Gss and Lss)
v_c=vc; v_c
S_un=Sun; S_un
G_c=Gc; G_c
G_ss=max(GA); G_ss
L_ss=max(Lss); L_ss

xlaw=[0; vc];
ylaw=[Sun; 0];

subplot(2,1,1),
   plot(xlaw,ylaw,'-'),
   gtext('G_c'),
   xlabel('Crack Opening Displacement, v (m)'),
   ylabel('Bridging Stress, S (Pa)'),
   title('Strain Softening Bridging Law')

subplot(2,1,2),
   plot(ratio(1:end),GA(1:end),'-',ratioexp(1:end),GAexp(1:end),'*'),
   legend('Strain Softening Bridging Law','Experimental Data for BM5'),
   xlabel('buckled length / hole radius'),
   ylabel('G_a_p_p_l_i_e_d (Pa*m)'),
   title('Resistance Curves for Partially-Bridged Crack')
```

Appendix 4 – DBM Code

```
clear all;

% Bulge width (l) parametric study sample code
% Top-middle delamination

% Define problem parameters:
Gc=300;
E1=16.663E9;
t1=0.0083*0.0254;
E2=57.226;
t2=2*t1;

% Define applied displacement vector:
u=[0:1E-6:5E-4];

%Define initial bulge width:
l=0.025*0.0254;

% Start loop that will increment bulge width for parametric study:
for m=1:1:80
   % Find critical displacements for sub-laminates to buckle:
   ecr1=pi^2/3*(t1/l)^2;      % Eq. 5.14
   ucr1=ecr1*l;
   ecr2=pi^2/3*(t2/l)^2;      % Eq. 5.14
   ucr2=ecr2*l;
   % Start loop that increments applied displacement:
   for n=1:length(u)
      % STRIP A
      % Impose conditional statements for energy and work terms:
      % Sub-laminate with thickness t1:
      if (u(n)<ucr1)          % Eqs. 5.15 and 5.16
         UA_1(n)=E1*t1/2/l*(u(n))^2;
         WA_1(n)=E1*t1/l*(u(n))^2;
      else if (u(n)==ucr1)    % Eqs. 5.17 and 5.18
            UA_1(n)=pi^4*E1*t1^5/18/l^3;
            WA_1(n)=pi^4*E1*t1^5/9/l^3;
         else if (u(n)>ucr1)  % Eqs. 5.19 and 5.20
               UA_1(n)=(pi^2*E1*t1^3/3/l^2)*u(n)-(pi^4*E1*t1^5/18/l^3);
               WA_1(n)=(4*pi^2*E1*t1^3/12/l^2)*u(n);
            end
         end
      end
      % Sub-laminate with thickness t2:
      if (u(n)<ucr2)          % Eqs. 5.15 and 5.16
         UA_2(n)=E2*t2/2/l*(u(n))^2;
         WA_2(n)=E2*t2/l*(u(n))^2;
      else if (u(n)==ucr2)    % Eqs. 5.17 and 5.18
            UA_2(n)=pi^4*E2*t2^5/18/l^3;
            WA_2(n)=pi^4*E2*t2^5/9/l^3;
```

```
         else if (u(n)>ucr2)  % Eqs. 5.19 and 5.20
               UA_2(n)=(pi^2*E2*t2^3/3/l^2)*u(n)-(pi^4*E2*t2^5/18/l^3);
               WA_2(n)=(4*pi^2*E2*t2^3/12/l^2)*u(n);
            end
         end
      end

      % Get total energy and work terms for Strip A:
      UA(n)=UA_1(n)+UA_2(n);  % Eq. 5.21
      WA(n)=WA_1(n)+WA_2(n);  % Eq. 5.22

      % STRIP B
      UB(n)=((E1*t1+E2*t2)/2/l)*(u(n))^2;     % Eq. 5.23
      WB(n)=((E1*t1+E2*t2)/l)*(u(n))^2;       % Eq. 5.24

      % Obtain differences and applied strain energy release rate:
      deltaU(n)=UA(n)-UB(n);
      deltaW(n)=WA(n)-WB(n);
      Gapp(n)=(deltaU(n)-deltaW(n))/l;        % Eq. 5.25
      Gcrit(n)=Gc;

      % Compare to material intrinsic fracture energy:
      if (Gapp(n)<Gc)       % Eq. 5.27
         uprop=u(n);
      end
   end

   lnotch(m)=l*100;
   upropa(m)=uprop/1E-6;

   % Increase bulge width for next iteration:
   l=l+0.0125*0.0254;
end

% Plot values of applied displacement for propagation for different
% bulge width values:
plot(lnotch(1:end),upropa(1:end),'-');
axis([0 max(lnotch) 0 max(upropa)]);
title('Applied Displacement for Bulge Propagation vs. Buckle Width');
xlabel('Buckle Width (cm)');
ylabel('Applied Displacement for Bulge Propagation (microns)');
```